ABSTRACT

Title of Document: REGULATION OF SHAPE DYNAMICS AND ACTIN POLYMERIZATION DURING COLLECTIVE CELL MIGRATION

Chenlu Wang, Doctor of Philosophy, 2016

Directed By: Professor Wolfgang Losert
Department of Physics

This thesis aims to understand how cells coordinate their motion during collective migration. As previously shown, the motion of individually migrating cells is governed by wave-like cell shape dynamics. The mechanisms that regulate these dynamic behaviors in response to extracellular environment remain largely unclear. I applied shape dynamics analysis to *Dictyostelium* cells migrating in pairs and in multicellular streams and found that wave-like membrane protrusions are highly coupled between touching cells. I further characterized cell motion by using principle component analysis (PCA) to decompose complex cell shape changes into a serial shape change modes, from which I found that streaming cells exhibit localized anterior protrusion, termed front narrowing, to facilitate cell-cell coupling.

I next explored cytoskeleton-based mechanisms of cell-cell coupling by measuring the dynamics of actin polymerization. Actin polymerization waves observed in individual cells were significantly suppressed in multicellular streams. Streaming cells exclusively produced F-actin at cell-cell contact regions, especially at cell fronts. I demonstrated that such restricted actin polymerization is associated with

cell-cell coupling, as reducing actin polymerization with Latrunculin A leads to the assembly of F-actin at the side of streams, the decrease of front narrowing, and the decoupling of protrusion waves.

My studies also suggest that collective migration is guided by cell-surface interactions. I examined the aggregation of *Dictyostelim* cells under distinct conditions and found that both chemical compositions of surfaces and surface-adhesion defects in cells result in altered collective migration patterns. I also investigated the shape dynamics of cells suspended on PEG-coated surfaces, which showed that coupling of protrusion waves disappears on touching suspended cells.

These observations indicate that collective migration requires a balance between cell-cell and cell-surface adhesions. I hypothesized such a balance is reached via the regulation of cytoskeleton. Indeed, I found cells actively regulate cytoskeleton to retain optimal cell-surface adhesions on varying surfaces, and cells lacking the link between actin and surfaces (*talin A*) could not retain the optimal adhesions. On the other hand, suspended cells exhibited enhanced actin filament assembly on the periphery of cell groups instead of in cell-cell contact regions, which facilitates their aggregation in a clumping fashion.

REGULATION OF SHAPE DYNAMICS AND ACTIN POLYMERIZATION DURING COLLECTIVE CELL MIGRATION

By

Chenlu Wang

Thesis submitted to the Faculty of the Graduate School of the
University of Maryland, College Park, in partial fulfillment
of the requirements for the degree of
Doctor of Philosophy
2016

Advisory Committee:
Professor Wolfgang Losert, Chair
Adjunct Professor Carole Parent, Co-advisor

Professor Jose Helim Aranda-Espinoza, Dean's Representative
Professor Dorothy Beckett
Professor Arpita Upadhyaya

Acknowledgements

Most of all, I would like to express my deepest gratitude to my advisor, Dr. Wolfgang Losert, for his genuine kindness and consistent support throughout the research. He always inspires me with brilliant scientific ideas and guides me through difficulties with his optimism and encouragement. Thousands of thanks to my co-advisor, Dr. Carole Parent, who is always curious about new research fields and enthusiastic about both science and life, setting an example of excellence as a researcher, mentor, and leader. Dr. S.K. Gupta introduced a new world of robotic engineering to me, and he was tremendously supportive and patient throughout our collaboration.

I would like to thank my fellows in Losert and Parent labs: Meghan Driscoll, for her brilliant scientific suggestions, unconditional help on programming, and her wonderful shape analysis code, without which I would spend another seven years on developing analytical tools; the Dicty crowd at NIH, Paul Kriebel and Weiye Wang, for their great suggestions and their help on cell culture, experiments, and everything else; Colin McCann, for his one-on-one teaching of experimental skills during those weekends; Satarupa Das, for her guidance on cell biology experiments, knowledge on *Dictyostelium*, and her insider tips giving as a seasoned mom; Xiaoyu Sun, for her insightful discussion on projects, career, and life, and for being a best friend; Can Guven, for all the discussions on modeling and his experiences as a new parent; Yang Shen, for her advice on statistical analysis; Rachel Lee, for being an incredible lab/office mate and a UMD-NIH buddy that I could not ask for anyone better. Also, thanks to Philippe Afonso, Samira Aghayee, Leonard Campanello, Julian Candia,

Desu Chen, Song Chen, Sagar Chowdhury, Matt Harrington, Deborah Hemingway, Mark Herrera, Matt Hourwitz, Lunhua Liu, Ritankar Majumdar, Kostas Moissoglu, Kerstin Nordstrom, EChO, Ava Omidvar, Joshua Parker, Erin Rericha, Sebastian Schmidt, Christina Stuelten, Aidin Tavakoli, and Michael Weiger, for all their kindness and support.

I have received tremendous help from people outside of my two research labs: Dr. Dorothy Beckett, in whose lab I started bio-bench work and decided to be an experimentalist; Dr. Arpita Upadhyaya, in whose lab I started the practice of cell culture and microscopic imaging that turned to be essential tools of my research; Dr. Valarie Barr, Dr. Itoro Akpan, and Dr. Amy Beaven, who trained and assisted me on microscopes; Star Jackson, Caricia Fisher, Stephanie Noel, and Nancy Cruz, who made my life much easier.

My family and friends have provided the strongest support for me to pursue a better self. My loving husband, Zhijian Zhang, thank you for walking with me through this journey and growing up with me together; a special credit to you for taking the little one out for a walk so that I can finish this page. My sweetest daughter, Ruochen, I have learned so much from you, and I'm so proud of you. Thanks to my parents and parents-in-law for the most reliable baby care and numberless other supports. Thanks to my grandparents for years of love and inspiration. My great friends, Xue Fei and Lance, Yuanting, Lin Zhu, Ying Chen and Donglei, Rian and Jinglei, Christy and Vali, Qi Xia and Kelvin, thank you all!

Finally, I would like to thank the members of my committee: Professor Wolfgang Losert, Professor Jose Helim Aranda-Espinoza, Professor Dorothy Beckett, Adjunct Professor Carole Parent, and Professor Arpita Upadhyaya.

Table of Contents

List of Figures

Chapter 1: Introduction

In this thesis, I study the motility and migration of the eukaryote *Dictyostelium discoideum* from a biophysical perspective. Cell migration is a ubiquitous phenomenon. Many types of cell migration, such as wound healing, tissue formation, and development of organisms, involve the collective migration of attached groups of cells. Collectively migrating cells require the ability to sense multiple external signals, either from extracellular substrates or from neighboring cells. Cells respond to these signals by actively regulating their cytoskeletons and subsequent motions, both of which have been shown to exhibit wave-like dynamics. The scope of this thesis is to understand how these wave-like behaviors are regulated by various guidance cues from external substrates and neighboring cells during collective cell migration.

1.1 Overview of Cell Migration

Cell migration has been observed from the early days of microscopy development in the 17th century, and it is found to be a ubiquitous phenomenon that occurs in all eukaryotic organisms for at least a small time window during their life spans. Some cells, such as leukocytes, maintain the ability to migrate throughout their

life (Figure 1.1A). On the other hand, other cells are motile during only part of their life spans. For example, primordial cells migrate to form the nervous system during embryo development and lose their motility afterward (Figure 1.1B) (Matsuda & Chitnis 2010). Some cells, as described in many cancer metastasis cases, are initially immotile and then gain the ability to migrate following certain events (Figure 1.1D) (Hanahan & Weinberg 2011). Examples of cell migration are shown in Figure 1.1, including neutrophils, primordial cells, endothelial cells and cancer cells (Vitorino et al. 2011; Alexander et al. 2008).

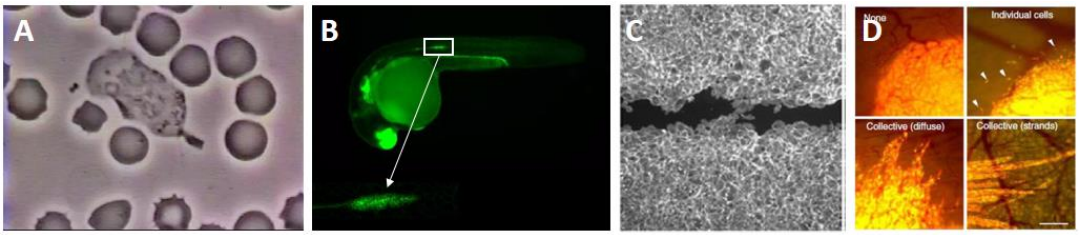

Figure 1.1 - Examples of Cell Migration. (A) A neutrophil migrates through a field of red blood cells, chasing after a bacterium (Staphylococcus aureus). (A snapshot from a youtube movie that was originally taken by David Rogers, Vanderbilt University in the 1950s.) The image is reproduced under the CC BY License. (B) Posterior lateral line primordial cells migrate in cohesive clumps during the development of the mechanosensory lateral line organ in a Zebrafish. (Courtesy of Deborah Hemingway, Biophysics Program at Univeristy of Maryland.) (C) A sheet of endothelial cells (gray) collectively migrates to close a gap (black) during wound healing. The image is reproduced from (Vitorino et al. 2011) with permission. (D) Tumor cells migrate out of a primary tumor either individually or collectively to invade neighboring tissue. The image is reproduced from (Alexander et al. 2008) with permission.

Cells migrate to carry out key biological functions from tissue formation and

organ development to the immune responses, wound healing, and cancer metastasis (Lauffenburger & Horwitz 1996; Matsuda & Chitnis 2010; Hanahan & Weinberg 2011). Different types of cells migrate within distinct contexts to fulfill their functions. Leukocytes can migrate within blood vessels as well as tissues to reach infection sites. Epithelial cells, however, can only migrate on the surfaces of tissues and organs.

Overall, cell migration occurs in vivo in 3D tissue environments or within the circulatory system, where cells are exposed to complex surrounding environments composed of the extracellular matrix and various types of cells. Depending on cell types and cues from the micro-environment, migrating cells exhibit distinct migratory phenotypes. Cell migration can be classified into individual and collective migration. As shown in Figure 1.2 (top half), individually migrating cells adopt different migration modes, which are reflected in distinct cell morphologies, including amoeboid mode, mesenchymal mode, and blebbing mode (Lauffenburger & Horwitz 1996; Friedl & Wolf 2010; Yoshida & Soldati 2006). Collectively migrating cells form direct cell-cell contacts and form multicellular groups that sometimes migrate with stream-like or strand-like patterns as illustrated in Figure 1.2 (bottom half) (Friedl & Wolf 2010). The migratory manners that cells adopt within different types of collective migration patterns have yet to be fully understood.

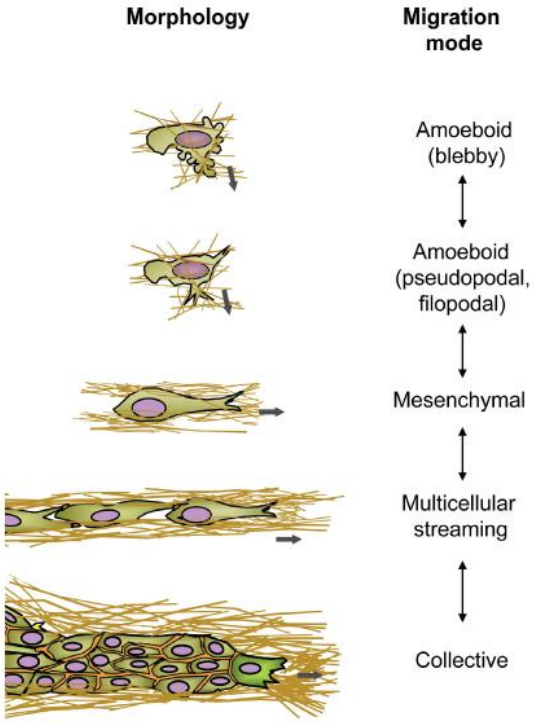

Figure 1.2 Cells Exhibit Distinct Morphologies and Migratory Phenotypes. Cells migrate through crowded environment contacting with extracellular matrix and other cells during collective migration. The image is reproduced from (Friedl & Wolf 2010) with permission.

Leukocytes, dendritic cells, and *Dictyostelium* cells are typical amoeboid cells; fibroblasts and neural crest cells are typical mesenchymal cells; endothelial and epithelial cells are typical collectively migrating cells. However, after losing cell-cell adhesion, epithelial cells can individually exhibit mesenchymal migration, a process termed epithelial-mesenchymal transition (Thiery 2002). In addition, mesenchymal-like cancer cells can convert to the amoeboid type via mesenchymal-amoeboid transition (Friedl & Wolf 2003). Although migratory phenotypes are distinct in pseudopod generation, cell-substrate interaction, and migration speed, they are related

and can interconvert under certain circumstances depending on the cell states and external environmental cues. This is because they use similar cytoskeleton-based migratory machineries that can be regulated in response to external signals (Keren et al. 2008; Farooqui & Fenteany 2005; Friedl & Wolf 2003).

1.2 Cell Motion and Cytoskeletal Mechanisms

A typical migration of an individual cell is a dynamic shape change process involving the generation of protrusions at the cell front and contractions at the back and side of cells. The protrusions and contractions are actively regulated by the cytoskeleton. The cytoskeleton is a complex cytoplasmic network formed by interlinking filaments and tubules, including actin filaments, intermediate filaments, and microtubules as illustrated in Figure 1.3.

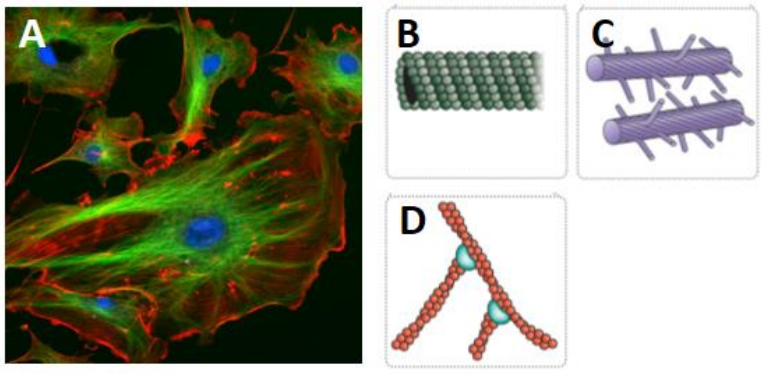

Figure 1.3 Microscopic Image and Diagrams of Cytoskeleton. (A) Cytoskeleton stained endothelial cells under the microscope. Nuclei are stained blue, microtubules are marked green, and actin filaments are labeled in red. The image is reproduced from https://en.wikipedia.org/wiki/Cytoskeleton under the CC BY License. Diagrams of a microtubule (B), intermediate filaments (C), and actin filaments (D). Images are reproduced from (Fletcher 2010) with permission.

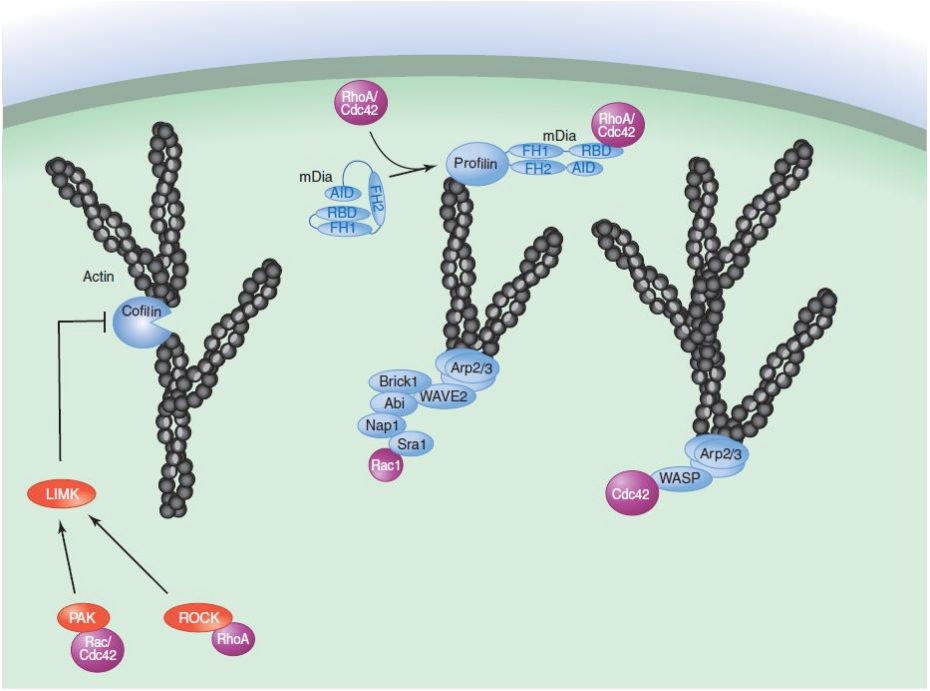

Figure 1.4 Regulation of Actin Network Dynamics in Cell Protrusions. The image is reproduced from (Devreotes & Horwitz 2015) with permission.

The cytoskeleton maintains cell integrity and enables cell migration by regulating dynamic cell shapes via actin polymerization and myosin-mediated contraction. When a cell is stimulated by external signals, the polymerization of actin monomers to filamentous actin occurs at the leading edge of the cell. The growing actin filaments at their barbed end (polymerizing end) push the cell membrane to protrude and form F-actin rich protrusions, such as pseudopods that are wide and thick, lamellipodia that are wide and flat, and spiky filopodia that are thin extensions (Yoshida & Soldati 2006; Lauffenburger & Horwitz 1996; Ridley 2011). As illustrated in Figure 1.4, the polymerization process is regulated by molecules, including formin proteins that nucleate and regulate the linear growth of actin

filaments, Arp2/3 that nucleate filament branches from existing filaments at a 70 degree angle, as well as capping proteins and cofilin, which inhibit the polymerization of filaments and sever actin filaments respectively to facilitate the recycling of actin monomers (Devreotes & Horwitz 2015). Together these molecules produce a dendritic actin network that generates and stabilizes protrusions. On the other hand, the movement of the whole cell body is also driven by the contraction of the rest of the cell body, which is mediated by the protein non-muscle Myosin II (Meili et al. 2010; Reichl et al. 2008). Microtubules are also found to be involved in the migration process (Dogterom & Surrey 2012), as they are oriented toward the site of polarity, which help to deliver materials to the leading edge of migrating cells.

During migration, the building blocks of the cytoskeleton dynamically assemble and disassemble, which leads to complex cytoskeletal behaviors as shown in some recent studies. Wave-like dynamic behaviors have been observed by Gerisch *et al.*, who found that actin polymerization initiates and propagates in a self-organized wave-like manner on the boundary of *Dictyostelium* cells recovering from actin depolymerization (Figure 1.5A) (Gerisch et al. 2004). Outward waves have been observed by Weiner *et al.* in neutrophils with fluorescently labeled Hem-1, an activator of actin nucleation (Figure 1.5B) (Weiner et al. 2007) and by Hui *et al.* on T cells membrane during cell spreading and activation (Lam Hui et al. 2012; Lam Hui et al. 2014). Bidirectional and unidirectional actin waves guided by nano-topographies have been shown in recent studies by Losert et al. (Figure 1.5C) (Driscoll et al. 2014; Sun et al. 2015). In addition, cell shape and cell motion exhibit similar wave-like dynamic behaviors as shown in multiple unicellular and

multicellular systems (Driscoll et al. 2011; Driscoll et al. 2015; Zaritsky et al. 2014). Further understanding of these dynamic behaviors provides insights into how cells adapt their migration to the complex external environment.

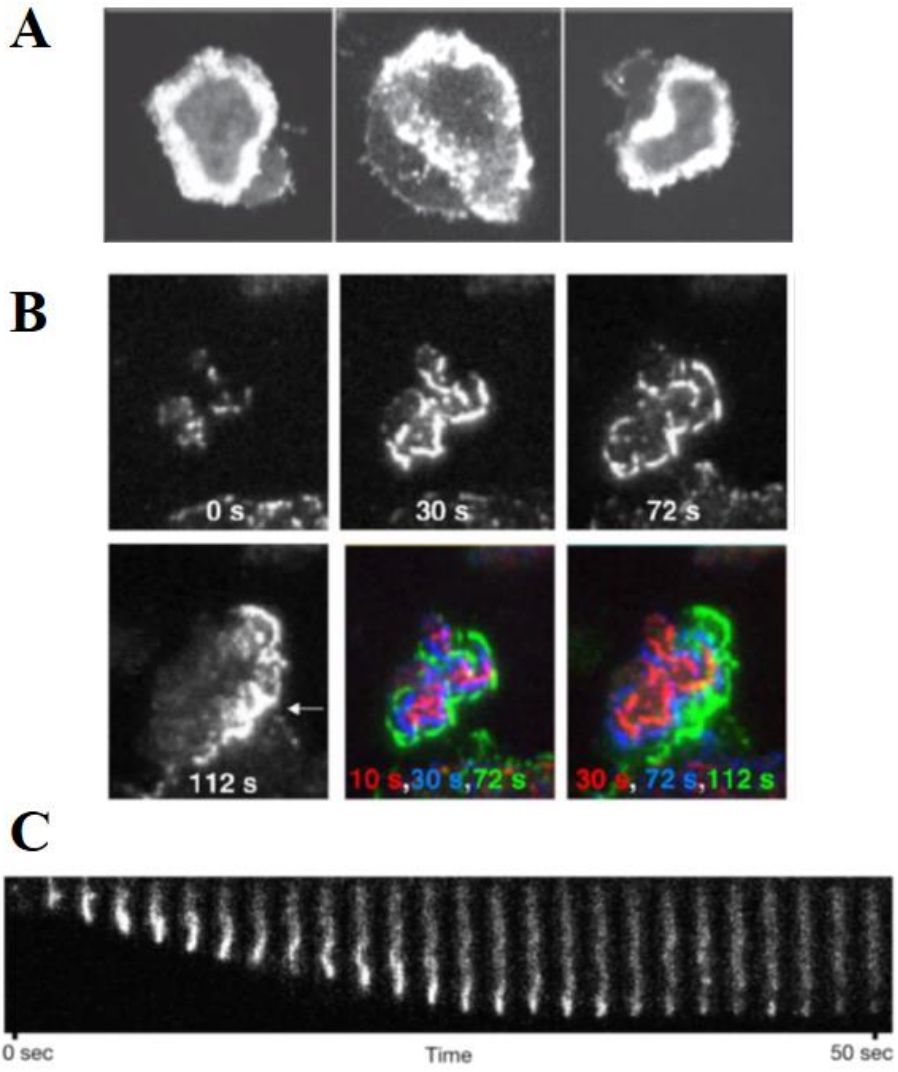

Figure 1.5 Wave-like Actin Activities are Seen in Cells: *Dictyostelium* (A, C) and neutrophil (B). Images are reproduced from (Gerisch et al. 2004; Weiner et al. 2007; Driscoll et al. 2014) with permission.

The focus of this thesis is to investigate dynamic shape deformation and

cytoskeletal activity by tuning the interactions between cells and the external environment via cell-cell and cell-substrate adhesions. During the migration of some types of cells, extended pseudopods form cell-substrate adhesions. The cell-substrate binding sites serve as anchor points for moving the whole cell body forward (Lauffenburger & Horwitz 1996). As the whole cell body moves forward, cell-substrate adhesions quickly disassemble so that the back of the cell detaches from the substrate (Parsons et al. 2010). Collectively migrating cells maintain strong and dynamic cell adhesion with neighboring cells (Collins & Nelson 2015). In mammalian cells, the adhesion at the cell-cell junction is usually cadherin-based, and cell-cell adhesion interacts with cell-substrate adhesion in a coordinated manner (Parsons et al. 2010; Burute & Thery 2012).

Overall, there is a feedback loop between the cytoskeleton and adhesions: cells sense external substrate and neighboring cells via adhesions and assemble their cytoskeleton accordingly; the cytoskeleton, in turn, actively regulates adhesions, thereby adapting cell motion to a varying external environment. The interplay between cell-cell and cell-substrate adhesions will be explained in detail in Chapter 5. How external signals guide cell migration via adhesions will be further discussed in the next section.

1.3 Sensing of Signals from the Environment

The active deformation of cell shapes and the re-organization of the cytoskeleton enable cell migration in response to external stimulus. The stimulating signals can be chemical signals from the surrounding environment, mechanical

signals from the extracellular substrate, or chemical and mechanical signals from neighboring cells. Cells transduce these external signals through receptors and other adhesions into internal signals. Complex signaling pathways have been revealed based on extensive studies on various types of cells in the context of migration and adhesion. As mentioned in section 1.1, epithelial cells, which commonly migrate collectively, can change to a mesenchymal or amoeboid mode of migration under certain circumstances. Such interconversion between migration modes suggests that similar signaling pathways are shared by a broad range of cell types. In this section, I will focus on *Dictyostelium* and guidance signals for their migration, yet these external signals are often found to be effective for higher eukaryotic cells as well.

Chemical signals from the surrounding environment:

Chemical signals usually guide cell migration through a process termed chemotaxis, where cells sense the concentration gradient of chemoattractants and migrate toward higher concentrations. Many chemotactic systems have been identified. For example, *Dictyostelium* cells are guided by the gradient of the chemoattractant cyclic adenosine monophosphate (cAMP) and migrate towards higher concentrations of cAMP (Kriebel et al. 2003). Likewise, neutrophils are able to migrate towards N-formyl-methionine-leucine-phenylalanine (fMLP) using chemotactic signaling mechanisms common with *Dictyostelium* (Anna Bagorda Carole A. Parent 2006).

Concentration gradient signals are transduced into the cell body and activate a signaling cascade network, which includes numerous components and involves crosstalk between molecules from different signaling pathways. The pathway of

phosphoinositide 3-kinase (PI3K), shown in Figure 1.6, is one of the most-studied gradient-sensing pathways, which is initiated by the binding of chemoattractants with G-protein coupled receptors (GPCRs) on the plasma membrane (Parent et al. 1998; Parent & Devreotes 1999). This binding leads to the dissociation of α and βγ subunits from the heterotrimeric G proteins, that go on to activate a wide range of parallel pathways, one of which targets Ras, which in turn actives PI3K. PI3K is recruited at the cell front where it produces phosphatidylinositol-3,4,5-triphosphate (PIP3). By recruiting PH-domain-containing proteins (Akt, PKB, etc), PIP3 can regulate GTP-binding proteins, for example, Rho-family small GTPases (Garcia & Parent 2008; Friedl & Gilmour 2009). The Rho-family GTPases, such as Rac, regulate actin polymerization by targeting cofilin, the WASP family, and in turn Arp2/3 (Ridley et al. 2003; Heasman & Ridley 2008; Ridley 2011). Meanwhile, phosphoinositide 3' phosphate phosphatase (PTEN) is recruited to the back and sides of cells, converting PIP3 into PIP2 (Iijima & Devreotes 2002).This process suppresses the activation of PH-domain binding proteins in these regions, which in turn down-regulates the activity of small GTPase proteins. Thus, the asymmetrical distribution of PI3K and PTEN leads to a polarized cytoskeleton and eventually directional migration. In addition to this PI3K-centered-pathway, there are other pathways that act in parallel, such as the pathway involving the target of rapamycin complex 2 (TORC2) (Veltman et al. 2008; King & Insall 2008; Devreotes & Horwitz 2015). With this complex signaling network, cells have the ability to transduce external shallow chemical gradients into steep internal signals, and in turn, regulate the cytoskeleton and cell motion.

The network that I introduced here is based on findings on *Dictyostelium* and neutrophils, but they have a large overlap with the pathways found in many other types of cells. For example, GPCR-mediated transduction pathways are highly conserved in eukaryotic cells (Penela et al. 2014); Rho GTPases are found to be the convergence point of many signaling pathways, which play a key role in regulating the actin cytoskeleton in all eukaryotic cells (Etienne-Manneville & Hall 2002; Devreotes & Horwitz 2015).

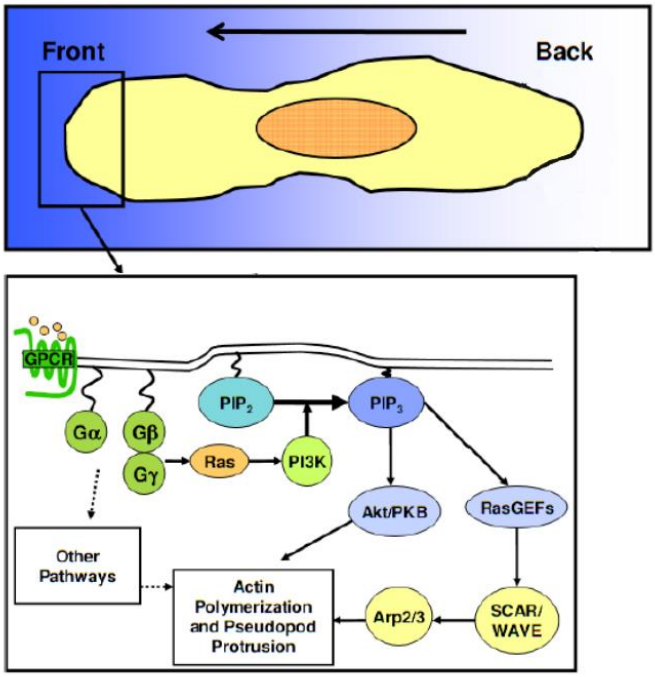

Figure 1.6 Signaling Pathways of Chemical Gradient-Sensing. The image is reproduced from (McCann 2011) with permission.

Mechanical signals from the extracellular substrate:

Mechanical properties of the extracellular substrate can guide cell migration. Multiple types of mechanical guidance cues have been reported. For example, cells

are able to follow gradients of the stiffness of the extracellular matrix (ECM), a phenomenon known as durotaxis (Roca-Cusachs et al. 2013). Cells can be guided by external physical forces exerted by other objects (Weber et al. 2012; Fujita et al. 2009). In addition, the topography of the ECM can provide the contact guidance for cell migration. It has been shown *in vivo* that fiber-like structures in the ECM can provide directional guidance for individual cells and multicellular streams (Wolf et al. 2013; Ventre et al. 2012).

Mechanical signals from extracellular substrates guide cell migration via integrin-based cell-substrate adhesion complexes, termed focal adhesions. Integrins are transmembrane proteins that bridge the cytoskeleton to extracellular substrates. They are actively regulated by actin filaments through adaptor proteins, such as talin, vinculin, and α-actinin (Case & Waterman 2011; Schwarz & Gardel 2012). On the other hand, amoeboid-like cells form non-integrin-based surface adhesions. However, my colleagues and I found that non-integrin-based cell-substrate adhesions can also be actively regulated by the cytoskeleton. Cells exhibit different collective migration patterns on surfaces with different inherent adhesivities. Details about this finding will be further discussed in Chapter 4. Moreover, the nano-topography of the extracellular surface has been found to be an efficient contact guidance cue for amoeboid cells, as cells migrate more directionally on nano-scale structures like ridges and grooves (Driscoll et al. 2014; Sun et al. 2015). All of these findings reveal that, even for cells without focal adhesions, mechanical cell-surface interactions serve as powerful guidance cues for cell migration. Therefore, the motivation of my

research in Chapter 3, 4 & 5 is to understand non-integrin-based cell-substrate interactions and their cytoskeleton-based mechanisms.

In addition to mechanical signals from extracellular substrates, physical properties of the external environment have been shown to be guidance cues for cell migration, such as electric fields and shear stress caused by fluid flow (Zhao et al. 2002; Lin et al. 2008; Hsu et al. 2005).

Chemical and mechanical signals from neighboring cells:

Collectively migrating cells can sense signals from neighboring cells and adapt their migration accordingly. Such intercellular interactions are sometimes mediated by signaling molecules, which can be lipids, phospholipids, amino acids, monoamines, proteins, glycoproteins, or other small molecules. Cells release molecules into the extracellular environment, where neighboring cells are able to perceive the molecules and respond to them. For example, *Dictyostelium* cells not only move towards cAMP but also produce and release cAMP at their rear to locally change the cAMP gradient that is sensed by neighboring cells. This signaling relay process is essential for the aggregation of *Dictyostelium* (Kriebel et al. 2003). Neutrophils, on the other hand, secrete a secondary chemoattractant, Leukotrene B_4 (LTB_4) upon stimulation with primary chemoattractants, such as fMLP. Neighboring neutrophils can sense LTB_4 and be guided (Afonso et al. 2012; Lammermann et al. 2013). As another example, human breast cancer cells have been found to form invading streams *in vivo* by using paracrine and autocrine signaling loops between tumor cells and host macrophages (Dovas et al. 2012).

Some recent studies indicate that intercellular signals can also be transmitted via direct cell-cell contact. Molecules in cell-cell adhesion, such as cadherins, often directly or indirectly connect to the intracellular cytoskeleton, and in turn, regulate cell motion. As shown in Figure 1.7, E-cadherin in cell-cell junctions connects to actin filaments through intermediate proteins such as catenins, talin, and other actin-binding proteins, which allows cells to adapt their cytoskeleton and motion in response to the signals from neighboring cells. It has been found that by exerting force at cell-cell contact boundaries a polarized *Xenopus mesendoderm* cell can induce reorganization of keratin intermediate filaments in the contacting cell, which eventually leads to protrusion generation and polarization of the contacting cell and the rest of the cell sheet (Weber et al. 2012). Recent work on epithelial cells also shows that cell-cell adhesion molecules mechanically couple with actin filaments and myosin to coordinate cell movement during wound healing (Menko et al. 2014). Such mechanical coordination of the monolayer cell sheet is found to be mediated by the propagation of waves in recent theoretical studies (Zaritsky et al. 2014).

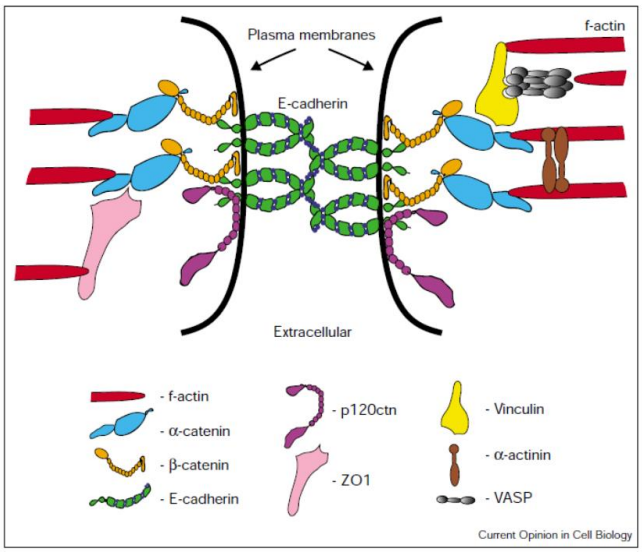

Figure 1.7 - Schematic Model of Cell-Cell Junctions on Adhered Epithelial Cells. The extracellular domain of E-cadherin interacts with intracellular F-actin via intermediate proteins on neighboring cells. The image is produced from (Vasioukhin & Fuchs 2001) with permission.

Despite the fact that signaling through cell-cell contacts is found in many biological systems, the underlying mechanisms of mechanical coupling during collective migration remain largely unknown. Therefore, the motivation of my research in ch5 & ch6 is to understand cell-cell interactions during collective cell migration and their cytoskeleton-based mechanisms.

Overall, cells are able to sense various external guidance signals as summarized in Figure 1.8. Cells then integrate these signals internally and regulate their cytoskeleton and migration accordingly.

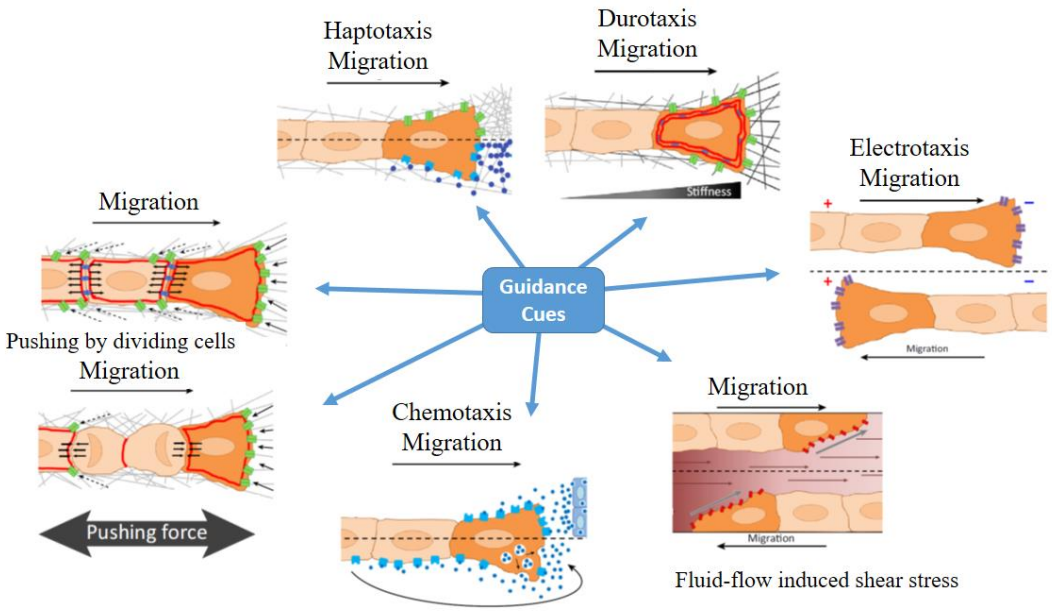

Figure 1.8 - Diversity of Guidance Cues and Signaling in Cell Migration. The image is adapted from (Haeger et al. 2015) with permission.

1.4 Thesis Outline

This thesis mainly focuses on how cell shape and cytoskeleton are regulated by cell-surface and cell-cell interactions during collective chemotactic migration. In this chapter, I introduced some general information about cell migration: the diversity of this phenomenon, the internal machinery of cell migration, and the biophysical views of cell movement. Multiple guidance cues for cell migration and cell-cell/cell-substrate interactions have been further reviewed in depth. I will provide more detailed background information directly related to my thesis research in Chapter 2, including the life cycle of *Dictyostelium* - my chosen biological model system, primary experimental techniques and analysis approaches that were applied in my research.

Chapter 3 presents my work on optical micromanipulation of active cells to probe their mechanical responses to minimal perturbations. Cells exhibit a polarized shape and cytoskeleton, which results in distinct cell-substrate and cell-cell interactions at different locations on their cell boundary. Thus, it would be ideal if the cell-cell/cell-substrate contact is created in a controllable way. To this end, I developed optical manipulation approaches, direct pushing and indirect pushing approaches, to non-invasively manipulate cells.

The indirect pushing approach significantly reduced the potential photodamage to target cells. In the viability study, most of the indirectly pushed cells were able to maintain their polarization and even dynamic shape waves after manipulation. Thus, indirect pushing can be applied to study many biological questions regarding cell motility. Indeed, the manipulation approaches I developed in this study were further applied to the study of cell-substrate interaction, which will be described in Chapter 5.

Chapter 4 discusses how *Dictyostelium* cells actively regulate cell-surface adhesion to migrate on various surfaces. Cell migration requires binding between cells and the external substrates, which should be strong and dynamic (Collins & Nelson 2015). Previous studies indicate that mammalian cells re-assemble their cytoskeleton to adapt to extracellular conditions, which is mediated by integrin-based adhesions. I was motivated to understand how cells adapt to mechanical cues via non-integrin based adhesion by plating *Dictyostelium* on surfaces with different chemical compositions.

Overall, I found that cells actively regulated their cytoskeleton and retained optimal cell-surface adhesions in response to different extracellular surfaces, suggesting that the integrin-based adhesion is not required for cells to respond to mechanical cues. Talin A is an adapter protein that connects transmembrane adhesion molecules to actin filaments. The cell-surface adhesion of cells lacking talin A was mainly affected on less adhesive surfaces, where the cell-surface adhesion is reinforced by the actin cytoskeleton. In addition, my colleague and I expanded the study from individual migration to collective migration and found that proper collective migration requires a balance between cell-cell and cell-surface adhesion. This result directly motivated my in-depth study on the interplay of cell-surface and cell-cell adhesions, which will be discussed in Chapter 5.

As mentioned above, collective cell migration involves notable cell-cell and cell-substrate adhesions. Mammalian cells form cadherin-based cell-cell adhesion and integrin-based cell-substrate adhesion. Cytoskeleton enables the formation and maintenance of both adhesions and allows the coordination between them (Parsons et al. 2010; Burute & Thery 2012). On the other hand, some fast-moving cells, such as *Dictyostelium*, form non-cadherin-based and non-integrin-based adhesions with neighboring cells and substrates. The interplay of adhesions in these cells remains largely unexplored.

Chapter 5 shows that cell shape dynamics and actin polymerization of individual cells are not surface-adhesion-dependent, as we observed that suspended cells exhibit similar shape and actin dynamics as adhered cells. However, collective migration pattern was significantly altered upon the loss of surface adhesion,

suggesting that surface-adhesion is crucial for cell-cell interactions. I further discovered that the coupling of protrusion waves on pairs of contacting adherent cells allows cells to migrate in a coordinated manner. In this context, I found that the actin cortex is coordinated by cell-cell and cell-substrate adhesions in a way that facilities collective migration. Yet, the driving force of coupled protrusion waves and the interaction of the actin cortex between neighboring cells remain unclear. Thus, I further explored these questions in chapter 6.

Given that the coordination of the cytoskeleton via cell-cell adhesions has been recognized in various types of cells (Weber et al. 2012; Menko et al. 2014; Wu et al. 2014), I proposed that the coupling of protrusion waves is mediated by the traveling actin waves. Remarkably, I found that waves of actin polymerization were significantly suppressed, and assembly of actin filaments exclusively occurred at cell-cell contacts in streams instead of propagating along the boundaries of individual cells. The suppression of actin waves enables the robustness of cell migration. The restricted actin polymerization facilitates the front narrowing behavior at cell-cell contact and enables the wave coupling between cells. This study reveals the mechanism that regulates the cell cytoskeleton and the subsequent motion in response to collective migration.

Chapter 7 presents the main conclusions of my studies and discusses potential future studies that can be pursued to further understand the mechanisms that regulate collective cell migration.

Chapter 2: Background

This chapter provides background information that is closely related to my thesis research, including an introduction of *Dictyostelium*, the model system that I mainly work with, experimental techniques that are crucial for my studies, and major analysis approaches that are applied in my research. Since the purpose of this chapter is to discuss the prerequisites of my research and prepare the readers for the following chapters, I also review previous findings, methods, and tools that motivated my studies.

2.1 Dictyostelium discoideum: a model system to study chemotaxis and collective migration

Dictyostelium cells are social amoeba that usually live in soil or leaf litter. They are eukaryotic cells and can be either unicellular or multicellular depending on the life stage they are in. Their life cycle is relatively short (24 hours) and consists of four stages: vegetative, aggregation, migration, and culmination (Figure 2.1A) (Dormann & Weijer 2006). Vegetative *Dictyostelium* live as unicellular cells when there is sufficient nutrition in the environment. Upon starvation, vegetative *Dictyostelium* cells enter the developmental life cycle and start to migrate toward several aggregation centers in the following four to five hours, which is the early

aggregation stage (Figure 2.1B). The aggregation continues until a slug forms, containing about 100,000 cells. The slug explores the environment to search for food and forms a fruiting body if it fails. *Dictyostelium* use conserved chemical signaling, migratory, and developmental mechanisms with more highly evolved eukaryotic cells, such as immune and metastatic cells. However, the shorter life cycle and the simpler genome of *Dictyostelium* make this system a widely used and valuable model to uncover important biological mechanisms (Parent 2004).

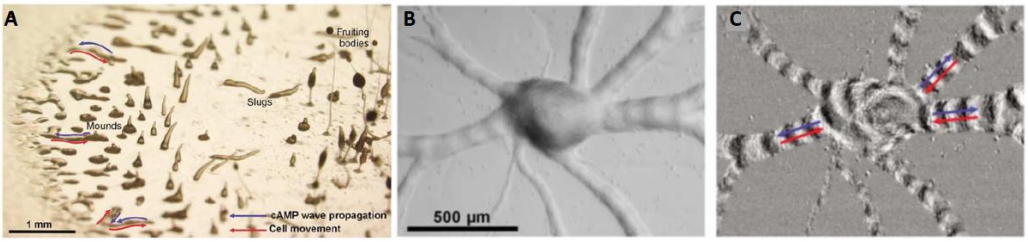

Figure 2.1 – Life Cycle of *Dictyostelium* and cAMP Wave Propagation During Their Aggregation. (A) The life stages of *Dictyostelium* discoideum during their development. Vegetative cells at the left start to develop to mounds through collective aggregation. Mounds further develop to slugs and fruiting bodies which are shown at the right. (B) Bright field image of an aggregation center of *Dictyostelium*. Cells aggregate in a streaming fashion. (C) Overlay image of cell streams and cAMP waves indicating cells migrate in responds to the cAMP signal. Cells migrate towards the aggregation center and cAMP waves propagate in the opposite direction outward of the center. Figures are reproduced from (Dormann & Weijer 2006) with permission.

During the early aggregation phase of their life cycle, *Dictyostelium* cells migrate individually as well as collectively by forming head-to-tail multicellular streams. When exposed to a gradient of chemoattractant, cAMP, these cells quickly

polarize up the gradient and migrate using F-actin based anterior pseudopodial extensions. As shown in Figure 2.2A, cAMP not only induces the cells to migrate directionally, but also stimulates the cells to produce cAMP through the activation of the adenylyl cyclase A (ACA) and release it locally at their rear, which allows them to relay the chemoattractant signal to distal cells and migrate collectively in a characteristic head-to-tail fashion (Figure 2.2B) (Kriebel et al. 2003).

Unlike mammalian cells, *Dictyostelium* form non-integrin-based adhesions with surfaces (Loomis et al. 2012). Although some cell-cell adhesion molecules have been identified, no cadherin-based cell-cell adhesions have been discovered (Wang et al. 2000; Sriskanthadevan et al. 2011).

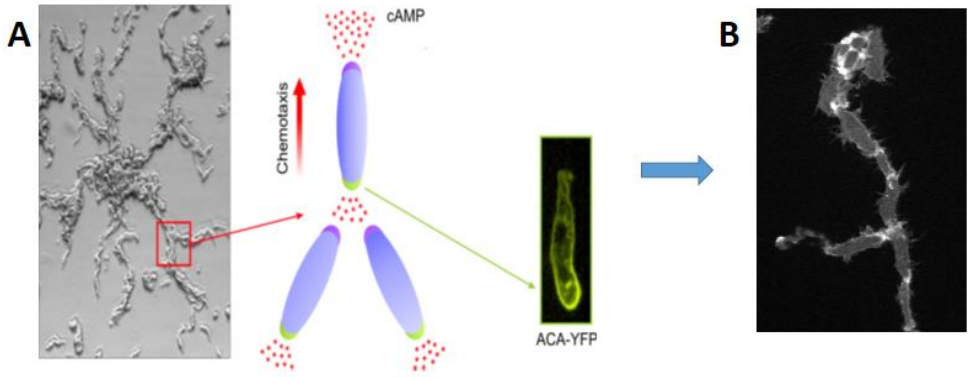

Figure 2.2 –Relay of Chemical Signal in *Dictyostelium* Leads to Head-to-Tail alignment. (A) A model for the chemotactic signal relay in *Dictyostelium*. When stimulated by chemoattractant (red dots), adenylyl cyclase protein is activated at cell back. It produces and releases chemoattractant that can be sensed by neighboring cells so that to propagate chemotactic signal. Figures are reproduced from (Anna Bagorda, Carole A. Parent 2006) with permission. (B) A multicellular stream formed by AX3-Lifeact-RFP cells with cells aligned head-to-tail on glass.

2.2 Cell Migration Assays

Live cell imaging is the primary technique of this thesis. Some experiments were performed by simply placing cells on desired surfaces and imaging their adhesion or spontaneous migration. Other experiments require a better control of directional migration, head-to-tail streaming, and drug treatment. One example, included in Chapter 6, studies the mechanical coupling of protrusion waves on streaming cells during chemotactic migration, where cells are guided by the gradient of a chemical concentration and quickly respond to the change of the gradient. A stable and controllable cAMP gradient is essential for guiding cells to form multicellular streams with head-to-tail alignment. Also, since cells sometimes crawl on top of each other during migration, a confined migration space in the z-direction is required to ensure that the cellular streams are in a single layer and to acquire good quality images. Moreover, to study how cell motion responds to the change of intracellular cytoskeleton, cells were treated with Latrunculin A with gradually increasing doses. Such drug treatment process requires a controlled drug gradient. For all of these needs, I used the under-agarose migration assay that has been previously introduced (Nelson et al. 1975).

The under-agarose-migration assay creates a stable cAMP gradient lasting for up to two hours. As illustrated in Figure 2.3, 0.5% of agarose was cured on a BSA-coated cover glass, and two wells (2 mm in diameter, 4mm center-center apart) were drilled. One well was filled with 1μM cAMP, which diffuses in agarose gel and forms a gradient of cAMP concentration. The other well contained cells that migrated to the

right, guided by the cAMP gradient. Time-lapse images of cells were taken at regular intervals for at least 45 minutes. Cell shape dynamics and principle component analyses were applied to those images.

In some experiments, I used Latrunculin A (LatA) to globally inhibit actin polymerization and studied its effect on cell motion. The mixture of cAMP (1μM) and LatA (different doses were used in experiments) was added into one well, and cells were added into the other well. A gradient of cAMP and LatA concentration was built up in the agarose gel. Thus, when cells migrate towards the other well under the cAMP concentration gradient, they are exposed to increasing concentrations of LatA as well. Based on mathematical models, the concentration of LatA at the edge of the well of cells, where the cells start to migrate, is about 10% of the concentration of the original LatA in the mixture that was added into the other well (Szatmary et al. 2014).

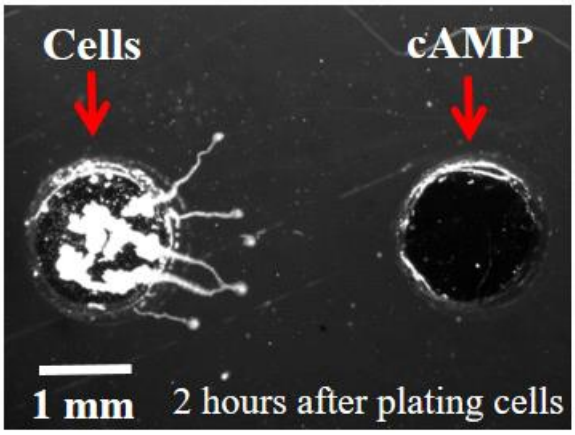

Figure 2.3 – Experimental Set Up of the Under-Agarose Migration Assay. Cells migrate underneath of the agarose gel from the left well to the right well forming multicellular streams. Image was taken under a stereo microscope

2.3 An Introduction of Optical Manipulation on Cells

Optical tweezer, also called optical trap, is a technique that is capable of generating piconewton (pN) forces by focusing a laser light beam on a micron- or nanometer-sized transparent dielectric objects, and moving the object precisely over a small distance (Ashkin et al. 1986). The focused light beam is usually obtained through microscope objectives, and it generates strong electronic gradients near the narrowest region of the focused light beam. Since forces generated by electronic fields correspond to the strength of the electronic field, positioning a particle within a strong electronic gradient results in imbalanced forces acting on the particle, as shown in Figure 2.4. The net force pulls the particle to the center of the light beam, where forces acting on different parts of the particle eventually achieve a balance. When the distance between the particle and the center of the laser light beam is less than the diffraction limit, the net force that the particle receives is proportional to the distance, similar to the force generated in the spring system, described by Hook's Law (Neuman & Nagy 2008).

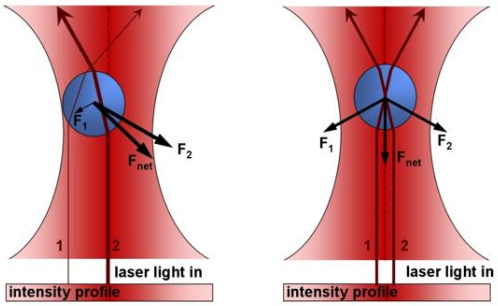

Figure 2.4 – Explanation of A Particle Trapping in Optical Tweezers. Figures are from https://en.wikipedia.org/wiki/Optical_tweezers and reproduced under the CC BY License.

When optical tweezers were initially developed in the 1980s, single optical traps were generated. The new generation of optical tweezers, holographic optical tweezers, came out about a decade ago. They can simultaneously generate multiple optical traps by changing the amplitude and phase of the light to form multiple focus points. This function is fulfilled by integrating a spatial light modulator (SLM) into the light path (Dholakia et al. n.d.).

In recent years, a number of research groups found optical micromanipulation particularly useful for biological objects because of the ability of optical tweezers to precisely control the trapped object's position, orientation, and speed. Micromanipulation via optical trapping forces involves directly focusing a laser beam on cell samples. Due to the extreme focusing of the laser beam in optical traps down to the diffraction limit, considerable photodamage can be inflicted on trapped cells, including the death of cells as noted by Ashkin (Ashkin et al. 1987; Ashkin & Dziedzic 1987). To avoid direct exposure to laser light which causes photodamage, I developed an approach that utilizes the holographic tweezers to indirectly manipulate cells and study cell shape dynamics in a controllable way, which will be further discussed in Chapter 3 and Chapter 5.

2.4 Shape Dynamics in Cell Migration

Eukaryotic cells seldom migrate by simply moving the whole cell body forward. Instead, they actively vary their shapes to migrate and to maintain proper cell-cell contact in groups. These activities include protruding, turning, rotating,

expanding, contracting, etc, which are driven by the dynamical assembling and dis-assembling of the cytoskeleton. Therefore, measuring shape dynamics and progression of motion along cell boundaries provides valuable insight into how cells actively adapt to the varying surrounding environments by cytoskeleton re-organization.

A variety of methods have been used to measure cell shape dynamics (Killich et al. 1993; Alt et al. 1995; Driscoll et al. 2011). I used a snake algorithm to extract cell boundaries and adapted a custom cell shape dynamics Matlab program that was previously developed in Dr. Losert's lab to obtain the measurements on cell boundaries (Driscoll, McCann, et al. 2012).

The Losert lab has applied the shape dynamics analysis method to study the motility of different types of cells (Driscoll, McCann, et al. 2012; Driscoll, Albanese, et al. 2012; Driscoll et al. 2015). *Dictyostelium* cells, for example, migrate in a zig-zag fashion and actively alter their shapes during migration, as shown in Figure 2.5A. They elongate and periodically generate protrusions along the cell membrane. As indicated in Figure 2.5B, protrusions on cell boundaries, indicated by arrows, start at the front of the cell and travel towards the back along either side of the cell body, forming protrusion "waves" on the cell membrane. These boundary protrusion waves are more distinct when the shape dynamics of an individual cell is quantitatively represented in a curvature-time kymograph (Figure 2.5C): the curvature of boundary points are represented in color and aligned vertically according to their position on the cell boundary. The two red lines going across horizontally in the kymograph represent the front and back of the cell, and the slanted red lines indicate traveling

protrusions along the side of cells. Other measurements such as boundary motion and boundary intensity can be represented in a similar way.

The shape dynamic program was initially developed for individual cells, and active boundary protrusion waves are found in these cells. However, how waves are correlated with collective cell migration remains largely unknown. My thesis research explores the robustness of protrusion waves under various perturbations, such as changes in cell-surface adhesions and cell-cell-adhesions, and looks for correlations between boundary protrusion waves and intracellular processes. Thus, I adapted the shape dynamic program to analyze groups of cells and used statistical analysis methods, such as principal component analysis (PCA) and cross-correlation analysis, to process the measurements obtained from shape analysis program.

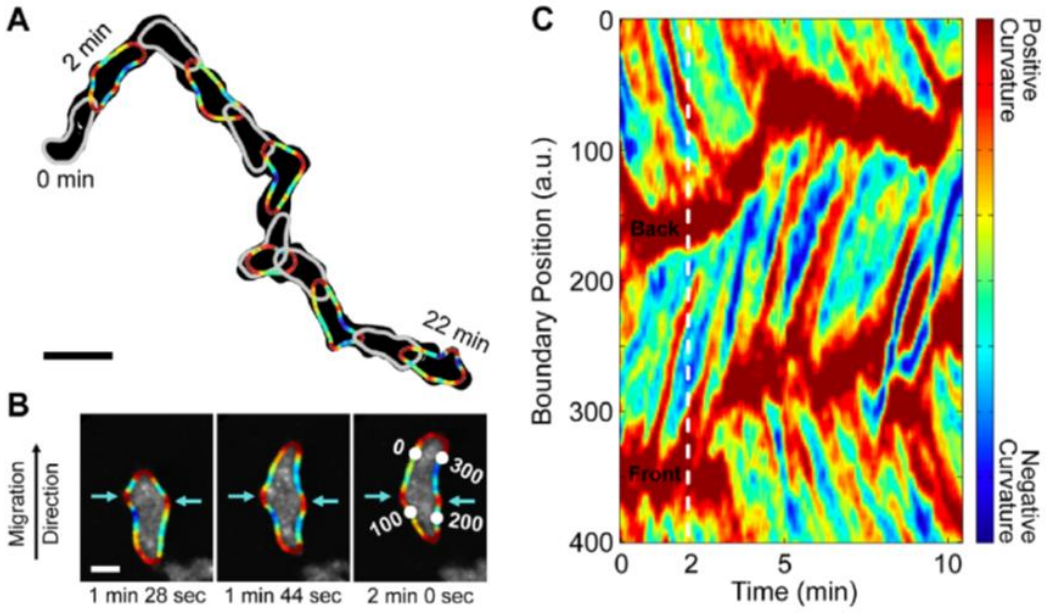

Figure 2.5 – Shape Dynamics of *Dictyostelium*. (A) The trace of a migrating cell formed by overlaying cell boundaries extracted from time-lapse images. (B) Cell boundaries colored according to the curvature of each boundary point. Red represents positive

curvature; blue represents negative curvature. (C) Progression of boundary curvature on a migrating cell represented in a kymograph. Figures are reproduced from (Driscoll, McCann, et al. 2012) under the CC BY License.

Chapter 3: Optical Micromanipulation of Active Cells with Minimal Perturbations: Direct and Indirect Pushing

This chapter is adapted from Wang, Chowdhury, Gupta, and Losert (Wang et al. 2013). Text and figures are reproduced here with permission. Chenlu Wang designed and performed the experiments and analyzed the data.

3.1 Preface

Active movement and the dynamic shape deformation occur in many types of cells. One can perturb the cell movement by attaching an object to cell membrane, or by bringing two cells together to observe how they adapt their movement to each other. Perturbing a moving cell requires precise manipulation of cells and objects. It is possible to directly move cells by focusing a laser beam directly at the cell. This direct optical trapping technique allows for the precise manipulation of cells, but it also causes photodamage to cells as they are exposed to laser light beam during manipulation. This chapter discusses optical-tweezer based techniques I developed for non-invasive optical manipulation of cells. I first developed the direct pushing method, in which I directly trapped a bead and used the bead to push cells. It greatly

reduces photo-damage to cells caused by optical manipulation, and it is further applied to study cell shape dynamics that will be discussed in Chapter 5. During direct pushing, cells are partially exposed to laser light. Thus, I further developed the indirect pushing method that completely avoids direct laser exposure to cells by adding an intermediate bead between the targeted cell and the trapped bead. However, because cells actively move and beads exhibit Brownian motion, the direction of applying pushing force has to be adjusted frequently according to the positions of the intermediate bead and the target cell, which makes the indirect pushing too complicated for manual manipulation. This problem was tackled by integrating real-time image processing and automatic control techniques. Our collaborators developed an automation program that can extract position of cells and beads from real-time images, calculate the optimal direction of applying forces, and then place optical traps accordingly. After many iterations of these steps, the program can manipulate cells in a controllable way. Furthermore, the automation program allows simultaneous manipulation of multiple cells, which brings a great potential of studying cell-cell interactions in a controllable way. In Chapter 5, the visualization of the cytoskeletal dynamics requires fluorescent imaging, which so far is not yet integrated into the automation programs. Thus I used manual direct pushing in chapter 5.

3.2 Overview

The challenge to wide application of optical tweezers in biological micromanipulation is the photodamage caused by high intensity laser exposure to the manipulated living systems. While direct exposure to IR lasers is less likely to kill

cells, it can affect cell behavior and signaling. Pushing cells with optically trapped objects has been introduced as a less invasive alternative, but includes some exposure of the biological object to parts of the optical tweezer beam. To keep the cells further away from the laser, we introduce an indirect pushing based technique for noninvasive manipulation of sensitive cells. We compare three manipulation approaches: direct manipulation, pushing, and indirect pushing. We find that indirect manipulation techniques lessen the impact of manipulation on cell behavior: Cell survival increases, so does the ability of cells to maintain shape and wiggle. Our experiments also demonstrate that indirect pushing allows us to form cell-cell contacts in a controllable way while retaining the ability of cells to change shapes and move.

3.3 Background

Light beams exert small forces on objects, and for objects smaller than tens of micrometers the forces can be designed to "grasp" a particle in an optical beam and move it to a desired position (Ashkin et al. 1986; Ashkin 1992; Grier 2003; Spalding et al. 2008). In recent years, a number of research groups found optical micromanipulation particularly useful for biological objects because of the ability of optical tweezers to precisely control the trapped object's position, orientation and speed (Ashkin et al. 1987; Ashkin & Dziedzic 1987; Kulin et al. 2002; Banerjee et al. 2011). Studies have been carried out on cells with a wide range of sizes: from bacteria which are less than a micrometer to red blood cells which are usually less than ten micrometers and mammalian cells which are tens of micrometers (T cells) (Zhang &

Liu 2008; Lim et al. 2006; Tan et al. 2010; Wang et al. 2011). Micromanipulation via optical trapping forces involves direct focusing a laser beam on cell samples (Neuman et al. 1999; Ericsson et al. 2000; Nascimento et al. 2006). Due to the extreme focusing of the laser in optical traps down to the diffraction limit, considerable photodamage can be inflicted on trapped cells, including the death of cells as noted by Ashkin (Ashkin et al. 1987). A range of assays have shown that focused laser light can also affect cell function without destroying the cell. Aside from heating, the photodamage mechanism has been proposed to be due to the creation of reactive oxygen through two-photon absorption (Berns 1976; König et al. 1996; Svoboda & Block 1994) These damages can affect the cells in various ways that only become visible in careful studies. For example, E. Coli is found to stop replicating after optical trapping (Ericsson et al. 2000). Another investigation found that the internal pH of E.coli and Listeria bacteria declined because of direct trapping (Rasmussen et al. 2008). Even without direct exposure to the focused laser beam, yeast cells are found to divide less after optical trapping (Arneborg et al. 2005).

Since photodamage causes significant negative impact on cells, many in-depth studies have investigated to maximize the cell health by a variety of methods. First, it was found that 830 nm and 970 nm laser wavelengths were significantly less harmful to CHO cells and E.coli cells than the nearby wavelength region from 870 nm to 910 nm (Neuman et al. 1999; Liang et al. 1996). However, another group found only a weak dependence of E.coli viability on wavelength in the range 840 nm to 930 nm, with the total dose of laser light the dominant parameter determining the ability of cells to express genes (Mirsaidov et al. 2008). Moreover, some studies indicate that

the threshold at which light may lead to cell damage is very low compared to the laser power needed for optical micromanipulation: using 1064 nm, Rasmussen found that the internal pH, a measure of viability, of both E.coli and Listeria bacteria declined at laser intensities as low as 6 mW (i.e. 21.6 J for one hour exposure in their study) (Rasmussen et al. 2008). Ayano showed that cell damage to E.coli was linearly dependent on the total dose received and found that cell division ability was affected at a dose larger than 0.35 J (Ayano et al. 2006). Furthermore, Aabo's study indicates that the photodamage to S. cerevisiae is dependent on both the laser power and the accumulated dose (Aabo et al. 2010).

In the studies we mention above, photodamage can be minimized by minimizing light intensity or optimizing laser wavelength, but this also means weakening the manipulation capabilities when directly manipulating cells, and choosing a laser wavelength that is optimal for the particular cell line and biological process, requiring intensive calibration. In addition, preferred wavelengths are generally in the IR, whereas visible lasers are generally less expensive, safer, and more common in labs and industry. Thus, we focus on developing a new indirect pushing approach to minimize the exposure of the manipulated cell to any laser light, so the light intensity and wavelength of the trapping beam no longer notably affect cell viability. Direct pushing is a method by which we manipulate target cells by assistant objects that are directly trapped by laser beams. This minimizes the direct exposure of the target cells to the laser light. Micro-beads, micro-rods, and some other micro-materials can be used as assistant objects.

The pushing approach to cell manipulation research has been carried out previously with the assistance from micro-objects, such as silica beads and erythrocytes (Dao et al. 2003; Grigaravičius et al. 2009). In these studies, the micro-objects were attached to cells and applied forces on cells, and the resulting cell response was investigated. However, for other studies it may be advantageous to not attach the object to the cells permanently. One reason to minimize contact between cell and pushing object is that in cells with very active shapes, for example, *Dictyostelium* cells and human epithelial cells, the shape dynamics and cell activity change upon adhesive contact with a surface (Driscoll et al. 2012; Weber et al. 2012). Hence we prevent the pushing bead and cell from sticking to each other. In this investigation this is straightforward – both cells and beads are negatively charged and so repel each other unless the charges are strongly screened by the buffer medium. Beads are removed away from manipulated cells after manipulation.

We had previously developed a pushing technique which we called indirect optical gripping, in which we utilize holographic optical tweezers to hold six silica beads and form a small 3D trapping pocket (Koss et al. 2011). A single cell can be placed in the trapping pocket and has been transported to the goal position (S Chowdhury et al. 2013). The gripper, as well as some other optical manipulation methods that grip an object touching the cell, is less invasive to the target cell as it reduces the light exposure during optical trapping. But it does not completely eliminate exposure of the target cell to the light cone, and a fixed size or shape of target cells is required for applying these methods easily (Koss et al. 2011). However, many types of motile cells have very dynamic cell shapes and continuously generate

protrusions and retractions on their membranes (Driscoll et al. 2012; Friedl et al. 2001; Barry & Bretscher 2010; Driscoll et al. 2011). In this paper, we introduce a simple pushing approach, shown in Figure 3.1(B), to manipulate cells indirectly, which not only reduces photodamage but also is suitable for manipulating cells with active shapes.

Our direct pushing method still exposes the pushed object to some laser light during the manipulation process. Thus, we also introduce indirect pushing, as shown in Figure 3.1(C), where the laser beam does not overlap with cells. Note that in our indirect pushing, none of the trapped objects touches the cell, whereas in what is commonly called "indirect manipulation" the trapped object usually touches the cell (Grigaravičius et al. 2009).

Previous work estimated photodamage by observing different cell properties: growth and division of cells after optical trapping, the rotation rate of the flagella in bacteria, cloning efficiency of CHO cells, viscoelastic properties, or pH change in the cytosol. Here, we introduce a new simple measure of cell viability: the ability of cells to wiggle and change shape. Unlike most previous work, which assessed viability from static properties, this measure is based on shape dynamics of the cell.

Dynamic shape and motility are significant properties to cells. It is widely believed that extending protrusions is necessary to many types of cells for migration, as cells use protrusions to adhere to surfaces and drag the cell body forward. Also, cells have different protrusion dynamics under different circumstances(Driscoll et al. 2012). Thus, protecting cells from damage to their shape dynamics is crucial when studying the motility and migration mechanism of the manipulated cells. Since the

shape dynamics are driven by cytoskeletal dynamics, such as the polymerization and disassembly of actin filaments, changes of cell shape dynamics indicate that the active mechanical properties of the cell have changed (Gerisch et al. 2004).

To study shape dynamics of manipulated cells, we use amoeboid cells *Dictyostelium discoideum. Dictyostelium* cells have similar chemotaxis and migration mechanisms with some cancer cells; hence their migration mechanism has been widely studied as a model system. When *Dictyostelium* migrates on a surface, cells elongate and periodically generate protrusions along the cell membrane. The protrusions usually start at the front of the cell and then travel to the back on one side of the cell body, so they form a protrusion "wave" on the cell membrane. Often adhesion to the surface strongly affects cells shape and protrusion dynamics. Thus, we focus on suspended cells that cannot adhere to the surface (see Materials and Methods for details). Suspended cells can be manipulated and moved with pN optical force yet still exhibit protrusion waves after indirect pushing, shown in Figure 3.2.

3.4 Results and Analysis

3.3.1 Viability of cells after optical manipulation

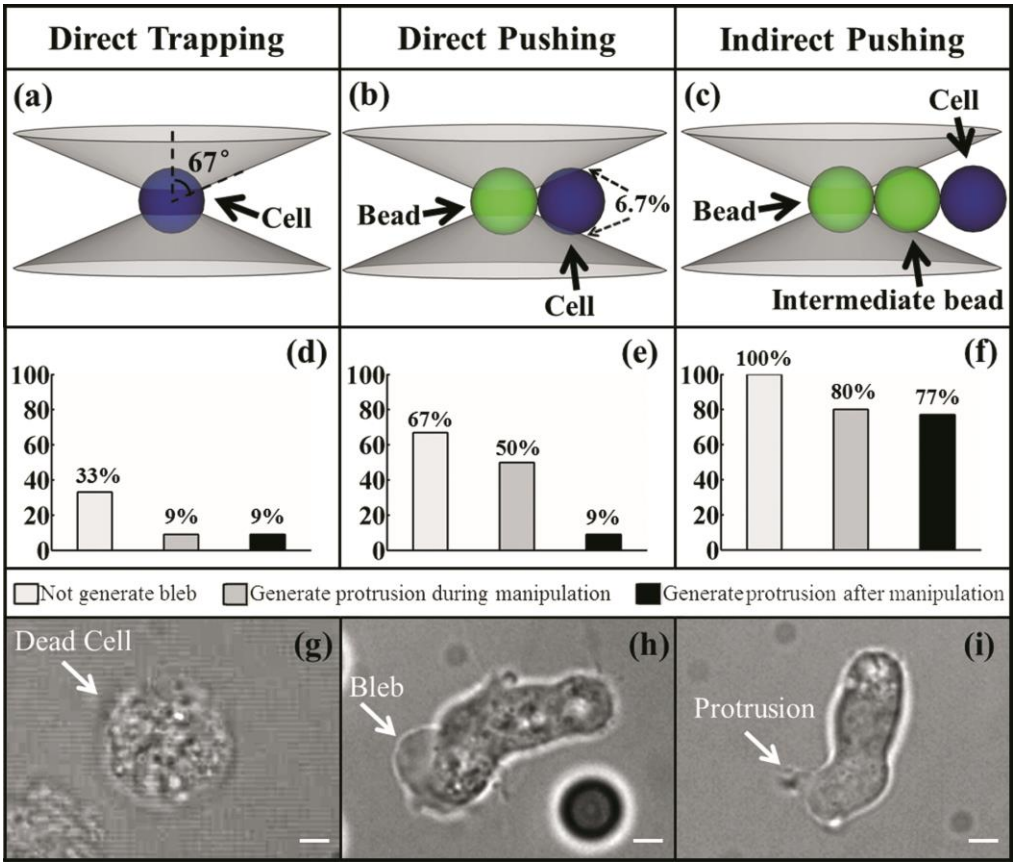

Figure 3.1 - Viability Test of Cells Under Different Optical Manipulation Methods. (a), (b), (c): Schematic of manipulation methods. The diameter of the silica beads and cells is 5 µm. The angular aperture is 67° for the objective. (b): in equilibrium, 6.7% (in volume) of the target cell is exposed to the laser cone. (d), (e), (f): Tests indicating viability of cells with increasing sensitivity: percentage of cells that do not generate blebs (often a precursor to cell death, light gray bars), generate protrusions during manipulation (dark gray bars) and still generate protrusions 5 min after manipulation (black bars). (g), (h), (i): representative figures of a dead cell, a blebbing cell, and a cell that is generating protrusions at its front. Scale bars in (g), (h), (i) are 2 µm.

There are three manipulation approaches that we used on *Dictyostelium* cells: direct trapping, direct pushing, and indirect pushing. To show the configurations of different manipulation approaches and illustrate how the focus laser cones intersect

with trapped beads or cells, we gave schematice figures of these three methods, as shown in Figure 3.1(a-c). The diameter of the silica beads is 5μm. The cells are assumed to be spherical with the size similar to the silica beads. The angular aperture (the angle between the cone and the direction of the laser beam) is 67 °for the objective (comparable to other high NA objectives needed for optical trapping) used in this study. Unlike direct trapping (Figure 3.1(a)), where the laser beam directly focuses on the target cell, the direct pushing approach (Figure 3.1(b)) limits a cell's exposure to light. As shown in Figure 3.1(b), in equilibrium, with the trapped bead at the focal point of the laser, 6.7% (in volume) of the target cell is exposed to the laser cone. However, this is the lower limit of the volume exposed to laser light: If cells are larger than beads (5μm in diameter) or can deform their shape, the exposed volume can be higher. For example, the typical size of *Dictyostelium* cells and epithelial cells are over 15 μm in diameter, and the *Dictyostelium* cells actively deform their shapes. Using a bigger bead (at least 8 μm in diameter in this example case) could possibely keep the cell out of the laser cone, but bigger beads can not be stably trapped against its gravitional force with our optical tweezer system. The third method, indirect pushing, is shown in Figure 3.1(c): The target cell is pushed by an intermediate bead, and the intermediate bead is pushed by another bead that is directly trapped by the laser beam. These two beads and the cell do not stick to each other (e,g. if the manipulation involves getting cells together into larger collections, beads have to be removed from cell group). The directions of the forces that the directly trapped bead applies on the intermediate bead are tuned depending on the relative position of the intermediate bead and the target cell. How to reliably push on the cells indirectly was

described elsewhere (Thakur et al. 2012; Thakur et al. 2014). When the target cell is pushed indirectly, the cell remains at least several microns away from the directly trapped bead, and thus is not directly exposed to the light cone of the trapping laser.

Viability tests of these three manipulation methods were performed on a set of suspended *Dictyostelium* cells (21 cells for direct trapping, 18 cells for direct pushing and 26 cells for indirect pushing), and cells were actively deform their shapes before manipulation. To maintain constant conditions, the output laser power was set to be 0.2 W, and the manipulation times remained between 40 to50 seconds, (i.e. (laser power) * (exposure time) = 8~10 J). Four criteria were used here to estimate the photodamage (Figure 3.1(d-f)): survival, the generation of blebs on the membrane, the generation of protrusions during manipulation, and the generation of protrusions after manipulation.

Note that the 532nm green laser we use is known to be harmful to cells. Thus our study presents a worst case scenario that makes it easier to detect differences in photodamage with different manipulation methods.

Dead *Dictyostelium* cells (shown in Figure 3.1(g)) are easy to distinguish from living cells, because they do not keep their membrane intact. All cells survived after all three manipulation approaches (data not shown). However, some living cells generate blebs on membrane during manipulations, which usually indicates that cells cannot retain their cortical tension and are unhealthy (Janson & Taylor 1993; Mills et al. 1998; Gerisch et al. 1995). A representative cell with a membrane bleb is shown in figure 3.1(h). As shown in Figure.3.1(d-f), the percentages of cells that generate blebs

during trapping drops from 67% to 0% from direct trapping approach to indirect pushing approach.

Dictyostelium cells migrate, and they need to extend protrusions in order to move forward. When *Dictyostelium* cells migrate on a surface, they generate new protrusions every 20 seconds (Driscoll et al. 2012). Thus, during the 45 seconds manipulation in this viability test, a healthy cell normally will be able to generate protrusions. But, as shown in Figure 3.1(d-f), only 9% of the cells under direct trapping extend protrusion during the manipulation, and this number increases to 50% and 80% when using the direct pushing and indirect pushing methods respectively, which reveals that only indirect pushing approach does not have significant negative impact on cells in terms of generating protrusions in a short time of optical trapping.

Nevertheless, photodamage could have long term effect on cells. To study that, cells have been observed for at least 5 minutes after each manipulation. As shown in Figure 3.1(d-f), only after indirect pushing, most of the cells (77%) are found to be able to generate protrusions in 5 minutes after manipulation, while only 9% of the cells could generate protrusions after the other two types of manipulations. Thus, the indirect pushing approach shows no significant long term photodamage on *Dictyostelium* cells.

3.3.2 Shape analysis of cells after optical manipulation

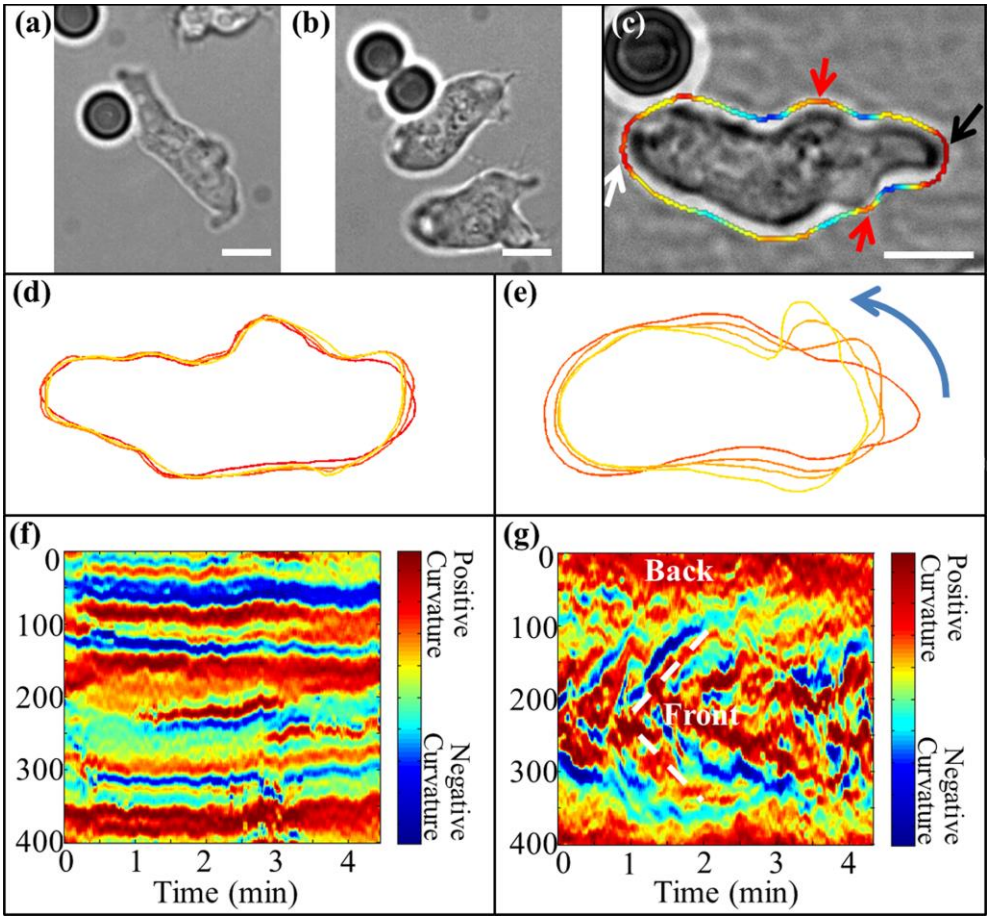

Figure 3.2 - Shape Analysis of *Dictyostelium* Cells After Optical Manipulation. (a): A cell that is directly pushed by a silica bead. (b): A cell that is indirectly pushed by a silica bead through an intermediate bead. (c): Extracted outlines of a representative polarized cell (Red: positive curvature; Blue: negative curvature) (d): Overlaid shapes of a cell manipulated by direct pushing. (20 seconds apart; red:initial shape). (e): Overlaid shapes of a cell manipulated by indirect pushing. (2 seconds apart; red:initial shape). (f): Curvature vs. time plot of a cell manipulated by direct pushing. (g): Curvature vs. time plot of a cell manipulated by indirect pushing. Scale bars in (a), (b), (c) are 5 µm.

The viability test indicates that the indirect pushing method does not cause long-term photodamage on generation of new protrusions, but the shape dynamics of the cell could be changed. As we learned from crawling *Dictyostelium* cells, protrusions should not only be generated but also travel on cell membrane like a wave. Thus, a shape dynamics analysis method that we previously developed has been used to analyze shapes of cells after optical trapping. The image processing details have been described in reference (Driscoll et al. 2012).

The shapes of cells after direct or indirect pushing are analyzed as shown in Figure 3.2. In Figure 3.2(b), indirect pushing of a cell towards another cell is shown. In both Figures 3.2(a), (b), *Dictyostelium* cells maintain a polarized, elongated shape. The polarized end that generates new protrusions is considered as the "front" (i.e. "head") of the cell, and the other end is the "back" (i.e. "tail") of the cell.

To analyze shape dynamics, 400 points on the cell boundary are extracted by an active contour algorithm(Chenyang & Prince 1998). The curvature along each point on the boundary is calculated and used as a metric for shape. Figure 3.2(c) shows an image of a representative cell with its extracted boundary, colored with curvature value. Two main high curvature regions are seen (red indicates high curvature). One in the front (black arrow) and the other in the back (white arrow). In addition, there are small high curvature regions (small red regions) (red arrows).

To visualize shape dynamics, we overlay cell shape outlines from different time points. Figure 3.2(d) shows overlaid cell shapes after direct pushing (the cell is the same as in the Figure 3.2(a). As we can see, although the cell retains its polarity and looks similar to a healthy cell (shown in Figure 3.2(c)), its overall shape does not

change notably in 80 seconds, indicating that the cell active shape changes after direct pushing. After indirect pushing, however, (the cell in the Figure 3.2(b)), cells continue to change shape (Figure 3.2(e)). Cell shape dynamics do not seem to be affected by indirect pushing: Localized protrusions travel from the front to the back of the cell (blue arrow), consistent with our prior observations.

To visualize and quantify shape dynamics over minutes, we plot a kymograph (space time plot) where color indicates local curvature. Each vertical line in the kymograph represents one shape outline at a different time, for a total of 4.5 minutes (Figures 3.2(f), (g)). After direct pushing the shape of the cell remains unchanged with time: The front and back, as well as additional small protrusions form multiple straight red lines in Figure 3.2(f). After indirect pushing (Figure 3.2(g)), tilted red lines are visible that start at the front of the cell, indicating protrusions that travel as a wave from the front of the cell to the back (white dot lines), similar to what we reported previously on healthy *Dictyostelium* cells(Driscoll et al. 2011).

3.3.3 Indirect pushing allows for studies of cell-cell adhesion.

Next we demonstrate an example how indirect pushing may be used to address a biological question. We focus on the question that how cell-cell contact affects cell behavior. Often cell-cell contact is studied when cells are anchored to a surface and thus cell-cell contact competes with cell-surface contact. However, many cells can at least temporarily be brought into suspension or prevented from anchoring to the surface. In that case they also lack the ability to push off the surface and move, and thus need to be manipulated in order to get in contact with other cells in a controlled way.

We first investigated cell-cell adhesion in cells suspended in distilled water. Unlike mammalian cells, the amoeboid cells we investigate (*Dictyostelium*) have special organelle to survive in distilled water. When two cells were pushed together we find that they did not form stable cell-cell adhesion. Instead, after indirect pushing stopped, they moved apart immediately, though cells were viable by our strictest standards. They maintained their shape dynamics until moving out of the field of view 19 minutes after manipulation.

To assess whether this lack of cell-cell adhesion was related to the absence of buffer medium which screens charges and limits repulsive forces between cells, we used cells in buffer, but on PEG coated glass slides to prevent cell-surface adhesion. We find that cells in buffer are able to stick to others when they are pushed into contact. This process is shown in Figure 3. In the Figure 3(a), (b), two suspended cells are generating new protrusions (black arrows) before manipulation. A bead (white arrow) is directly trapped by an optical trap and moved towards an intermediate bead and cell A. The indirect pushing process is shown in Figure 3(b), (c), (d) as these two cells are arranged along their polarization direction (head-to-tail) and are pushed to form direct cell-cell contact. This manipulation process lasts for about 40 seconds. After the manipulation stops, these two cells still extend protrusions (black arrows) and retain dynamic shapes. The cells remain in contact and eventually form a clump several minutes after manipulation, as shown in Figure 3(h). We have carried out this procedure 8 times with success, demonstrating that it is possible to generate cell-cell contact with controlled polarity for biophysical investigations.

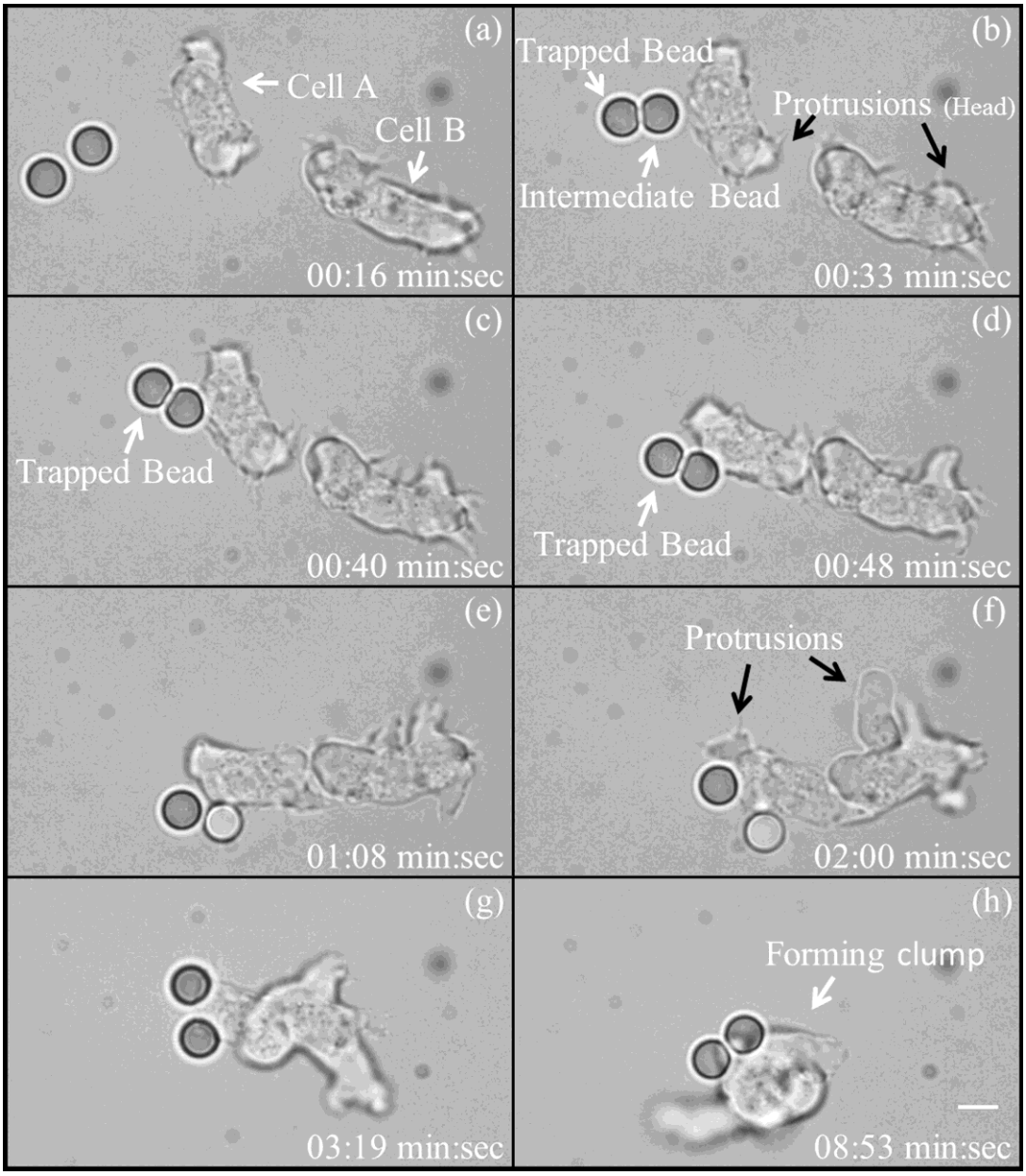

Figure 3.3 - Indirect Pushing Of Two *Dictyostelium* Cells Allows For Tests Cell-Cell Adhesion With Controlled Cell Polarity. (a~b): A bead is directly trapped by the optical trap and moved towards another bead and cell A. (c~d): Cell A is indirectly pushed by the trapped bead through the intermediate bead. (e): The manipulation stops after one minute, and the two *Dictyostelium* cells are able to adhere together. (f~h): The two adhered *Dictyostelium* cells extend protrusions and form a clump in the following 8 minutes. Scale bar: 5 µm.

3.3.4 Manipulating epithelial cells via indirect pushing.

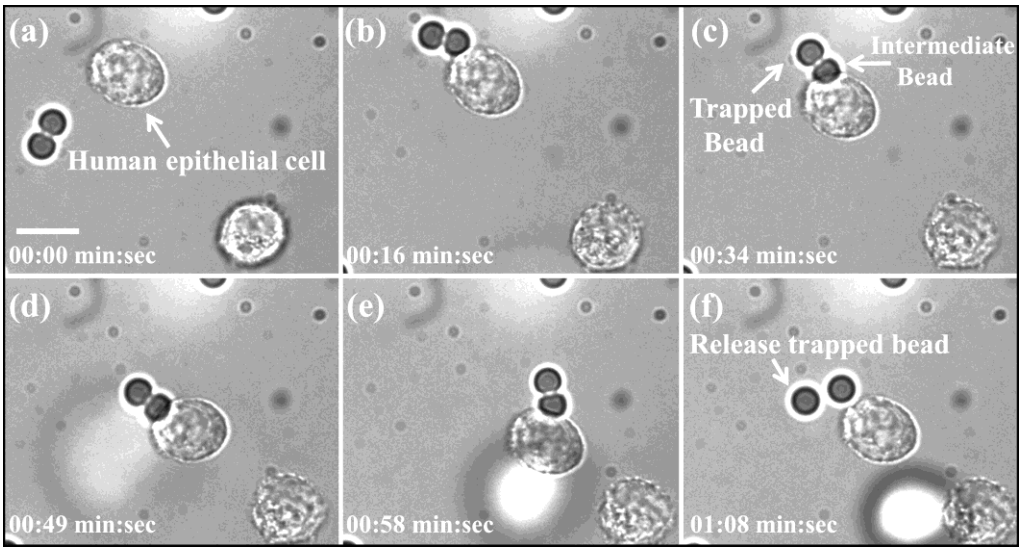

Figure 4 - Indirect Pushing of an MCF-10A Cell. (a): A bead is directly trapped by the optical trap and pushed to another bead, and move towards an MCF-10A cell. (b-e): Cell is indirectly pushed from a different direction by the trapped bead through the intermediate bead. (f): After manipulation, the trapped bead is released from trapping. Scale bar in (a): 10 µm.

The indirect pushing method introduced in this paper is useful for non-adherent cells. But it also can be used on adherent cells, taking advantage of the slow process of cell-substrate adhesion. Mammalian cells usually adhere to surfaces or an extracellular matrix, and utilize cell-surface adhesion to migrate. When adhered to a surface, these cells cannot be manipulated with optical tweezers, since adhesion forces are in the nN range, stronger than optical forces. However, there is an up to half an hour delay between the time cells settle to the surface and the time they start to adhere, as e.g. reported in reference(Dubin-Thaler et al. 2004). The delay time can

be tuned by varying the surface coating concentration. As an example, we studied MCF-10A Human Breast Cells that are shown in Figure 4. After placement in an 8-well chamber (Ibidi, Martinsried, Germany), it was possible to push cells indirectly with silica beads before the cells stick on the surface for more than 30 minutes.

3.5 Conclusion and Future Work

This study presents evidence that indirect pushing significantly reduces the potential photodamage to target cells. By indirect pushing we mean optical trapping of beads, which push another bead, which in turn pushes on a cell. Unlike direct manipulation or direct pushing (where cells are directly pushed by beads and parts of cells are still exposed to the trapping beam) indirect pushing does not expose cells to laser light. Indeed, cells remain viable even when hundreds of mW of laser power at 532nm, i.e. in a harmful wavelength range, is used for manipulation. Our study focused on the worst case scenario, manipulation with laser light of a wavelength that is known to harm cells, to demonstrate that the indirect pushing method is broadly applicable for a wide range of laser wavelengths.

In the viability study, most of the indirectly pushed cells are able to maintain their polarized shapes during manipulation. More importantly, most cells maintained their shape dynamics after manipulation. Thus, indirect pushing may be applied to study many interesting biological questions regarding cell motility or mechanical properties of pairs or groups of cells, the small building blocks of tissues and organs.

One of the challenges of manual indirect pushing is that the intermediate bead could slip out from the configuration. Thus, it requires constant tuning of the pushing direction. However, by integrating robotic planning techniques, it is not a challenge to

reliably execute indirect pushing operations. The robotic control is achieved through a feedback loop that takes the current states of the trapped bead, intermediate bead, and the target cell into account to produce optimal action to move the trap so that the cell can be transported towards the desired goal location. The instability of the intermediate bead due to random Brownian motion does not affect the stability of the controller. The authors were even successful in manipulating smaller cells, e.g., Yeast that have smaller contact area between intermediate bead and cell which makes the pushing more challenging (Thakur et al. 2012; Thakur et al. 2014). Besides, we have developed an approach that is able to automatically trap multiple beads at the same time and move them on different trajectories using holographic tweezers, which will allow us to indirectly push multiple cells to different positions to form collective cell patterns in a controlled way (S Chowdhury et al. 2013; Chowdhury et al. 2012; Sagar Chowdhury et al. 2013; Banerjee et al. 2012).

3.6 Materials and Method

3.5.1 Optical Setup

Multiple optical point traps are generated by using a 532nm green laser (Nd:YAG 5 W, Spectraphysicics, Millenia) coupled into a Nikon inverted light microscope, integrated with a Biorryx system (Arryx Inc.). Though the 532nm green laser is known to be harmful to cells, it presents a worst case scenario that makes it easier to detect differences in photodamage with different manipulation methods. Our indirect pushing method keeps cells viable even when hundreds of mW of laser power at 532nm is used for manipulation. A spatial light modulator has been built on this setup to customize the multi-traps arrangement within three dimensional spaces.

With a Nikon 60X NA 1.4 oil immersion objective, the Biorryx system can arrange up to 100 point traps within the operating region of about 100 μm*100μm and about 10 μm above or below the focal plane. The same objective was used for both optical trapping and imaging. The cell manipulation process and long-term cell shape dynamics were imaged at 15 frames per second by a CCD camera (Foculus Inc.) and at 1 frame per second by CCD camera (Ueye from IDS GmbH) representatively.

3.5.2 Preparations of *Dictyostelium* cell, Human MCF-10A Mammary Epithelial Cells and silica beads

Dictyostelium discoideum lives as single amoeba cell when there is sufficient nutrition in the environment. Upon starvation, wild-type *Dictyostelium* are able to sense their neighboring cells and collectively migrate to an aggregation center, and eventually form a slug, which helps the whole cell group move faster during the food searching. The wild type *Dictyostelium* (AX3) cells were grown in HL-5 medium at the concentration no higher than $5*10^6$ cells/mL at 21 ℃ (Sussman 1987). For experiments, we starved and developed cells for 5 hours in development buffer (DB: 5 mM KH_2PO_4; 5 mM $Na_2HPO_4*7H_2O$; 2 mM $MgSO_4$; 0.2 mM $CaCl_2$) with pulses of 75 nM of cAMP every 6 mins, as described in other papers (Devreotes et al. 1987; McCann et al. 2010). Developed cells were harvested after 5 hours by centrifuging 500μL of liquid from develop flask at 9000rpm for 3 minutes. The cell pellets were dissolved in 500μl of distilled water or phosphate buffer (PB: 5 mM KH_2PO_4; 5 mM $Na_2HPO_4*7H_2O$).

The MCF-10A cells were grown in an incubator in which the humidified atmosphere was kept at 37 ℃ and 5% CO_2, in the DMEM/F12 media with 5% horse

serum, 10μg/ml insulin (Invitrogen), 10 ng/ml EGF (Peprotech, Rocky Hill, NJ), 0.5 μg/ml hydrocortisone (Sigma, St. Louis, MO), and 100 ng/ml cholera toxin (Sigma, St. Louis, MO). For experiments, cells were harvested from the culture flask by adding Trypsin (Invitrogen), and the supernatant were centrifuged at 350 rpm for 5 minutes. The cell pellet was dissolved in 6mL growth media and 10μL cells were added into a well of a μ-slide 8 well chamber (Ibidi, Martinsried, Germany)

Silica beads (5 μm) are used as optical trapping assistants in indirect manipulation approaches. Micro-beads solution was prepared by mixing 2 μl original silica microspheres solution (Bangs Laboratories, Fishers, IN) with 1 ml distilled water.

3.5.3 Suspended cells and beads

In order to have enough time to manipulate cells and beads, the electrostatic force is utilized in experiments with *Dictyostelium* cells to keep cells and beads from sticking to the glass surface. The surface of cover glass, *Dictyostelium* cells, and silica beads are all negatively charged. They repel each other because of the Coulomb force when they get close. After adding cells into normal buffer, as in a standard experiment protocol, cells gradually settle to the surface from suspension. Once placed on the surface, they adhere and start to spread, i.e. form a growing contact area with the surface. The reason that they are able to overcome the repellent Coulomb force is that the cations in the buffer screen out the negative charge on cell membranes and surfaces (Socol et al. 2010). In this study, we add cells and beads into distilled water, so that the Coulomb force between cells and glass surface can keep them suspended for manipulation. When studying cell-cell interaction, the lack of

charge screening may also lead to repulsion between negatively charged cells. Thus, poly (ethyleneglycol) (PEG) coated glass slides (from MicroSurface, Inc.) are also used in the experiment that is shown in Figure 3.3 to keep cells from adhering to the surface.

Chapter 4: *Dictyostelium* Cells Migrate Similarly on Surfaces of Varying Chemical Composition

This chapter is adapted from McCann, Rericha, Wang, Losert, and Parent (McCann et al. 2014).Text and figures are reproduced here with permission. Section 4.3 summarizes and explains the previous experimental results and analysis finished by Colin McCann and Erin Rericha, which are not part of my dissertation. These results will be referred to as "our results" throughout this chapter. It is included here as understanding the previous hypothesis and results is critical to the understanding of the subsequent experiments and analysis. The work completed as part of my dissertation research is introduced in Section 4.4. Chenlu Wang performed the experiments and analyzed the data in Section 4.4. Colin McCann and Erin Rericha performed experiments and analyzed the data in Section 4.3.

4.1 Overview

Cell migration requires binding between cells and external substrates with moderate strength because sufficient adhesion is needed for pseudopods to anchor on surfaces and the whole cell body to be pulled forward, and adhesion needs to be weak enough for the cells to detach from surfaces. Mammalian cells strongly adhere to surfaces to be able to sense extracellular conditions and adapt their migration

accordingly, a phenomenon termed mechanotransduction. Mechanotransduction is found to be mediated by transmembrane integrins. However, amoeboid cells do not form integrin-based focal adhesions. We wonder whether mechanotransduction also occurs when these cells use non-integrin-based adhesion to migrate. We find individual *Dictyostelium* actively maintain optimal cell-surface contact area and migrate similarly on surfaces with different chemical compositions, which is regulated by the cytoskeleton. However, during collective migration, the cell-surface contact area and the migration pattern are strongly affected by surface composition, suggesting the formation of cell-cell adhesion alters cell-surface adhesion and the mechanism that cells migrate on different surfaces.

4.2 Background

Migrating on surfaces of different compositions is crucial for cells to fulfill many biological and pathological functions, such as immune responses, wound healing and cancer metastasis (Ridley et al. 2003). The mechanism of cells adhering to surfaces varies widely and is mainly determined by cell types (Friedl & Wolf 2010). Some types of cells, such as mesenchymal cells, form strong adhesions with surfaces, termed focal adhesions, which are mediated by integrins. Integrins are major transmembrane receptors which facilitate cells to adhere to surfaces and sense the surrounding environment. Thus, integrins play an important role in mechanotransduction (Wolfenson et al. 2013). Amoeboid cells, such as *Dictyostelium* cells and neutrophils, form non-integrin-based cell-surface adhesions.

Cells maintain their shapes and cell-surface adhesions by regulating cytoskeletal dynamics, including polymerization of actin and assembly of myosin II (Lecuit et al. 2011). These dynamic processes are often mediated by integrins. Integrins interact with cytoskeleton through adaptor proteins, such as Talin, which binds to both integrins and actin (Wolfenson et al. 2013).

In the wild, *Dictyostelium discoideum* exist in soil, an environment with diverse conditions, and are exposed to different types of surfaces. They live as single amoeboid cells when there is sufficient nutrition in the environment. Upon starvation, wild-type *Dictyostelium* are able to sense their neighboring cells and collectively migrate to eventually form a slug or a fruiting body, which helps the whole cell group survive in harsh environment conditions (Müller-Taubenberger et al. 2013). They aggregate by secreting and chemotaxing toward cAMP signals forming multicellular streams with head-to-tail alignment. Although several adhesion receptors on cell membrane have been identified in *Dictyostelium*, the molecular mechanism of cell-surface adhesion remains largely unknown (Cornillon et al. 2000; Fey et al. 2002). Two identified receptors, SibA and SibC, have homologues with mammalian integrin β chains, which could potentially interact with talin, but no actual integrin homologues are found (Cornillon et al. 2006; Cornillon et al. 2008). However, they express two homologues of talin, Talin A and Talin B, with distinct functions. Compared to Talin B, Talin A is more related to talin in mammalian cells, and it is found to be involved in a couple of processes in single cell migration, including cell-substrate interaction (Kreitmeier et al. 1995; Niewöhner et al. 1997).

In this study, we were motivated to understand how *Dictyostelium* adapt their migration to complex extracellular environments by plating them on surfaces with different chemical compositions. Cell-substrate adhesion and collective migration were investigated in both individual cells and cell groups. In addition, we used drugs and mutant cell lines to observe activities of actin, myosin II, and talin under perturbations so that to probe the roles of them in cell migration. These experiments and analysis provide us a new understanding of cell-substrate adhesion and insights in underlying intracellular mechanisms during collective migration.

4.3 Previous Results and Analysis from McCann and Rericha's Research

4.3.1 Non-specific cell-surface adhesion is actively regulated

Unlike mammalian cells who form integrin-mediated focal adhesions, *Dictyostelium* are thought to form non-integrin-mediated adhesions with substrates (Eichinger et al. 2005; Décavé et al. 2002; Loomis et al. 2012). This type of membrane-surface interaction is expected to be largely determined by the physical properties of the external substrate, such as electrostatic charges and hydrophobicity (Socol et al. 2010). Thus, we investigated the cell-surface adhesion on surfaces with different chemical compositions: bovine serum albumin (BSA) coated glass, poly-L-lysine (PLL) coated glass, acid-washed glass, and perfluorinated carbon chain coated glass.

To access the strength of cell-surface adhesion, we measured the relative contact area of cells, which is the ratio of the surface contacting area of a cell to the projected area of the cell. The surface contacting region was visualized under Interference Reflection Microscopy (IRM), and the whole cell was visualized under

bright-field microscopy (Barr & Bunnell 2009). Cells exhibited visibly similar contact area on four surfaces (Figure 4.1A), and the following quantitative analysis indicated that the steady-state surface contact covered 20% to 30% of projected cell areas (Figure 4.1C, right plot). To further evaluate cell-surface adhesion, shaking adhesion assay experiments were used. Cells were plated and allowed to adhere to different surfaces. After been shaken orbitally at a controlled speed for a certain period of time, some cells were peeled off surfaces and then washed away. The numbers of surviving cells were found to be similar on all tested surfaces, indicating the strength of cell-surface adhesion is comparable when cells migrate on these distinct surfaces.

In addition to cell-surface adhesion, other properties of cell migration were investigated, such as the polarity of cells, which was found to be similar on all tested surfaces. Cells also exhibited similar migration speed on different surfaces, as shown in Figure 4.1C, left plot.

The underlying mechanism of cells maintaining similar adhesions on distinct surfaces remains unclear. Cytoskeleton provides physical integrity of cells, and it is often considered as a generator of forces that regulates cell-surface adhesion (Murrell et al. 2011; Reichl et al. 2008; Cuvelier et al. 2007; Robinson & Spudich 2004). To verify this hypothesis, we disrupted actomyosin cortex by using latrunculin A (LatA) and observed the change of cell-surface adhesions. LatA inhibits the polymerization of actin filaments so that to disrupt actomyosin cortex (Parent et al. 1998). Under the treatment of LatA, cells adopted a spherical shape and adhered on four surfaces with the significantly different relative contact area (Figure 4.1B). The relative contact

area of cells was dramatically larger on PLL and FCC coated surfaces than on glass and BSA coated surfaces, which was strongly correlated with the inherent adhesivity of these surfaces (Schindl et al. 1995). This finding suggests, in the absence of actomyosin cortex, cell-surface adhesion is mainly determined by the type of surfaces instead of being actively regulated by actomyosin force.

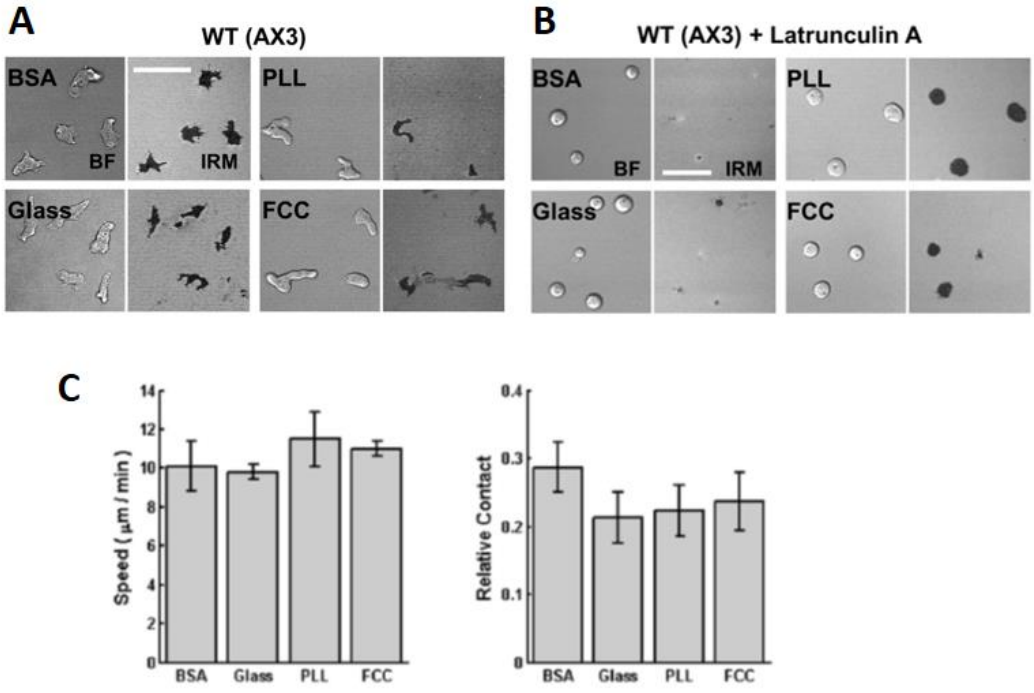

Figure 4.1 – Cell-Surface Contact Area and Cell Migration on Surfaces with Different Chemical Composition. (A) Representative bright field images and IRM images of WT *Dictyostelium* cells (AX3) on 4 different surfaces. Scale bar: 35 μm. (B) Representative bright field images and IRM images of Latrunculin A treated AX3 cells on 4 different surfaces. (C) Average migration speed and the relative surface contact area of AX3 cells on 4 different surfaces.

4.3.2 Myosin II is required for strong cell-surface adhesions

Cell-surface adhesions were significantly altered by LatA treatment, suggesting that the interaction between the cell membrane and surfaces is actively regulated by the cytoskeleton. The cytoskeleton is found to be able to adapt to different external substrates through actomyosin forces, which is generated by forming protrusions via actin polymerization and by controlling membrane tension via contractions mediated by myosin II (Jay et al. 1995). Thus, to understand how cell-surface adhesion is regulated by myosin II, we measured the surface contact of cells lacking myosin II (myoII- cells). These cells exhibited migration defect as they cannot retract their backs (Meili et al. 2010). As shown in Figure 4.2A, myoII- cells migrating on PLL and FCC surfaces exhibited larger surface contact areas than those migrating on BSA and glass surfaces. Compared to wild-type cells (AX3 cells), the relative surface contact area of myoII- cells significantly increased on PLL and FCC surfaces (Figure 4.2B). These surfaces were considered to have higher adhesivity than BSA and glass surfaces in previous studies. However, absence of myosin II did not significantly change cell adhesion on surfaces of low adhesivity, i.e., glass and BSA coated surfaces. This finding suggests that cell-surface adhesion to high adherent surfaces is highly correlated with the contractile ability of cells mediated by myosin II, but cell-surface adhesion to low adherent surfaces is mainly regulated by actin and independent of membrane contraction.

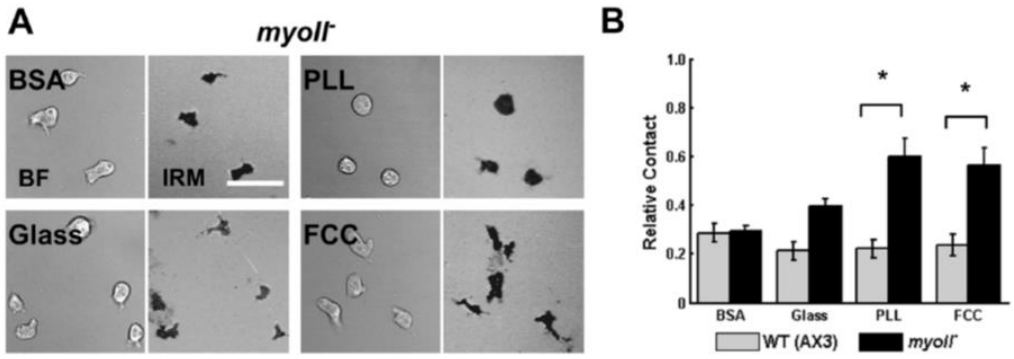

Figure 4.2 –Cell-Surface Contact Area of myosinII null Cells on Surfaces with Different Chemical Composition. (A) Representative bright field images and IRM images of *myoII*- cells on 4 different surfaces. Scale bar: 35 μm. (B) The average relative surface contact area of AX3 cells and *myoII*- cells on 4 different surfaces.

4.4 Results and Analysis

4.4.1 Actin contributes differently to the regulation of cell-surface adhesions on distinct surfaces.

As revealed in the above experiments, cell-surface adhesions were significantly altered by depolymerization of actin. To further examine the effect of actin polymerization on adhesions, we measured the relative contact area of cells treated with different concentrations of Latrunculin A (Section 4.6.1 Materials & Method). BSA and PLL coated surfaces were chosen as representative surfaces that respectively display lower and higher contact area after Latrunculin A treatment. Experiments were repeated for 3 times, and images of 20~30 cells were taken for each experimental conditions. Representative images showing phalloidin staining of Latrunculin A-treated cells on both BSA- and PLL-coated surfaces are shown in

Figure 4.3A. Interestingly, we found that cells plated on BSA are more resistant to actin disassembly compared with cells plated on PLL. As low as 0.5μM Latrunculin A significantly increased the relative contact area of cells plated on PLL (Figure 4.3B). In contrast, cells plated on BSA required a minimum of 5μM Latrunculin A before a significant decrease in relative contact area could be measured (Figure 4.3B). Indeed, from images we noticed that at equivalent Latrunculin A concentrations the phalloidin staining appears to be weaker in cells plated on PLL, compared to BSA, particularly at 0.5μM Latrunculin A (Figure 4.3A). These findings indicate that (i) *Dictyostelium* cells regulate their surface contact area and cell-surface adhesion in an actin-dependent manner and that (ii) actin contributes differently to maintain optimal surface adhesion on different surfaces.

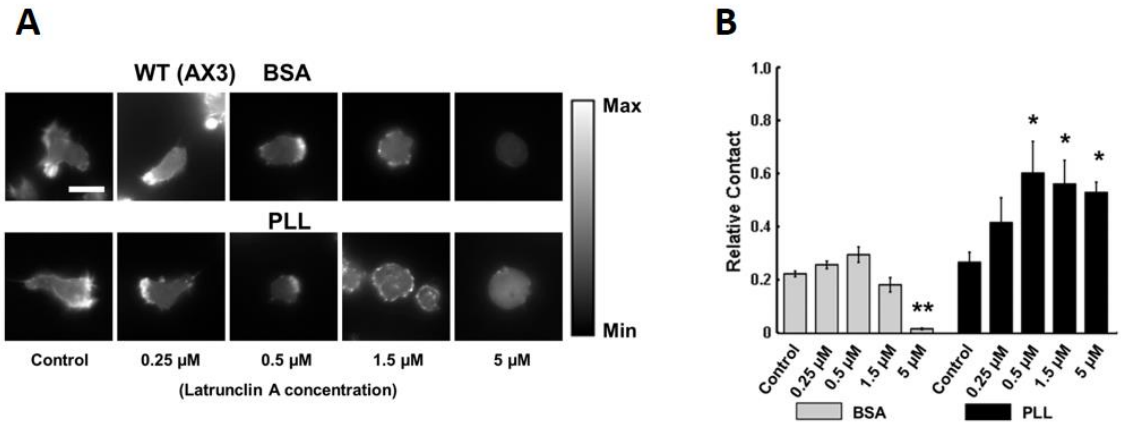

Figure 4.3 – Cell-Surface Adhesion is Altered by Latrunclun A Treatment in a Dose-dependent Manner. (A) Representative TRITC-phalloidin fluorescent images of Latrunculin A-treated WT (AX3) cells on BSA and PLL surfaces. Scale bar = 10μm. (B) Quantification of the relative contact area of cells on BSA and PLL surfaces. AX3 cells were treated with different Latrunculin A concentrations, as indicated. * indicates statistical significance compared to the control condition (*: $p<0.05$, T-test; **: $p<0.005$, T-test)

4.4.2 Talin A is required for weak cell-surfaces adhesions

To further understand the molecular mechanisms that regulate cell adhesion and migration in *Dictyostelium*, we examined how surface composition affects contact area in cells lacking talin A (talin A- cells). Similar to the finding of previous studies (Niewöhner et al. 1997), we found that talin A- cells exhibit less cell-surface contact when plated on BSA compared to WT cells (Figure 4.4 A, C&D). In contrast, there is no significant differences in the contact area between talin A- cells and WT cells when cells were plated on the other more adherent surfaces, except for PLL where the talin A- cells showed higher contact area (Figure 4.4D). For these experiments, the talin A- parental cell line AX2 was used as a control. These cells behave similarly to AX3 cells on the various surfaces tested (Figure 4.4B). As discussed in the last section, cells regulate actin cortex to reinforce cell-surface adhesion when they migrate on less adhesive surfaces, *e.g.* on BSA. Our finding that talin A- cells exhibit less cell-surface contact on such surfaces suggests that talin A is required when cell-surface adhesion is enhanced by cortical actin.

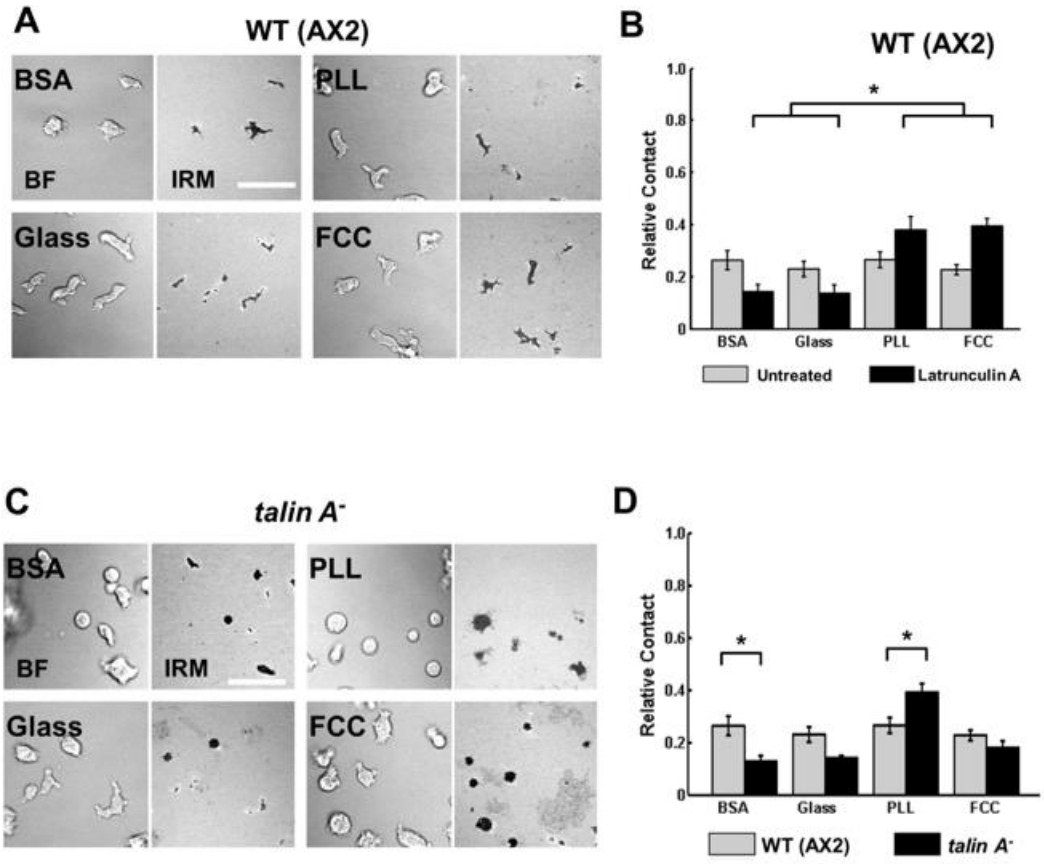

Figure 4.4 –Cell-Surface Contact Area of *talin A null* Cells on Surfaces with Different Chemical Composition. (A) Representative bright field images and IRM images of AX2 (WT) cells on 4 different surfaces. Scale bar: 35 µm. (B) The verage relative surface contact area of AX2 cell with Latrunculin A treatment on different surfaces. (C) Representative bright field images and IRM images of *talin A*- cells on different surfaces. (D) The average relative surface contact area of AX3 cells and *talin A*- cells on different surfaces. * indicate significance ($p<0.05$; ANOVA, Tukey test).

4.4.3 Absence of Talin A significantly alters collective cell migration

Cells not only interact with extracellular surfaces but also interact with other cells during collective migration. These two types of interactions compete with each other and regulate the movement of cells (Burute & Thery 2012). In this chapter, I

have discussed how the change of cell-surface adhesions affect migration of individual cells (Figure 4.1C), whereas, how the cell-surface adhesion changes the cell-cell adhesion and collective migration remains largely unknown. Thus, we imaged the early aggregation of *Dictyostelium* on surfaces with different chemical compositions. As mentioned in Chapter 2, *Dictyostelium* relay chemical signals by releasing cAMP at their back and in turn forming multicellular streams in a head-to-tail fashion. The width of such multicellular streams varies from single cell wide to several cells wide, and cells are in contact with both surfaces and neighboring cells in these streams. Thus, the multicellular streams serve as a good model for studying the interplay of cell-cell and cell-surface adhesions.

McCann and et al found that the collective migration patterns dramatically differed between surfaces during the transition from individual cells to multiple aggregates. Multicellular streaming was inhibited on cells that were plated on more adhesive surfaces, such as PLL and FCC, where cells preferred to adhere to each other than on surfaces (McCann et al. 2014). These findings suggest that cells with less cell-surfaces adhesion are likely to form a greater contact area with other cells, which promotes the formation of cell clumps instead of streams and in turn changes the migration pattern.

Therefore, we further studied how the reduction of cell-surface adhesion alters collective migration patterns by imaging the migration of talin A null cells and WT cells (AX2). Similar to AX3 cells (McCann et al. 2014), AX2 cells formed distinct streaming territories on BSA and glass surfaces in 30 minutes and formed a small number of aggregates in 2 hours (Figure 4.5A). However, cells plated on PLL

surfaces formed many aggregates instead of streaming territories, and these small aggregates merged into larger aggregates in 2 hours. The difference in migration pattern suggests that cell streaming and aggregation are affected by chemical compositions of surfaces via cell-surface interactions, and AX2 cells form relatively stronger cell-cell adhesion on PLL surface.

On the other hand, talin A null cells exhibited dramatically different migration behavior compared to AX2 cells. Talin A null cells formed small cell clumps and aggregated by slowly merging small clumps into large clumps. On all three tested surfaces, talin A null cells did not form distinct aggregation territories or large aggregates throughout the image recording time. Moreover, from images talin A null cells appear to form relatively larger cell clumps on PLL surface than on less adhesive surfaces: BSA and glass coated surfaces. One possible explanation is that, with cell-surface adhesion defect, talin A null cells prefer to adhere to each other with greater contact area than adhere to surfaces and aggregating by clumping rather than streaming allows cells to minimize their cell-surface contact area. Such preference is enhanced in cells on PLL surface, where they form even larger clumps.

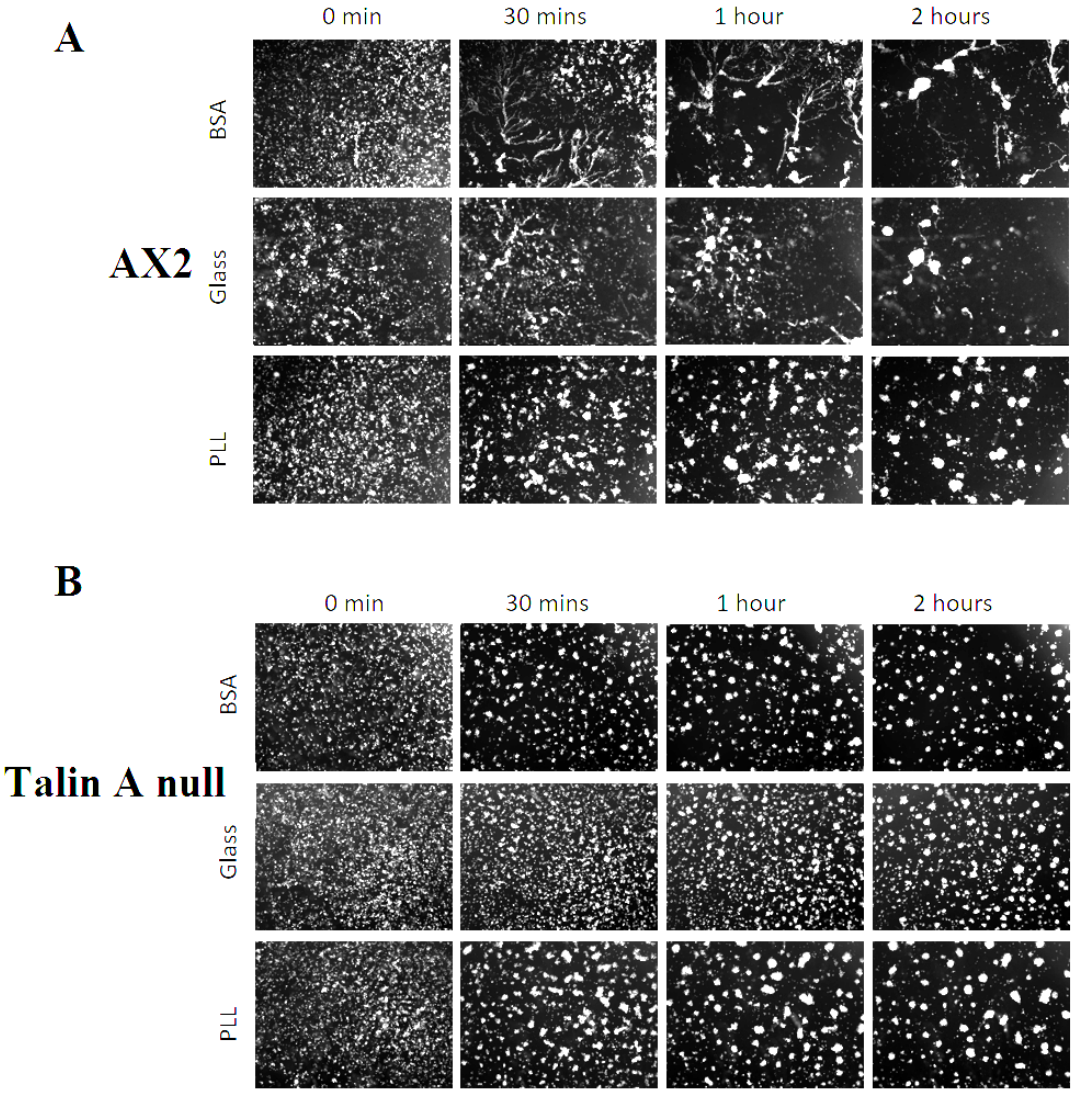

Figure 4.5 – Surface Composition and talin A Affects Collective Cell Migration. (A) Montage of images of AX2 (WT) cells aggregating on the 3 different surfaces, shown at 4 different times. (B) Montage of images of *talin A null* cells aggregate on the 3 different surfaces, shown at 4 different times.

4.5 Discussion

Together, we found *Dictyostelium* cells regulate actin cortex and maintain optimal cell-surface adhesions to adapt to different extracellular substrates, revealing that such adaption does not require integrin-based adhesion. Inhibition of actin filaments with the drug (LatA) leads to distinct cell-surface adhesion on surfaces with different inherent adhesivity, suggesting untreated cells compensate such adhesion difference by actively regulating the actomyosin cortex. The actin-driven protrusion and the myosin II-mediated contraction are crucial for regulating actomyosin cortex. Actin polymerization is found to be significant for all tested surfaces. However, myosin II is found to mainly affect the cell-surface adhesion on highly adhesive surfaces, such as PLL and FCC surfaces, suggesting cell contractility is essential when cells detach from more adhesive surfaces. On the other hand, cells lacking talin A exhibit distinct cell-surface adhesion on less adhesive surfaces, such as BSA and glass surfaces. This is probably due to the fact that actin greatly reinforces cell-surface adhesion on these surfaces, and talin A is the link connecting transmembrane adhesion molecules to actin filaments.

Our finding shows individual cells can regulate cytoskeleton in response to the mechanical difference between surfaces, adhere optimally, and migrate similarly on them. In contrast to the individual migration, collective migration is strongly affected by surface composition or cell-surface adhesion defect as cell streams exhibit distinct contact areas on different surfaces (McCann et al. 2014). Multicellular streaming is greatly inhibited on highly adhesive surfaces, on which cell-surface adhesion is not preferred when competing with cell-cell adhesion. A more in-depth

study on the interplay between cell-surface and cell-cell adhesions will be discussed in the next chapter.

4.6 Materials and Methods

4.6.1 Cell Culture

WT *Dictyostelium* (strain AX3 and AX2) and talin A null cells (*talin A*$^-$) (Kreitmeier et al. 1995) were grown in HL-5 medium with density 4-5x10^6 cells/ml. Cells were developed 4.5 (WT) or 5 (*talin A*$^-$) hours prior the microscopic imaging. The development and harvest procedures have described in detail in Chapter3.5.2. Cells were suspended in phosphate buffer at the end of harvest procedure and then processed according to the assay performed. Experiments requiring Latrunculin A treatment involved resuspending cells in PB with 5 μM Latrunculin A (Invitrogen) for 5 minutes before placing them in a chamber in which the buffer contained 5 μM Latrunculin A. For the Latrunculin A titration experiments, cells were resuspended in PB with different concentration of Latrunculin A (0 (only PB), 5 μM, 1.5 μM, 0.5 μM, 0.25 μM) for 5 min before placing them in a chamber where the buffer contained the same concentration of Latrunculin A.

4.6.2 Surface Preparation

Lab-Tek 8-chamber slides (Lab-Tek, Nunc) were used in experiments in this Chapter. All chambers were pre-washed with 1 M HCl and then triple rinsed with water. To obtain BSA (Sigma) or PLL (Sigma) coated surfaces, chambers were incubated with 1% w/v BSA or PLL solution for 2 hours and then triple rinsed with water. FCC (tridecafluoro-1,1,2,2-tetra hydrooctyl dimethyl chlorosilane; Gelest

SIT8170.0) coated surfaces were obtained by placing chamber slides in a vacuum chamber filled with FCC vapor for 2 hours followed by triple rinsing with water.

4.6.3 Microscopy

Images from interference reflection microscopy (IRM) and images of F-actin staining were taken under a Zeiss Meta 510 microscope with a 40x (NA 1.3) objective, using a HeNe laser (488 nm). IRM samples were prepared by simply plating developed cells on pre-coated surfaces 30 minutes prior the imaging time. F-actin staining samples were prepared with the following protocol. Cells were allowed to migrate for 30 minutes, fixed in 2% formaldehyde and 0.2% glutaradehyde for 10 min, and rinsed twice. Next, 2 μM TRITC-phalloidin in 0.2% Triton was added to each well, and the samples were placed under aluminum foil to incubate for 30 min. Finally, the samples were rinsed 5 times with PBS (Pang et al. 1998).

Self-aggregation assays were performed under a Zeiss Axiovert S100 microscope with a 2.5x (NA 0.075) objective using an automated moveable stage. To facilitate automatic tracking, the height of the condenser was adjusted so that cells appeared bright and background appeared dark in images. Images were acquired every 90 seconds for at least 2 hours.

4.6.4 Image Analysis

The relative contact area was calculated by dividing the cell-surface contact area by the total area of the cell. Cell–surface contact area was measured from IRM images, which were pre-processed with bandpass filtering and thresholding in ImageJ (National Institutes of Health; http://rsbweb.nih.gov/ij/) and imported into a custom Matlab (The Mathworks, Natick, MA) code for measuring the binarized contact area.

The total cell area was measured from bright field images, on which tools of variance filter, thresholding, and binary erosion in ImageJ were applied. The same custom Matlab code was used to calculate the area of each cell based on binarized images.

Chapter 5: The Interplay of Cell-cell and Cell-substrate Adhesion in Collective Cell Migration

This chapter is adapted from Wang, Chowdhury, Driscoll, Parent, Gupta, and Losert (Wang et al. 2014).Text and figures are reproduced here with permission. Chenlu Wang designed and performed the experiments and analyzed the data.

5.1 Overview

Collective cell migration often involves notable cell-cell and cell-substrate adhesions and highly coordinated motion of touching cells. We focus on the interplay between cell-substrate adhesion and cell-cell adhesion. We show that the loss of cell-surface contact does not significantly alter the dynamic pattern of protrusions and retractions of fast migrating amoeboid cells (*Dictyostelium discoideum*), but significantly changes their ability to adhere to other cells. Analysis of the dynamics of cell shapes reveals that cells that are adherent to a surface may coordinate their motion with neighboring cells through protrusion waves that travel across cell-cell contacts. However, while shape waves exist if cells are detached from surfaces, they do not couple cell to cell. In addition, our investigation of actin polymerization indicates that loss of cell-surface adhesion changes actin polymerization at cell-cell contacts. To further investigate cell-cell/cell-substrate interactions, we used optical

micromanipulation to form cell-substrate contact at designed locations. We find that both cell shape dynamics and cytoskeletal activity respond rapidly to the formation of cell-substrate contact.

5.2 Background

Cells collectively migrate to carry out key functions of life: from tissue formation and organ development, to immune response and wound healing. Collective migration may simply involve a large number of cells flocking towards a common attractant, *e.g.* as observed during immune response. Collective migration may additionally involve cohesive migration patterns, in which cells migrate in a coordinated manner. Examples of such collective migration include human mammary epithelial cells, which form cohesive migration sheets during wound healing (Friedl & Gilmour 2009), and posterior lateral line primordial cells, which migrate in cohesive clumps during the development of the mechanosensory lateral line organ in Zebrafish (Matsuda & Chitnis 2010). Both cancer cells and amoeboid cells often migrate as multicellular streams, in which cells move in a head-to-tail fashion using the same path within tissues (Alexander et al. 2008; Kriebel et al. 2003; Weijer 2009).

Collective migration requires the coordination of cells during migration, and therefore the coordination of the cell cytoskeleton and chemical signaling (*e.g.*, chemotactic signaling) that control that migration. The chemical signaling cues that guide collective migration have been extensively studied, and many pathways have been identified. For example, human breast cancer cells have been found to form invading streams *in vivo* that use paracrine and autocrine signaling loops (Dovas et al.

2012; Patsialou et al. 2009). *Dictyostelium discoideum* cells provide a valuable model system for collective migration, since they form head-to-tail multicellular streams during aggregation and are guided by the chemoattractant cyclic adenosine monophosphate (cAMP) (Kriebel et al. 2003; Kimmel & Parent 2003).

In addition to chemical guidance of cell migration, cells are also guided by mechanical cues. Mechanical forces arise from the extracellular matrix (ECM) through cell-surface contact and from other cells through cell-cell contact. These forces regulate the motion of migrating cell groups (Ventre et al. 2012; Kim et al. 2010). Cells are able to follow gradients in stiffness of the extracellular matrix (ECM), a phenomenon known as durotaxis (Roca-Cusachs et al. n.d.). In addition, cells can be guided by external physical forces exerted more locally by other cells or objects (Kim et al. 2010; Weber et al. 2012; Fujita et al. 2009). For example, it has been shown *in vivo* that fiber-like structures in the ECM can provide directional guidance and direct multicellular streams (Alexander et al. 2008; Ventre et al. 2012). We previously showed that cell-surface adhesion can also affect collective migration: *Dictyostelium discoideum* cells exhibit different collective migration patterns on surfaces with different inherent adhesivities (McCann et al. 2014). However, it is not well understood how cell-surface adhesion affects collective migration, or how touching cells achieve highly coordinated motion.

This study focuses on the interplay between cell-cell and cell-substrate contact in migrating cells. Recent studies have shown that in epithelial cells these two adhesion systems spatially inhibit each other and use different mechanisms to regulate the cytoskeleton and to generate mechanical forces (Burute & Thery 2012).

Epithelial cells and many other mammalian cells adhere to each other and to the the substrate via integrins, the activation of which triggers signaling pathways that affect various cell behavior (Critchley 2000). On the other hand, some fast migrating cells, such as *Dictyostelium discoideum*, adhere to surfaces non-specifically, and therefore allow us to study the competition of adhesions in the context of non-integrin mediated adhesion.

We begin our investigation of the competition between cell-cell contact and cell-surface contact by blocking the formation of cell-surface contact. Without cell-surface contact, cells significantly change their collective migration pattern. However, the protrusions and retractions of individual cells are not significantly altered by inhibiting cell-surface contact, which is consistent with our previous observations of cells suspended in water (Driscoll et al. 2012). Next, we investigate how cell-surface coupling affects cell-cell coupling and the spatial distribution of actin polymerization. Further, we use optical tweezers to form controlled cell-substrate contacts, which allows us to systematically study how cell shape dynamics and the cytoskeleton respond to changes in cell-cell and cell-substrate contact.

5.3 Results and Analysis

5.3.1 Without cell-surface contact, *D. discoideum* do not stream in a head-to-tall fashion but instead aggregate by clumping.

We used two complementary approaches of inhibiting cell-surface contact in order to evaluate the effects of cell-substrate adhesion on cell-cell adhesion. In our first approach, wild type cells (AX3) were plated and remained suspended on a polyethylene-glycol (PEG) coated surface (MicroSurface Inc., Missouri). PEG

coatings have previously been used to prevent cells from adhering to surface (Wischerhoff et al. 2008). Interference Reflection Microscopy (IRM) (Barr & Bunnell 2009) was used to determine the actual cell-surface contact area. Bright-field and IRM images of AX3 cells on glass are shown in Figure 5.1A. As we previously reported (McCann et al. 2014), cells partially adhere to glass surfaces. (Regions of adherence appear dark in IRM images. See Figure 5.1A for an example.). On PEG-coated surfaces, cells are less polarized and do not form regions of cell-surface adhesions as shown in Figure 5.1B (no dark region in the IRM image).

With these two surfaces, we examine the migration of *Dictyostelium discoideum* cells. We investigate cells at an early aggregation stage, where cells are prone to signal and to each other and migrate collectively in a head to tail fashion. Cells were marked with the cytosolic stain Cell-Tracker Green (Invitrogen) to facilitate the imaging and analysis of dynamic changes in cell shape. Representative images are shown in Figures 5.1C. On glass, cells are initially uniformly distributed on the surface and move non-directionally. After the first 20 minutes, the cAMP secreted by cells facilitates the formation of multicellular streams. This process is well established as a key example of collective streaming (Kriebel et al. 2003). Collective streaming results in the formation of a few large cell aggregates.

In contrast, cells plated on PEG-coated surfaces do not stream collectively. Instead, they move non-directionally and form small spherical aggregates (Figure 5.1D). After several hours, these spherical aggregates merge into larger aggregates. Since cells remain suspended on PEG coated surfaces, their movement is largely affected by the convection and flows in the chamber. Therefore, cell movement is

actually the combination of passive movement that caused by environment factors and active movement that results from their aggregation motion.

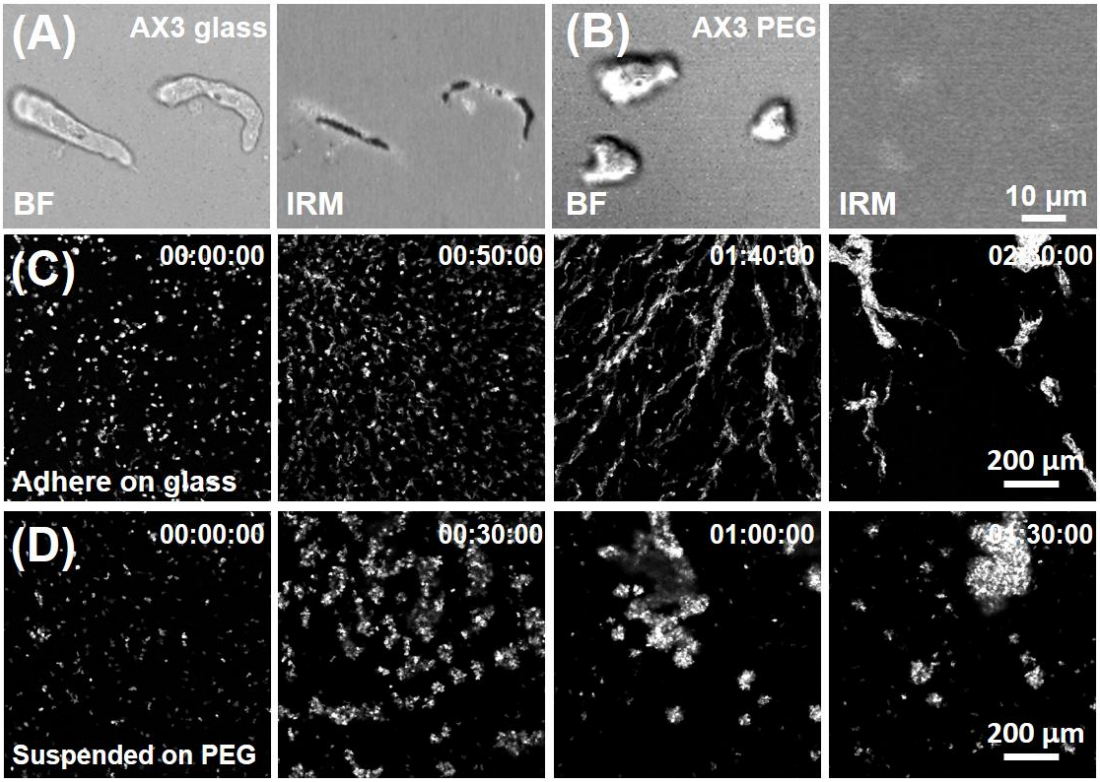

Figure 5.1 –On PEG-coated Surfaces, Cells Exhibit No Cell-Surface Contact and Aggregate by Clumping rather Than Streaming. (A) Bright-field and IRM images of AX3 cells show that cells plated on glass form cell-surface contacts. (Dark areas on the IRM image indicate regions of cell-surface contact.) (B) Bright-field and IRM images of AX3 cells plated on a PEG-coated surface show that cells do not form cell-surface contacts on PEG. (No dark areas are observed on the IRM image.) (C) Early aggregation of AX3 (WT) cells on glass; cells aggregate via multicellular streaming. (D) Early aggregation of AX3 (WT) cells on a PEG coated surface; cells aggregate by clumping instead of streaming.

To distinguish between active movement and passive movement, we used a plugin in ImageJ software (National Institutes of Health; http://rsbweb.nih.gov/ij/)

called template matching to get rid of the passive movement of all cells. Then, a custom particle tracking Matlab (The Mathworks, Natick, MA) code was applied to obtain the movement of each cell or cell clump, from which we calculated the active movement of cells in the field of view. Figure 5.2 shows the comparison of the extracted motion tracks between overall cell movement (original movement) and the active cell movement (corrected movement). After subtracting the passive movement, corrected movement tracks clearly show the aggregation of cells towards an aggregation center.

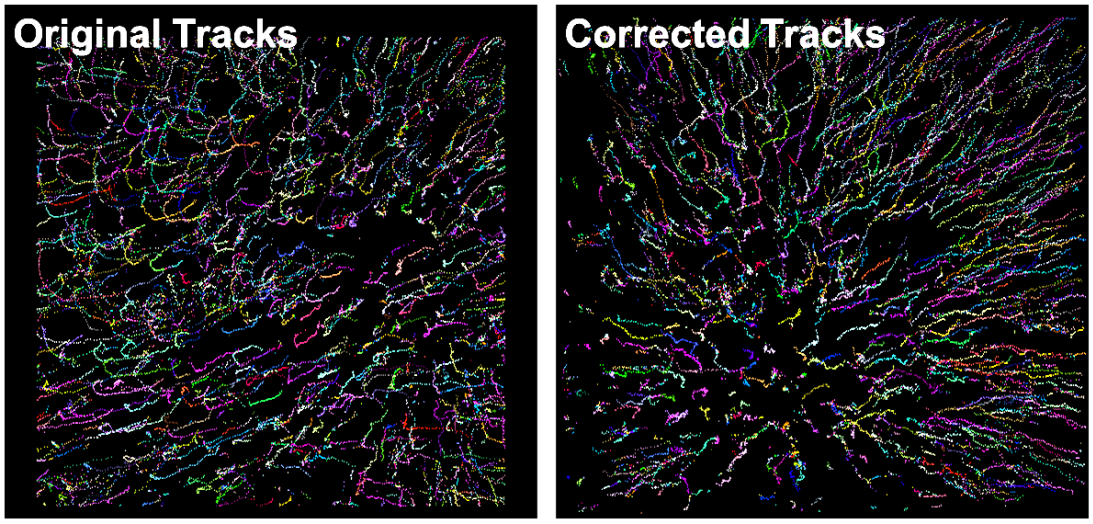

Figure 5.2 – Corrected Motion Tracks. Comparison of the extracted motion tracks between overall cell movement (original movement) and the active cell movement (corrected movement) on PEG coated surfaces.

We found although the overall speed of cells with/without passive motion are similar. (14.9um/min for original motion; 14.6um/min for corrected motion), subtracting the passive flow made the speed more uniform over time (Figure 5.3).

To observe actin polymerization dynamics, we transfected Lifeact-RFP plasmid into wild type Dictyostelium (AX3). Lifeact is a short peptide that fused with

RFP, and it can bind to filamentous actin so that the fluorescent intensity can infer the concentration of polymerized actin. Figures. 5.4A&B are higher magnification images of AX3-Lifeact-RFP cells, which illustrate that cells arrange in streams on glass surfaces and in spherical aggregates on PEG-coated surfaces. During collective streaming on glass, adherent cells align in a head-to-tail fashion in streams. However, suspended cells do not exhibit such alignment inside aggregates. Furthermore, cells that are adhered to a surface show enhancement of F-actin at cell-cell contacts, as shown in Figure 5.4A. In cells that are not adhered to a surface, actin is instead enhanced in the periphery of the aggregate, as shown in Figure 5.4B.

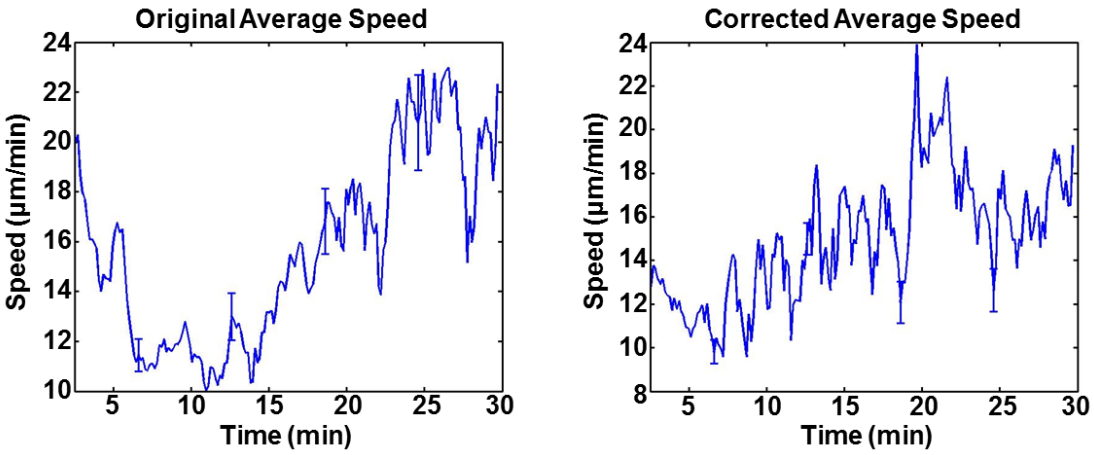

Figure 5.3 – Speed of Cells during Aggregation. Speed of cells with both passive motion and active motion varies during aggregation, whereas the speed of cells with subtraction of passive motion remains steady during aggregation.

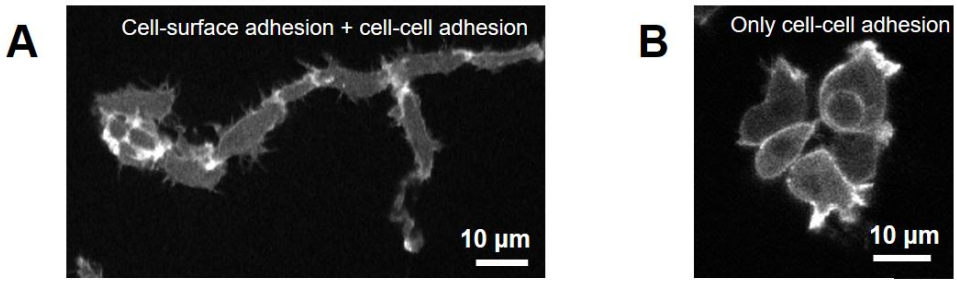

Figure 5.4- Alignment of Cells is Distinct on Different Surfaces. (A) A multicellular stream formed by AX3-Lifeact-RFP cells with cells aligned head-to-tail on glass. (B) A multicellular clump formed by AX3-Lifeact-RFP cells on a PEG coated surface.

5.3.2 Inhibiting cell-cell contact results in significant collective streaming defect.

We examined how cell-cell adhesion affects collective migration in the presence of cell-surface adhesion by utilizing the force of electrostatic repulsion between cells. This approach has previously been used and adapted by us to prevent adhesion between cells and glass coverslips (Socol et al. 2010). Since both cell membranes and glass are negatively charged, they repel one another. Under usual experimental conditions, these negative charges are screened by ions in the phosphate buffer (PB). Repulsion between cells increases as the ion concentration in the medium decreases. In pure water and medium with low ion concentration, this repulsion is strong enough to prevent or partially inhibit cell-cell and cell-surface adhesions. Although this experimental approach only works for our osmotic-shock-resistant amoeboid cells and is not transferrable to mammalian cells, it allows us to tune the mechanical cell-cell contact and elucidate the potential role of cell-cell adhesion in collective migration.

In these experiments, cells were allowed to form cell-surface adhesion in diluted medium (6% PB) for 15 minutes. Then, the medium was adjusted to different concentration (from full medium (100% PB) to almost pure water (1% PB)) to tune cell-cell adhesion at different level. We found that diluted PB (3%~10%) greatly inhibits the formation of cell-cell contact but retains cell-surface contact and cell motility. Cells in the 100% PB form streams normally (Figure 5.5A); cells exhibit significant streaming defect and aggregate through very shorts streams when cell-cell contact partially inhibited (6% PB) (Figure 5.5B); cells in the medium with even lower ion concentration (3% PB) remain their motility but do not form multicellular streams due to the significant inhibition of cell-cell contact (Figure 5.5C); when we further dilute the medium to 1% PB, cell-surface adhesion is also inhibited and some cells detached from the surface (Figure 5.5D). Testing via internal reflection microscopy (IRM) revealed that cells form cell-surface contacts in the first 3 conditions only (Figure 5.6). Therefore, these experiments demonstrate the importance of cell-cell adhesion for collective streaming migration: cells do not align in a head to tail fashion without cell-cell adhesion.

We further study the extreme case in which both cell-cell and cell-surface adhesion are inhibited. Cells were placed in distilled (DI) water instead of ionized buffer (PB), in which condition, the electrostatic repulsion is strong enough to prevent any cell-cell and cell-surface adhesion. Cells suspended in DI water lose both cell-surface adhesion and cell-cell adhesion. However, as shown in Figure 5.5E, these cells retain their polarity and motility (as well as their cytoskeletal activity, data is not shown).

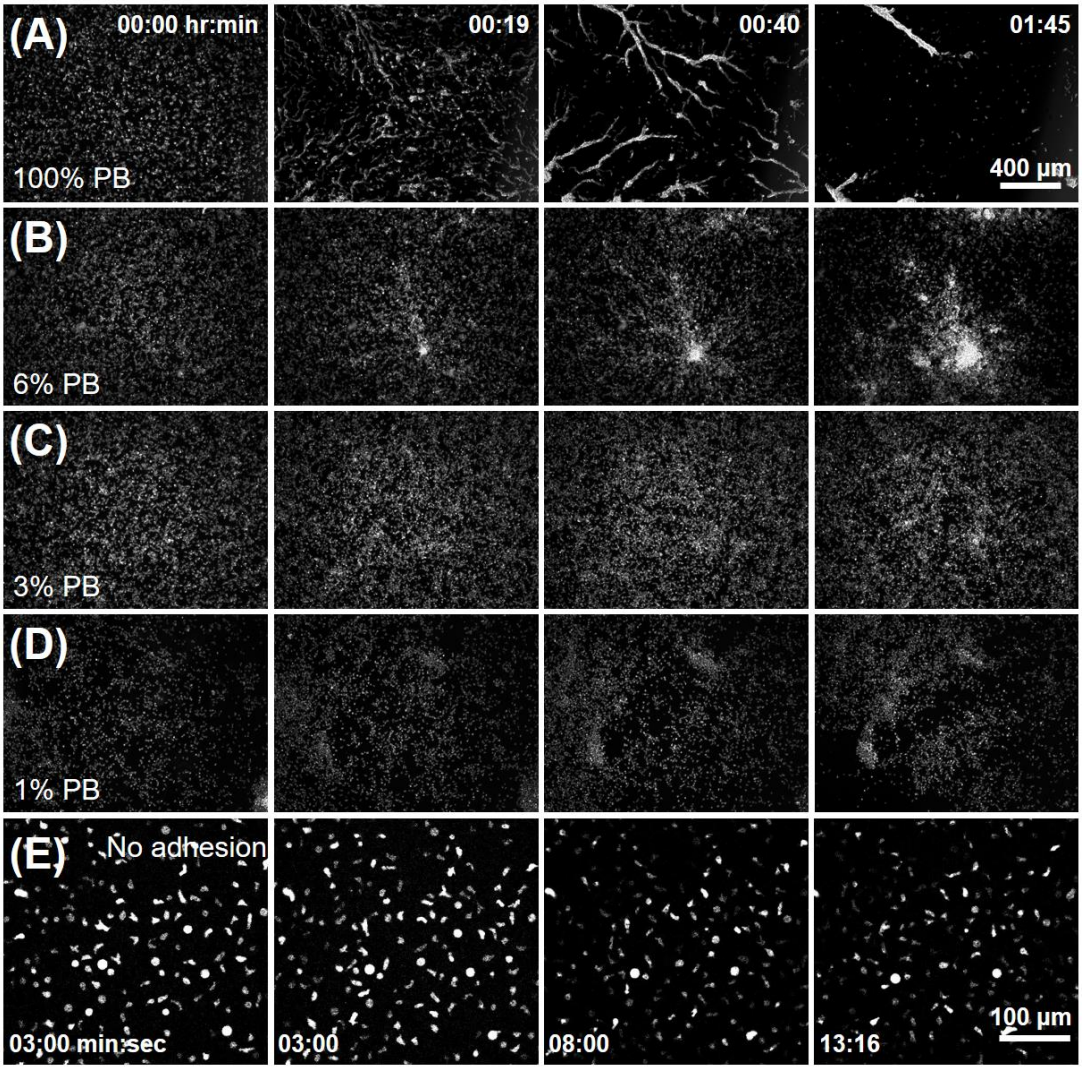

Figure 5.5 –Inhibiting Cell-cell Contact Results in Significant Collective Streaming Defect. (A) Migration of AX3 (WT) cells on glass in 100% PB; cells aggregate via multicellular streaming. (B) Migration of AX3 (WT) cells on glass in 6% PB; cells aggregate with streaming defect due to the partially inhibition of cell-cell contact. (C) Migration of AX3 (WT) cells on glass in 3% PB; cells do not form streams or aggregate. (D) Migration of AX3 (WT) cells on glass in 1% PB; some cells lost cell-surface adhesion. (E) AX3 cells without cell-cell and cell-substrate adhesion exhibit dynamic and polarized morphologies.

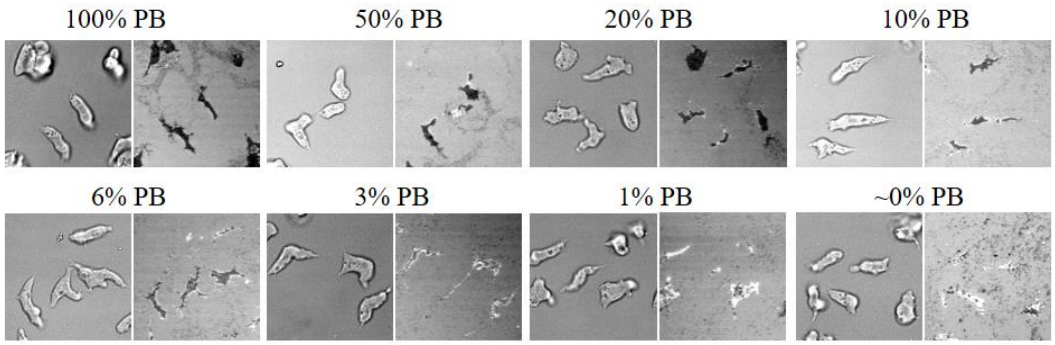

Figure 5.6 –Cell-Surface Contact Area of AX3 Cells in Medium with Different Ion Concentration.

Cells that are suspended on PEG-coated surfaces have cell-cell adhesion but no cell-surface adhesion. Although they retain their shape activities, they cannot form streams since they lose the head-to-tail alignment. On the other hand, cells that are adhered on surfaces display significant multicellular streaming defect when the cell-cell adhesion is inhibited. Therefore, collective streaming requires both cell-cell adhesion and cell-surface adhesion.

5.3.3 The loss of cell-surface contact does not significantly change the shape dynamics and actin activity of individual cells.

Both cell-cell adhesion and cell-surface adhesion are important in collective migration. To understand their respective roles, we first observe cell-surface adhesion in the absence of cell-cell adhesion, *i.e.* how cell-surface adhesion impacts on individual cells. Since cell migration involves a careful interplay of protrusions and retractions, quantitative analysis is used to compare the motion of individual, adherent cells with the motion of individual, suspended cells. Our previously

developed approach represents the shapes and shape dynamics of cells in a way that provides a whole-cell perspective on the protrusive and retractive processes (Driscoll et al. 2012; Driscoll et al. 2011). Briefly, the outline of an individual adherent cell is extracted from a sequence of images. To visualize local protrusions, the curvature at each boundary point is calculated and represented as a different color (see Figure 5.7A.). Red represents convex regions, whereas blue represents concave regions, *i.e.* invaginations. The shape dynamics of this cell can then be represented as a kymograph of the local boundary curvature. A representative case is shown in Figure 5.7B. The shape at each time is represented by a vertical line of equal length that is colored by local curvature. The two horizontal red regions indicate the locations of the front and back (the two polarized ends) of the cell and the slanted red lines indicate protrusion waves traveling on the sides of the cell. We define the polarized end that protrusion waves initiate from as the "front" of the cell and the other end as the "back". Figures 5.7C&D are a representation of the curvature outline and the cell shape dynamics of an individual cell that is suspended on a PEG-coated surface. From Figures 5.7B&D we can infer that both the adherent cell and the suspended cell are polarized, *i.e.*, have a well-defined front and a back, with protrusion waves that travel from the front to the back of the cell. Protrusion waves, which are indicated by black dashed lines, are seen as slanted red lines that initiate at the cell front and propagate to the back. Polarized shapes and similar pattern of protrusion waves are observed on both adherent cells and suspended cells. Further analysis of protrusion waves finds that curvature waves on suspended cells are more frequent than those on adherent cells (Figure 5.8).

To investigate the intracellular processes that allow cells to maintain their polarity and motility, we visualize intracellular actin polymerization using Lifeact-RFP. Actin polymerization is very dynamic at the leading edge of migrating cells. Polymerization bursts are very transient. F-actin dynamics is measured by analyzing the fluorescence intensity of Lifeact-RFP along the cell periphery. In Figures 5.7E&G, the color on the extracted outline represents the F-actin fluorescence intensity near each boundary point. Red represents high fluorescence intensity (high F-actin concentration), whereas blue represents low fluorescence intensity (low F-actin concentration). The kymographs in Figures 5.7F&H show the F-actin activity of representative individual cells that are migrating on a glass surface and are suspended on a PEG-coated surface, respectively. The red areas represent regions of high actin polymerization, which mainly occur at the front of the cell and travel in a wave-like fashion mostly along the sides of the cell that near the front (indicated by black dashed lines). Figures 5.7F&H suggest that both adherent and suspended cells dynamically and asymmetrically assemble actin to generate force on their boundary, so that to maintain their shape polarity and their leading edge, where the membrane is pushed outwards.

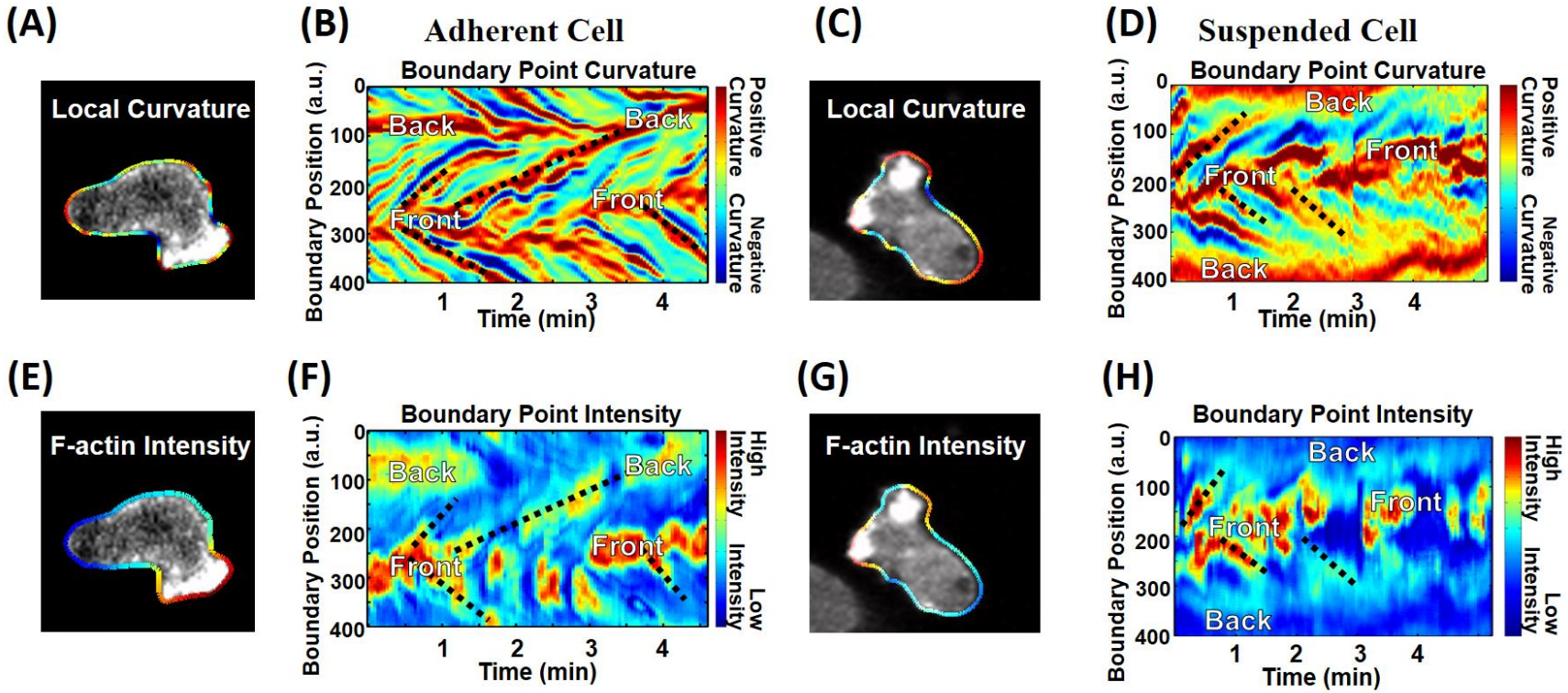
(A)
Local Curvature
(B)
Adherent Cell
Boundary Point Curvature
Boundary Position (a.u.)
Time (min)
Back
Front
Positive Curvature
Negative Curvature
(C)
Local Curvature
(D)
Suspended Cell
Boundary Point Curvature
(E)
F-actin Intensity
(F)
Boundary Point Intensity
High Intensity
Low Intensity
(G)
F-actin Intensity
(H)
Boundary Point Intensity

Figure 5.7 –Cells without Surface Contact Exhibit Similar Shape Dynamics and F-actin Activity as Cells with Surface Contact. (A) An image of a representative adherent AX3-Lifeact-RFP cell with the cell boundary, colored by curvature, overlaid. Here, red represents regions of positive curvature, and blue represents regions of negative curvature. (B) A kymograph of boundary-point-curvature vs. time for an individual, adherent cell. (C) An image of a representative suspended AX3-Lifeact-RFP cell with the cell boundary, colored by curvature, overlaid. (D) A kymograph of boundary-point-curvature vs. time for an individual, suspended cell. These kymographs illustrate that adherent and suspended cells have similar cell shape dynamics. Both of them have two horizontal red region (front & back of the cell) and slanted red lines start from the front red region and end at the back red region (indicated by black dashed lines), which correspond to curvature waves travel on cell boundary from cell front to the back. (E) An image of a representative adherent AX3-Lifeact-RFP cell with the cell boundary, colored by the intensity of nearby actin fluorescence, overlaid. Red represents region of high fluorescence intensity, and blue represents regions of low fluorescence intensity. (F) A kymograph of boundary-point-fluorescence-intensity vs. time for an individual adherent cell. (G) An image of a representative suspended AX3-Lifeact-RFP cell with the cell boundary, colored by the intensity of nearby actin fluorescence, overlaid. (H) A kymograph of boundary-point-fluorescence-intensity vs. time for an individual suspended cell. These kymographs illustrate that adherent and suspended cells show similar patterns of F-actin activity. Regions of high actin polymerization (shown red) mainly occur at the front of cells but sometimes travel in a wave-like fashion along the sides of cells (indicated by black dashed lines).

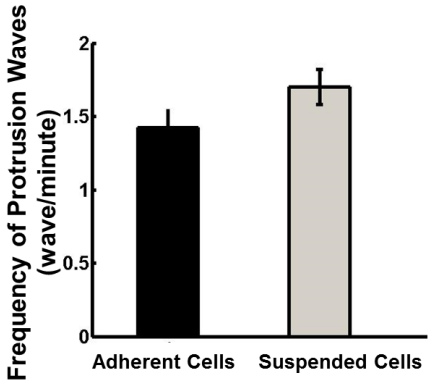

Figure 5.8- Comparison of frequency of protrusion waves that generated on individual adherent cells and individual suspended cells. Data averaged from over 10 cells on each condition. Error bar: standard deviation of the mean.

5.3.4 The shape dynamics of pairs of cells is coupled in a manner that depends on cell-surface contact.

Without cell-surface contact, *Dictyostelium discoideum* cells maintain their cell shape dynamics and cytoskeletal activity when they move as individuals. But, as shown earlier, large groups of cells cannot form normal collective migration patterns without cell-surface adhesion. We hypothesize that the loss of cell-surface contact changes the mechanical interaction between cells, which results in the differences in collective behavior. Thus, pairs of cells in direct contact were studied, as they represent the simplest case of cell-cell interaction.

When two neighboring cells move in in a stream on glass, their cell boundaries are sometimes indistinguishable. To distinguish neighboring cells, a mixture of AX3 cells stained with either Cell-Tracker Green (Invitrogen) or Cell-Tracker Orange (Invitrogen) was used. Figure 5.9A shows a neighboring pair of

differently stained cells migrating on glass. For this analysis, we term the cell that is ahead the ‘leading cell’, and the cell that is behind the ‘trailing cell’. The overall boundaries of pairs of cells were extracted. Figure 5.9B shows overlaid cell shapes from different points in time (6 seconds between shapes). It indicates protrusions travel in the same direction on both cells and cross cell-cell contact region. Protrusions near the cell-cell contact region are pointed out by colored arrows. Further, the shape dynamics of each pair was measured following the approach used for individual cells (see Figure 5.9C). Note that the two red horizontal lines represent the front of the leading cell (cell A) and back of the trailing cell (cell B), and the slanted red lines indicate protrusions traveling on the side of these cells. As observed for individual cells, traveling protrusions initiate at the front of the leading cell. For cell pairs, these protrusion waves travel across the contact region of the two cells (indicated by the purple arrow), and stop when they hit the back of the trailing cell. This suggests that membrane protrusion waves on both cells travel in the same direction and are synchronized in time, *i.e.*, the shape dynamics of these two cells are coupled across the cell-cell contact. For further comparison, we sketch a simplified cartoon of the shape dynamics in Figure 5.9D. Overlapping extracted cell outlines indicate the generation of a membrane protrusion, and the arrows indicate the direction of protrusion propagation.

Pairs of suspended cells exhibit different collective motion and shape dynamics than pairs of adherent cells (Figures 5.9E-G). Overlaid cell shapes (Figure 5.9F) indicate that protrusions travel in opposite directions towards cell-cell contact region on pairs of cells. Coupled, suspended cells do not form cell-cell contact in a

head-to-tail fashion. Instead, they often form tail-to-tail contact, as shown in Figure 5.9G. In this boundary curvature kymograph of a representative pair of cells, the two horizontal red lines represent the front of the two cells and the slanted red lines represent traveling protrusion waves. The cells touch back-to-back, and protrusion waves initiate at the fronts of both cells, travel laterally along the cells, and then stop at the region of cell-cell contact. A schematic of the dynamics of protrusions in suspended cells is shown in Figure 5.9H. In general, pairs of suspended cells generate new protrusions at the end that is farthest away from the region of cell-cell contact. Those protrusions propagate in opposite directions and do not travel across the cell-cell contact. The comparison between pairs of adherent cells and suspended cells suggests that, without cell-surface contact, cells cannot form the head-to-tail cell-cell contact that helps them to synchronize their motion.

To further investigate the response of suspended cells to contact with another object, we use controlled indirect optical-gripping of cells, a technique that we had previously developed and refined (Wang et al. 2013; Sagar Chowdhury et al. 2013; Thakur et al. 2014; S Chowdhury et al. 2013). In our sample applications, we demonstrated that assistant tools, such as glass beads, could be used to indirectly bring two cells in controlled contact, without directly exposing cells to the potential photo-damage from the laser. Surprisingly, we had found that two suspended cells that are brought into front-to-back contact do not retain that alignment but instead rapidly change the location of their leading edges (Wang et al. 2013). One possible reason is that the loss of cell-surface adhesion varies the adhesivity of the cell membrane, *e.g.*, the leading edge or tail of cells become less sticky and so cells are

more likely to adhere at other positions. To analyze the role of cell-substrate contact in a controlled way, we move glass beads (5 μm in diameter, Bangs Laboratories, Fishers, Indiana) towards target cells using optical tweezers (Figure 5.9I). Once the cell-bead distance is small enough to form direct cell-bead contact, we release the bead from the laser trap. Therefore, there is no optical tweezer force that pushes or pulls the cell after the formation of cell-bead contact. When a glass bead is adhered to the leading edge of a suspended cell, the cell rapidly loses its polarity and generates a new leading edge far from the cell-bead contact region, consistent with our observations of suspended cell behavior in response to cell-cell contacts. Our observations suggest that cells actively alter their shape dynamics and leading edge locations when forming direct contact with other objects, such as beads or cells.

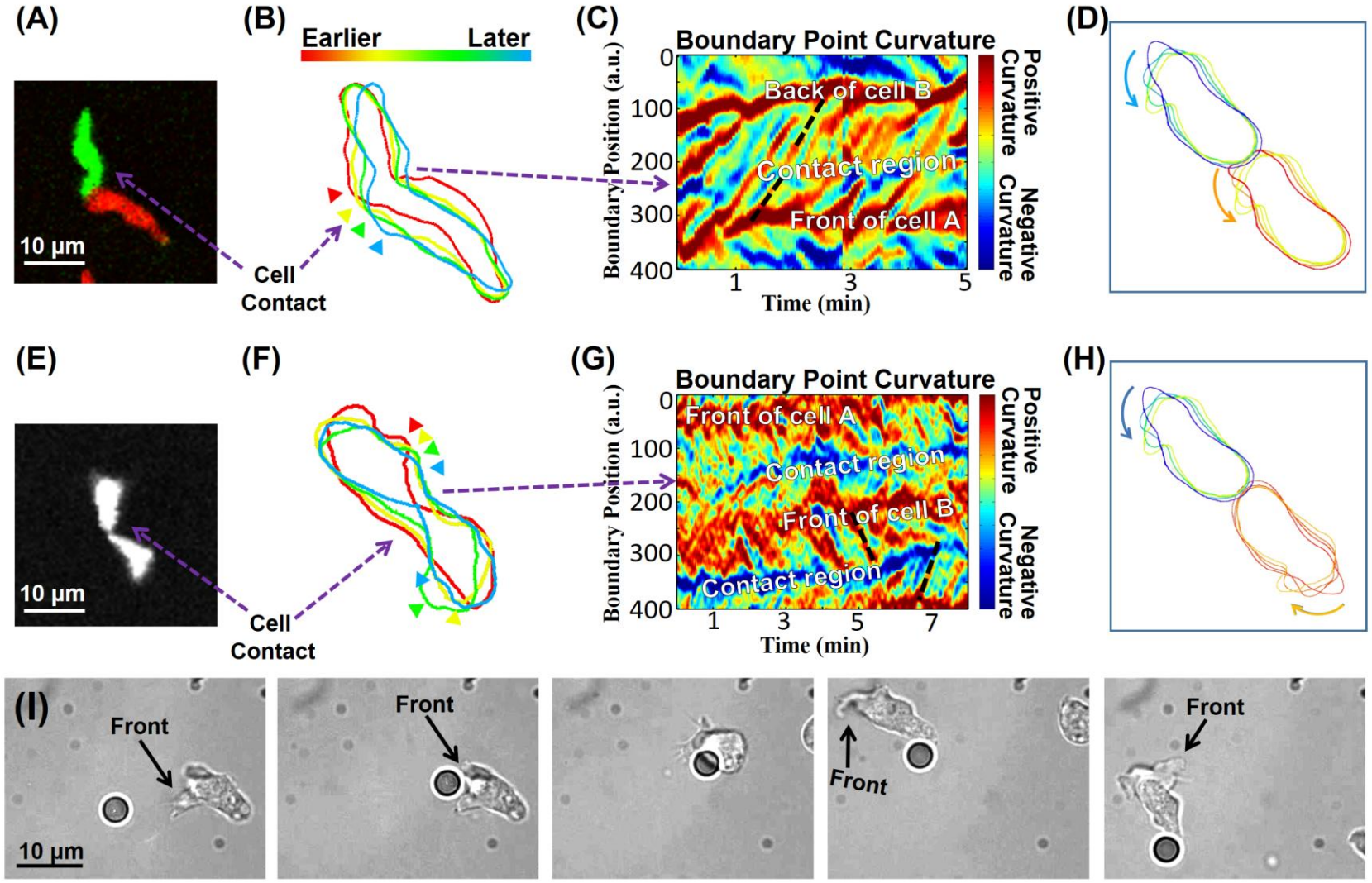
(A)
10 μm
Cell
Contact
(B)
Earlier
Later
(C)
Boundary Point Curvature
Back of cell B
Contact region
Front of cell A
Boundary Position (a.u.)
Time (min)
Positive Curvature
Negative Curvature
(D)
(E)
10 μm
Cell
Contact
(F)
(G)
Boundary Point Curvature
Front of cell A
Contact region
Front of cell B
Contact region
Boundary Position (a.u.)
Time (min)
Positive Curvature
Negative Curvature
(H)
(I)
Front
10 μm
Front
Front
Front

Figure 5.9 - Adherent cells exhibit coupled protrusion waves but suspended cells do not. (A) An image of a representative pair of AX3 cells that are head-to-tail aligned and migrating on glass. (Cells were cytosolically stained green and orange.) (B) Overlay of the shapes of this pair of cells, which shows that the protrusion waves in both cells travel in the same direction and cross the cell-cell contact region. Red outline is a cell shape extracted from an earlier frame, whereas blue outline is a cell shape extracted from a later frame. Protrusions are pointed out by arrows. (C) A kymograph of boundary-point-curvature vs. time for this pair of adherent cells. Cell boundaries were extracted from the overall boundary of the two cells. The kymograph shows that curvature waves, indicated by black dashed lines, travel along the same direction in these two cells. (D) A cartoon of the shape dynamics of a pair of adherent cells. Protrusion waves in different cells propagate in the same direction and travel from cell to cell. (E) An image of a representative pair of AX3 cells suspended over a PEG-coated surface. (Cells were cytosolically stained.) (F) Overlay of the shapes of this pair of suspended cells, which shows that protrusion waves travel in opposite directions along the two cells. (Protrusions are pointed out by arrows on both cells, from red to blue.) (G) A kymograph of boundary-point-curvature vs. time for this pair of suspended cells. Cell boundaries are extracted from the overall boundary of the two cells. The kymograph shows that the curvature waves (indicated by black dashed lines) travel in opposite directions along these two cells. (H) A cartoon of the shape dynamics of a pair of suspended cells, Protrusion waves in different cells propagate in opposite directions and do not travel from cell to cell. (I) Cell-substrate contact can induce a switch in cell polarity. Upon contact with a bead at its front, this cell rounds up, and then forms a new front away from the bead.

5.3.5 The spatial patterning of actin polymerization in directly contacted cells varies with cell-substrate contact.

We investigate how actin polymerization responds to changes in cell-cell contact, and how this response differs for adherent and non-adherent cells. The F-actin concentration of a representative pair of cells migrating with front-to-back alignment on glass is shown in Figure 5.11A. Actin mainly polymerizes at the front of the leading cell and at the contact region of the two cells. The fluorescence in the contact region is mostly due to the enrichment of F-actin at the leading edge of the trailing cell, as shown in Figure 5.10. The kymograph of the fluorescence intensity near the boundary of this pair of cells indicates that this enrichment near the leading edge and at cell-cell contacts persists during migration (Figure 5.11B). Statistical analysis of the relative fluorescence intensity on the cell boundaries (Figure 5.11C) supports the observation that the cell-cell contact region exhibits significantly higher F-actin activity than the far edges (free ends) of either cell. (The colored rectangular boxes in Figure 5.11A indicate the regions that are analyzed in Figure 5.11C. The rectangular boxes in Figures 5.11D, F, G, I, J also indicate regions of analysis.)

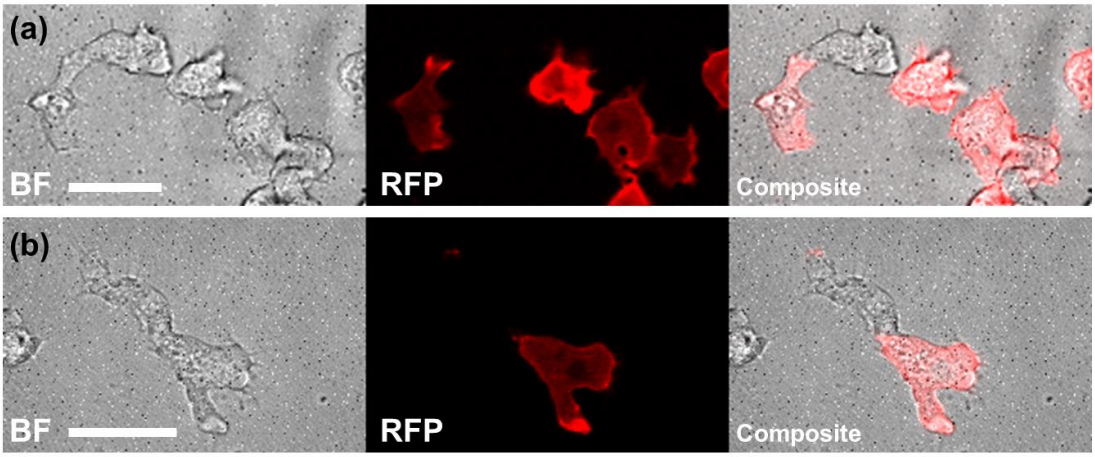

Figure 5.10 - Cells Migrate on Glass Surface Mainly Polymerize Actin at Their Leading Edges. AX3 (WT) cells and AX3-Lifeact-RFP cells were evenly mixed and plated on glass surface. (A), Bright field, fluorescent, and composite images show a AX3 (WT) cell is migrating on glass surface, followed by an AX3-Lifeact-RFP cell, which has more F-actin at its front. (B), Bright field, fluorescent, and composite images show an AX3-Lifeact-RFP cell is leading an AX3 (WT) cell during migration. There is no notable F-actin enrichment at the back of the AX3-Lifeact-RFP cell.

Similarly, the F-actin concentration in pairs of suspended cells that display back-to-back alignment was investigated. In these cells, actin mostly polymerizes at the far edges (free ends) of both cells, with no significant F-actin enrichment in the cell-cell contact region. Kymographs of F-actin intensity (Figure 5.11E) and statistical analysis of relative fluorescence intensity (Figure 5.11F) further validate this observation.

Our results suggest that, without cell-surface adhesion, cells organize their cytoskeleton differently when they adhere to other cells. From analysis of shape dynamics and F-actin activity, we find that in both adherent and suspended cells, actin polymerizes at the cell fronts, where protrusion waves are initiated. However, in pairs of suspended and adherent cells, the cell fronts occur in different locations. Adherent cells locate their fronts at the tails of other cells, whereas suspended cells locate their fronts away from other cells.

Using optical micromanipulation as describe earlier in the paper, we next investigate how the introduction of controlled cell-surface contacts drives reorganization of the intracellular cytoskeleton. To simultaneously optically

manipulate beads and measure actin fluorescence, we built a florescence light path into our optical tweezers system. This allowed us to image the spatial distribution of F-actin within cells before and after beads were adhered onto cells via optical micromanipulation. The typical process of such manipulation is shown in Figures 5.11G-I. We find that upon contact with a silica bead, F-actin is enriched away from the region of cell-bead contact. This is consistent with and provides a molecular explanation for our observation that protrusions occur away from regions of cell-bead contact. Further analysis of the F-actin intensity along a cell boundary is shown in Figure 5.11J. This analysis further validates that cells form a leading edge away from cell-surface contact and that F-actin is enriched at that leading edge. Intracellular actin polymerization actively responds to the adhesion of either a silica bead or another cell in a similar manner.

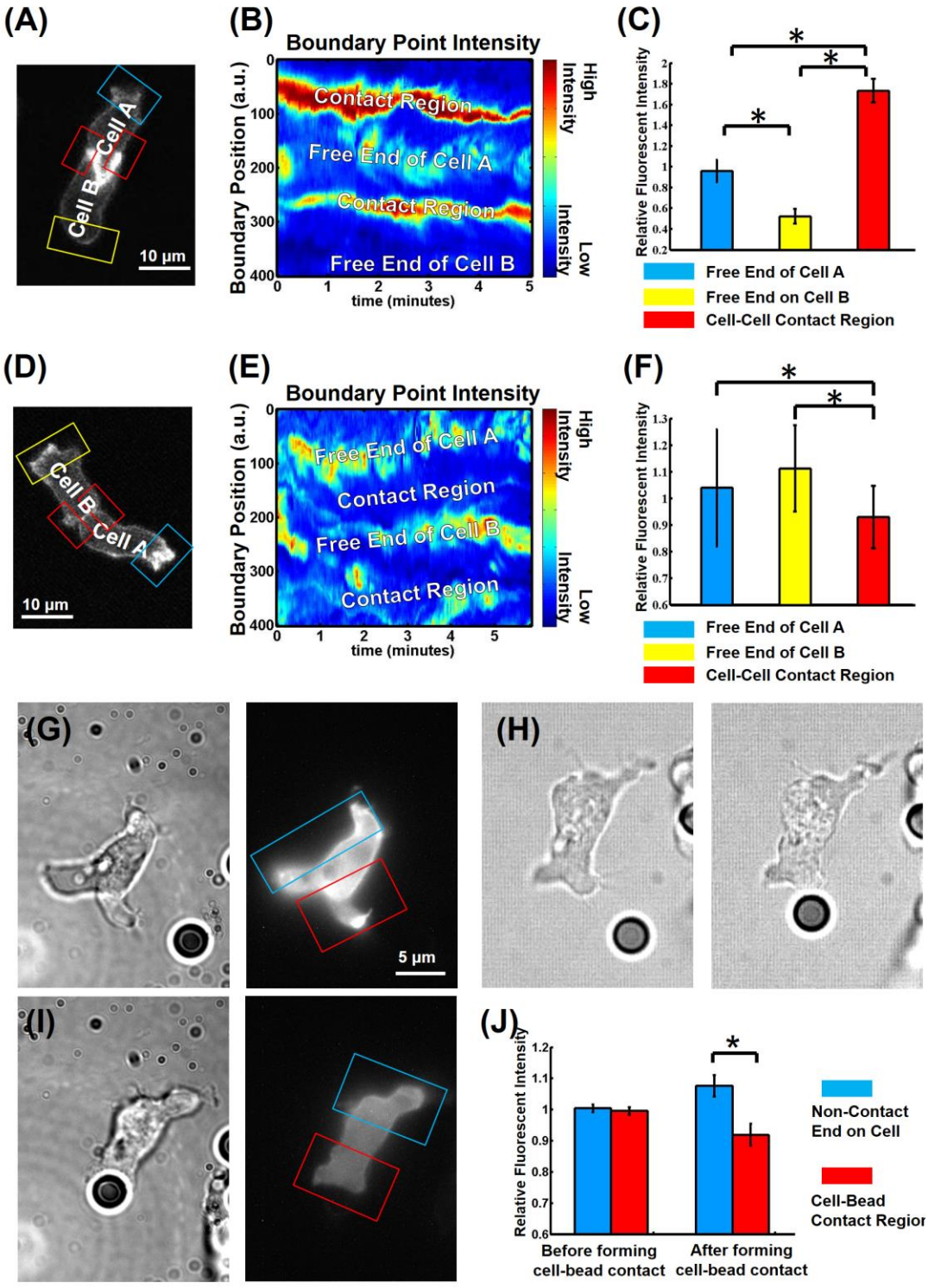

Figure 5.11 - The Spatial Distribution of F-actin in Pairs of Cells Responds to a New Cell-surface Contact. (A) A fluorescence image of two AX3-Lifeact-RFP cells in direct

contact on glass. Colored, rectangular boxes indicate the regions that are analyzed in (C). (B) A kymograph of boundary-point-fluorescence-intensity vs. time for this pair of adherent cells. F-actin is persistently enriched at cell-cell contacts. (C) Relative F-actin fluorescence intensity in different regions on the boundary for the pair of adherent cells. The cell-cell contact region (shown red) shows higher fluorescence intensity than the free ends of the cells (shown blue and yellow). (D) A fluorescence image of two AX3-Lifeact-RFP cells in direct contact suspended on a PEG-coated surface. Colored rectangular boxes indicate the regions that are analyzed in (F). (E) A kymograph of boundary-point-fluorescence-intensity vs. time for this pair of suspended cells. No enrichment of F-actin is found at the cell-cell contact. (F) Relative F-actin fluorescence intensity in different regions on the boundary for the pair of suspended cells. The cell-cell contact region (shown red) shows lower fluorescence intensity than the free ends of the cells (shown blue and yellow). (G) Bright-field and fluorescence images of a suspended AX3-Lifeact-RFP cell with a 5 μm silica bead nearby. (H) Using optical tweezers, the silica bead is adhered to a recently generated protrusion on the cell, and sticks on the membrane of the cell. (I) Bright-field and fluorescence images of the cell after manipulation show that, following contact with the bead, F-actin is enriched at the end of the cell opposite to the cell-bead contact region. (J) Relative F-actin fluorescence intensity in different regions on the boundary of a cell before and after the formation of cell-bead contact. (In C, F, J, to make intensity of each frame comparable, the average intensity of the whole cell boundary in each frame was normalized to be 1. Each analyzed region includes the same number of boundary points. Error bar: standard deviation. *: T-test $P<0.001$).

5.4 Discussion

Our main result is that the presence of cell-surface contacts affects actin polymerization at cell-cell contacts, and that cell-surface contacts are important to facilitate head-to-tail collective migration. Even though the shape dynamics and internal actin polymerization dynamics of individual cells during amoeboid migration do not appear to depend on surface adhesion, we find that the loss of surface adhesion significantly alters the collective migration pattern. Our analysis suggests that this change in collective behavior is not simply due to the fact that cells are not able to move well without surface adhesion (though they are able to "swim" as reported by us and others in prior work (Driscoll et al. 2012; Barry & Bretscher 2010; Bae & Bodenschatz 2010)), but due to changes in the shape dynamics.

The motor underlying this shape dynamics is studied through observing actin polymerization activity. Our results indicate that individual suspended cells display similar F-actin activity as adherent cells, but that actin polymerization in touching cells is only coordinated to facilitate motion in the same direction if a cell-surface contact is present. The loss of cell-surface contacts leads to a loss of the cell-cell mechanical coupling via protrusion waves and actin polymerization enrichment. To generate a controlled cell-substrate contact, and to image intracellular actin polymerization at the same time we adapted our optical micromanipulation system. We find that after forming controlled cell-substrate contacts cells respond to the additional contact points with enhanced actin polymerization.

These observations from the optical manipulation experiments give us complementary insights into mechanotransduction in two aspects: (i), as previously

shown, motility or shape change can be stimulated by forming contact with objects that are coated with certain chemical components (*e.g.* cadherin, antibody, or other protein/protein complexes) (Weber et al. 2012; Guilluy et al. 2014; Wang et al. 2005). The mechano-chemical effects reported in these studies are specifically mediated by the chemical components that are coated on the objects. Whereas, since we used uncoated silica beads and *Dictyostelium discoideum* cells adhere to substrate non-specificly, *i.e.*, no integrin mediated adhesions, the changes in cell shapes dynamics and the reaction of actin activity we report in our study are not chemical component specific. (ii), forces in the range of hundreds of pN to hundreds of nN exerting on cellular structures appear needed to activate mechano-chemical signaling pathways, known as mechanotransduction pathways (Weber et al. 2012; Wang et al. 2005; Sniadecki 2010; Maruthamuthu et al. 2011). However, in our experiments, we observed changes of cell actin dynamics without the need to apply any external forces on cells, *i.e.*, forming cell-surface contact can induce a change in intracellular dynamics. It would be interesting to test whether applying forces can induce different intracellular responds on this system. Such experiments require the use of different force spectroscopy that can exert higher forces than optical tweezer (*e.g.*, magnetic tweezer or AFM), which can exert up to 10nN forces (Sniadecki 2010; Neuman & Nagy 2008).

Collective aggregation is an important behavior of cell groups. Studies of collective migration generally focus on chemical signaling between cells, and the migration of cells in response to that signal. Our results indicate that, in addition, cell-surface coupling can facilitate collective migration via coupling of actin

polymerization activity. On the other hand, when cells are not in contact with a surface, they are no longer able to migrate in a cooperative manner. Indeed we observe less polymerization activity at cell-cell contacts but instead protrusions and actin polymerization at the boundaries of the aggregate. Though this is a very distinct localization of mechanical activity, it also leads to aggregation of cells into larger groups, very similar to collective migration on an adhesive surface. Our findings suggest that aggregating cells do not simply utilize actin polymerization to develop protrusions in response to chemotactic signals. Our data suggest that actin polymerization dynamics is also coordinated by cell-cell adhesion and cell-surface adhesion in a way that facilitates collective behavior. The migratory machinery of the cell thus appears to weigh and balance of mechanical stimuli with chemotactic signals in yet unexplained ways to facilitate robust aggregation.

5.5 Materials and Methods

5.5.1 Model system

To study the interplay between mechanical and biochemical signaling, we use a simple model system, the social amoebae *Dictyostelium discoideum*, which form multicellular streams during development (Kriebel et al. 2003). They do so by simultaneously chemotaxing towards and secreting adenosine 3',5'-cyclic monophosphate (cAMP), thereby forming aggregates which eventually differentiate into fruiting bodies. When exposed to a gradient of cAMP, the cells quickly orient themselves up the gradient and migrate using F-actin based pseudopodial extensions of their front, coupled with myosin II-mediated contraction and retraction of their

sides and back. Cyclic AMP not only induces cells to migrate directionally, but also stimulates the cells to produce and release cAMP locally, which allows cells to relay the chemoattractant signal to distal cells and migrate collectively in a characteristic head-to-tail fashion.

5.5.2 Tissue culture, differentiation and labeling

Wild-type *Dictyostelium discoideum* (AX3) cells and the mutant AX3-Lifeact-RFP cells were grown in HL-5 medium at 21 ℃ to concentrations no higher than $5*10^6$ cells/mL (Sussman 1987). For experiments, cells were starved and developed for 5 hours in development buffer (DB: 5 mM KH_2PO_4; 5 mM $Na_2HPO_4*7H_2O$; 2 mM $MgSO_4$; 0.2 mM $CaCl_2$) and pulsed with 75 nM cAMP every 6 mins, as described in other papers (Devreotes et al. 1987; McCann et al. 2010). Developed cells were harvested after 5 hours by centrifugation of 500μL of the development liquid at 9000 rpm for 3 minutes. The cell pellets were washed twice and dissolved in 500μL of phosphate buffer (PB: 5 mM KH_2PO_4; 5 mM $Na_2HPO_4*7H_2O$) or distilled water. In some experiments, cells were fluorescently stained with CellTracker Green CDMFA or CellTracker Orange CMTMR (Invitrogen) at concentrations of 18 μg/mL for 20 minutes, similarly to previously reported procedures (McCann et al. 2010).

5.5.3 Microscopy

The early aggregation of AX3-Lifeact-RFP cells was imaged for 2.5 hours every 6 seconds using a Leica SP2 confocal microscope with a 10X objective. $4*10^5$ cells were well mixed in 300 μl of phosphate buffer and added into a 2-well Lab-tek chamber 15 minutes prior to imaging to allow cells to adhere to the surface. The early aggregation assay experiments were repeated 3-5 time for each experimental

condition. Zoomed in confocal images of AX3-Lifeact-RFP Cells were taken every 2.5 or 2 seconds using either a Zeiss 510 confocal microscope with a 40X objective or a Leica SP2 confocal microscope with a 100X objective.

Optical manipulation images were taken using a Nikon inverted light microscope with a 60X objective, which is integrated with a Biorryx optical trapping system (Arryx Inc., Chicago, Illinois). Optical traps were generated with a 532 nm laser (Nd:YAG 5W, Spectra-Physics, Newport Inc., Irvine, California). A fluorescence system was also incorporated into the same microscope to facilitate fluorescence imaging (Ex: 540nm-580nm, Em: 620 nm-700 nm). Images were collected by a highly sensitive CCD camera (PCO. Edge, Kelheim, Germany).

5.5.4 Image analysis

Confocal images were processed by a custom shape analysis Matlab (The Mathworks, Natick, MA) program as described in previous publications (Driscoll et al. 2012; Driscoll et al. 2014). Shapes of individual cells or pairs of cells were extracted and 400 points on the boundary were obtained on each frame. All boundary points can be tracked by applying 1:1 mapping between points on each frame and the following frame. The mapping is based on the finding of the minimum sum of square distance between points. For each boundary point, the curvature was calculated by fitting a circle into this boundary point and two points that 10 points away from it. For visualization, the value of the curvature is scaled in color in the kymograph with a cut off at a maximum curvature magnitude (0.25). The color bars are normalized by the cut off (-2.5 to 2.5). For the fluorescent intensity measurement, we draw a circle (10 pixels in diameter) around each boundary point and calculate the average actin

intensity within that circle. Then, the value of the intensity of each points was normalized by the maximum intensity on the cell boundary and scaled in color in the kymograph.

The shape analysis and fluorescent intensity analysis for individual adherent and suspended cells were repeated on 20-30 cells. Typical examples were shown in Figure 5.7. Similar analysis for pairs of adherent and suspended cells were repeated on 5-10 pairs of cells. Typical examples were shown in Figure 5.9 and 5.11.

Chapter 6: Suppression of Actin Waves Enables Collective Cell Migration

This chapter is adapted from a manuscript under preparation by Wang, Parent, and Losert (Wang et al. in preparation). Chenlu Wang designed and performed the experiments and analyzed the data.

6.1 Overview

Cells are able to migrate in a coordinated manner in groups. The mechanism that regulates the cytoskeleton in response to the contact with neighboring cells remains largely unknown. To understand cell-cell coordination, we investigated the cell shape dynamics and the actin polymerization in multicellular streams. We found that protrusion waves traveling along cell boundaries connect from cell to cell. In contrast, actin polymerization waves are suppressed on streaming cells, and F-actin is exclusively distributed at the front of cells where cell-cell contacts are formed. By applying Principal Component Analysis (PCA) to the cell shape change and the actin activity, we found that, compared to individually migrating cells, collectively migrating cells exhibit more localized protrusions at their fronts, which we termed front narrowing. The coupling of protrusion waves and the front narrowing are associated with the restricted actin polymerization. Reducing actin polymerization

with Latrunculin A leads to the re-organization of actin cortex, the decrease of front narrowing, and the decoupling of protrusion waves. Our findings suggest that the cell-cell coupling depends on the exclusive actin polymerization and the corresponding front narrowing behavior at cell-cell contacts.

6.2 Background

Cell migration is a ubiquitous phenomenon in developmental biology, immune response, wound healing and cancer metastasis (Lammermann et al. 2013; Matsuda & Chitnis 2010; Friedl & Gilmour 2009). Migrating cells exhibit distinct morphology, motility, and migration patterns depending cell type, cues from the cellular micro-environment, and signals from other cells (Weijer 2009; DuFort et al. 2011; Parent 2004; Doyle et al. 2013). Some cells migrate individually, such as immune and leukemia cells. Other cell types migrate in multicellular groups as observed during development and wound healing. Group migration is a highly orchestrated process that requires the integration of multiple external signals and the transmission of the information to neighboring cells in order to coordinate motion and steer the migration of the group (Haeger et al. 2015; Menko et al. 2014; Mayor & Etienne-Manneville 2016).

During migration, eukaryotic cells actively deform their shape by extending pseudopods and contracting their plasma membrane (Lauffenburger & Horwitz 1996). The generation of actin-rich protrusions is regulated by external chemical cues and steers cells during chemotaxis (Van Haastert & Bosgraaf 2009; Rickert et al. 2000). In addition, cell-substrate binding provides anchor points that are essential for cell translocation (Lämmermann & Sixt 2009; Lauffenburger & Horwitz 1996; Parsons et

al. 2010). Therefore, the location and dynamics of protrusions largely determine the membrane motion and ultimately the direction of migration. Distinct protrusion activities have been observed in a variety of cells: some protrusions grow and retract locally on cell membrane, while others are more dynamically propagated along the cell membrane in a wave-like fashion, exhibiting rich diversity in size and speed (Machacek 2006; Driscoll et al. 2012; Van Haastert & Bosgraaf 2009).

Active cellular shape changes are internally driven by the rearrangement of the actin cytoskeleton - a complex network formed by dynamically polymerizing and depolymerizing actin filaments. Indeed, the growth of actin filaments has been shown to exert sufficient force to push the cell membrane outward and generate membrane protrusions (Prass et al. 2006). Self-assembled actin polymerization waves traveling along the cell cortex have been measured in various cell types (Gerisch et al. 2004; Weiner et al. 2007; Rottner & Stradal 2011; Allard & Mogilner 2013). Moreover, it has been shown that the propagation of actin waves associates with membrane motion waves in migrating cells (Driscoll et al. 2015; Enculescu et al. 2010; Machacek 2006; Weiner et al. 2007). Similarly, signaling proteins that regulate actin polymerization, such as PIP_3, also exhibit wave-like activities during cell migration (Gerisch et al. 2012; Rickert et al. 2000).

It was recently established that membrane protrusion waves couple between collectively migrating cells, such as in epithelial cells in a monolayer sheet or in directly associated pairs of amoeboid cells (Zaritsky et al. 2014; Wang et al. 2014; Zouani et al. 2014). However, the underlying mechanism regulating the coupling of membrane waves remains largely unknown. One intuitive hypothesis is that the

coupling of membrane protrusive waves between neighboring cells is mediated by traveling actin waves. Indeed, recent studies have shown that molecules that maintain cell-cell contacts often directly or indirectly connect with the intracellular cytoskeleton, which allows cells to rearrange their cytoskeleton in response to signals from neighboring cells and coordinate their group cell behaviors (Weber et al. 2012; Wu et al. 2014; Cai et al. 2014).

We, therefore, sought to determine if migrating groups of cells couple their internal actin waves. We used the social amoebae *Dictyostelium discoideum* as a model system for our studies. Upon starvation, these cells enter a developmental program that leads to the formation of an aggregate that differentiates into a multicellular organism that can resist harsh environmental conditions. Aggregate formation is a highly organized process that occurs as cells chemotax towards self-generated adenosine 3',5' cyclic monophosphate (cAMP) cues. As the cells migrate and relay cAMP signals to neighboring cells, they migrate in a head-to-tail fashion and form characteristic streams (Kriebel et al. 2003; Kimmel & Parent 2003). We previously showed that *Dictyostelium* cells extend leading edge membrane protrusions and propagate wave-like protrusions across head-to-tail contacts on pairs of cells, which are essential for streaming (Wang et al. 2014).

In this report, we compared cell shape change and actin assembly in individual and streaming cells. Remarkably, while we found that membrane protrusion waves were coupled between streaming cells, waves of actin polymerization were significantly suppressed. In aligned cells, actin polymerization exclusively occurred in cell-cell contact regions instead of propagating along the cell

boundaries of individual cells. This restricted distribution of F-actin at cell-cell junctions led to a change in cell shapes and collective migration patterns. Our findings reveal that collectively migrating cells exhibit localized actin assembly, which helps them adapt their motion to migrate coordinately within groups.

6.3 Results and Analysis

6.3.1 Cells couple their motion in multicellular streams and suppress actin waves

We used the under-agarose migration assay (Figure 6.1A) to observe cell shape change in a 2D environment, as well as to create a stable cAMP concentration gradient, which guides cells to form streams (Materials & Method) (Nelson et al. 1975; Kriebel & Parent 2009). To follow the behavior of individual cells inside of streams, we mixed 70% of wild type (WT) AX3 cells with 30% of WT cells expressing lifeact-RFP, which labels F-actin (Riedl et al. 2008), and recorded time lapse fluorescent images of chemotaxing cells (Figure 6.1B, Figure 6.1C, left). By applying a custom shape analysis Matlab code (Mathworks, Natick, MA, USA) as previously reported (Driscoll et al. 2012) (Materials & Method), we tracked the movement of the geometry center of cells. Figure 6.1C shows a typical example of cell (green) accurately following the trajectories of an earlier cell (red) in the stream. During the migration of the green cell, we measured the minimum distance of it to the trajectory of the red cell. The trajectories of cells migrating in the same streams largely overlap, as the distance between trajectories remains below 2 μm (Figure 6.1D), which is very small compare to the width of cell streams (3~5μm). We hypothesize that streaming cells so accurately coordinate their migration by exquisitely coordinating the movement of their shapes.

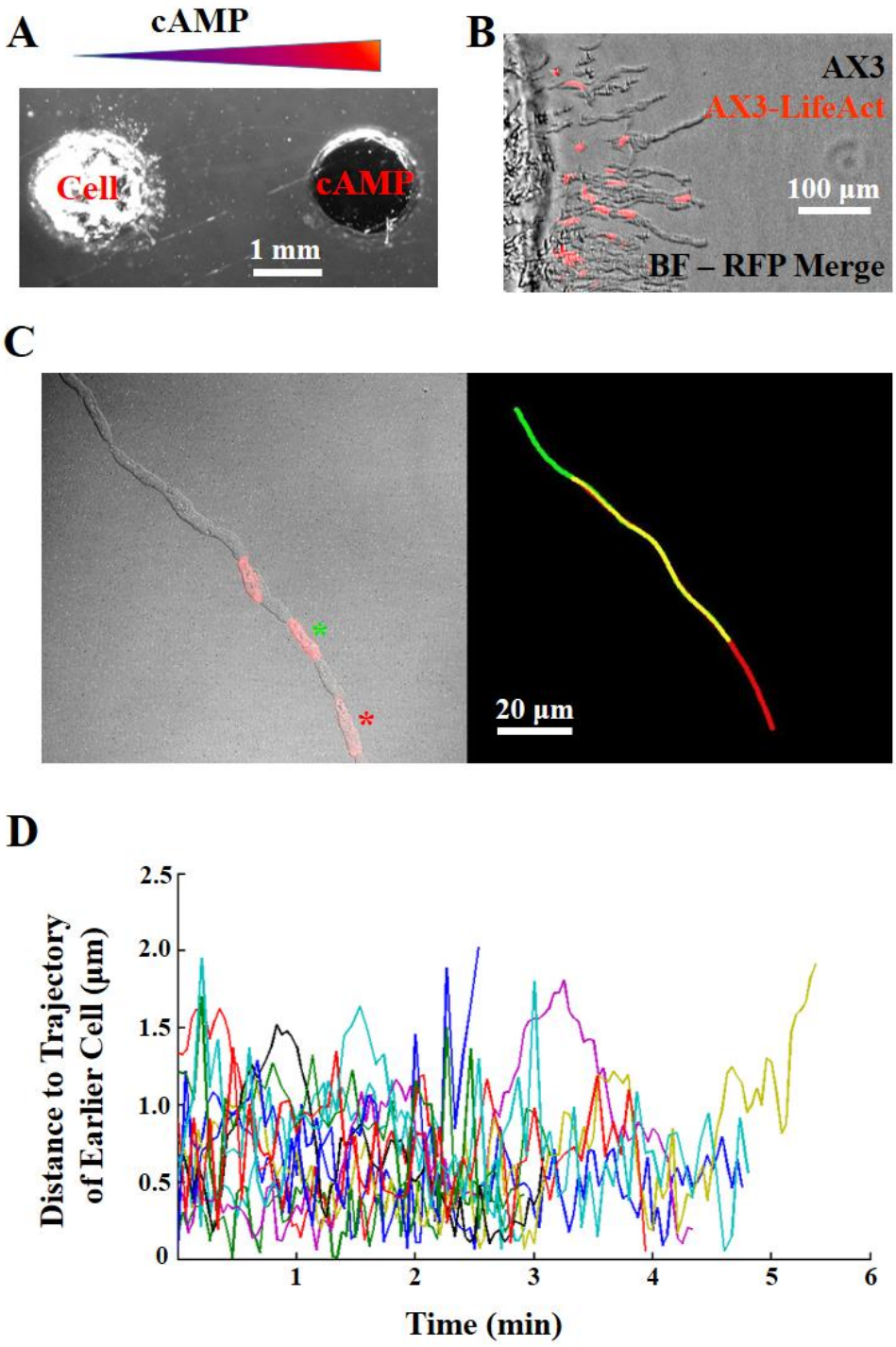

Figure 6.1: Cells accurately follow other cells in streams. (A) Cells migrate from one well to a signal (cAMP) containing well under-agarose. (B) AX3-lifeact-RFP cells mixed with WT AX3 cells form multicellular streams under agarose – overlay of bright-field channel and red fluorescent channel. (C) A typical multicellular stream (left) and

overlaid migratory trajectories of two cells (indicated with green/red stars) in the stream (right). (D) Minimum distance of one cell to the trajectory of an earlier cell in the same stream during its migration. Distance measurement of 11 cells plotted. Each curve represent one cell.

We have shown that individually migrating cells extend protrusions at their front that travel to their back on the cell boundaries and that, most importantly, the dynamics of protrusions govern the migration of individual cells (Driscoll et al. 2012)Wang et al. 2013). To get more insight into the behavior of cells in groups, we studied the travelling of protrusion waves on *Dictyostelium* cells migrating collectively in multicellular streams. We considered two streaming cells in direct contact as a unit and extracted their overall boundaries using the custom shape analysis Matlab code (Driscoll et al. 2012). A typical example is shown in Figure 6.2A. Note that the front cell (cell A) is ahead of the second cell we analyze (cell B), but in the back of another cell that is not fluorescently labeled. The stream of cells migrates to the right (blue arrow), and the boundaries of cell A and B are extracted every 2.5 seconds. Figure 6.2B shows an overlay over select cell boundaries. Protrusions (arrow heads), appearing like small bumps on the cell boundaries, initiate at the front of cell A and propagate to cell B across the head-to-tail contact region (black dash line).

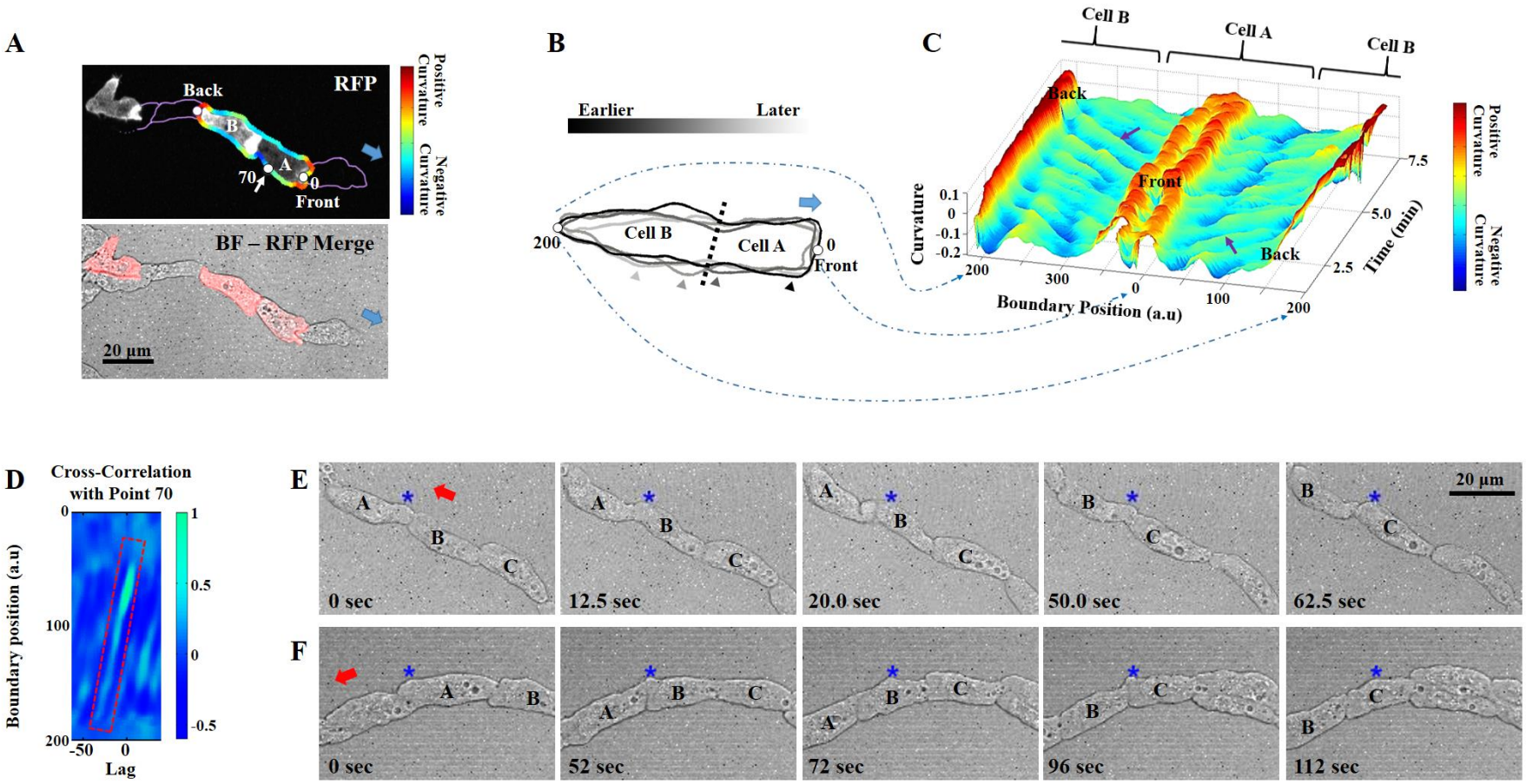
A
RFP
Back
B
A
70
0
Front
Positive Curvature
Negative Curvature
BF – RFP Merge
20 μm
B
Earlier
Later
200
Cell B
Cell A
0
Front
C
Cell B
Cell A
Cell B
Back
Front
Back
Curvature
0.1
0
-0.1
-0.2
200
300
0
100
200
Boundary Position (a.u)
7.5
5.0
2.5
Time (min)
Positive Curvature
Negative Curvature
D
Cross-Correlation with Point 70
Boundary position (a.u)
0
100
200
-50
0
Lag
1
0.5
0
-0.5
E
A
B
C
0 sec
12.5 sec
20.0 sec
50.0 sec
62.5 sec
20 μm
F
0 sec
52 sec
72 sec
96 sec
112 sec

Figure 6.2: Cells couple their protrusion waves in streams. (A) Two touching AX3-lifeact-RFP cells migrate as part of a multicellular stream. The boundary of these two cells is extracted and colored to indicate local boundary curvature. (B) Overlaid shapes of two cells in contact illustrate the propagation of protrusions from one cell to its follower cell. Shapes are aligned by their front point. (C) 3D kymograph of the spatio-temporal evolution of boundary curvature of two cells in contact illustrates coupling of protrusion waves on two cells. Red represents high positive curvature, indicating convex area; and vice versa. (D) Cross correlation of curvature dynamics between boundary points quantifies the coupling of waves.(E-F) Two phase contrast images sequences show that membrane protrusive bumps (marked with blue stars, stationary reference markers) are stationary with respect to the substrate in streams of migrating cells.

To quantify protrusion waves, we measured the curvature of cell boundaries (Figure 6.2A, color indicates of curvature). A time sequence of curvature outlines then allows us to study the dynamics of cell shapes. As illustrated in Figure 6.2C, the front and back of cells display high curvature regions. In addition, the small positive curvature regions (yellow/red regions) on the cell periphery indicate lateral protrusions. One of those is generated in the front of cell A (purple arrow) and travels in a wave-like manner across the cell-cell contact region to the back of cell B. The correlation between protrusion waves traveling on the two cells was further studied by calculating the cross-correlation of curvature dynamics between boundary points. For this purpose, each point on the bottom side of the boundary (point 1 to point 200) was compared to a reference point (point 70) (see Figure 6.2A). There may be multiple protrusive bumps simultaneously traveling on the boundary. To ensure the maximum

correlation is found based on the same protrusive bump traveling through each compared point and the reference point, the reference point on cell A has to be close to cell B. Point 70 is a point arbitrarily chosen from the back region of cell A. We tested other points from the same region, and they yielded similar correlation results. As shown in Figure 6.2D, the highest correlation is seen between point 70 and points surrounding it with a constantly increasing frame lag, suggesting that curvature dynamics of these points are highly coupled. The high correlation region (red dash box) starts at point 40 and extends to point 180, covering the bottom side of cell boundary. The protrusion dynamics on the other side of the boundary showed similar correlation (data not shown). We also found that the cross-correlation heat plot exhibits periodic patterns, suggesting that the protrusion waves are periodic. Together, these findings reveal that coupled protrusion waves travel between streaming cells. However, after examining the location of membrane protrusions with respect to the substrate, we found that the protrusions are generated at the same location on successive cells as the stream migrates forward (Figure 6.2E&F).

Since actin polymerization generates sufficient force to form protrusions and cells are capable of coupling their cytoskeleton through cell-cell contacts, we hypothesized that the coupled protrusion waves on cell streams are driven by coupled internal actin waves. We measured actin polymerization in WT cells expressing lifeact-RFP migrating either individually or within streams (Figure 6.3A, B & C). As shown in Figure 6.3D, individually migrating cells polymerize actin at their front, but the location of the polymerizing region along the cell boundary shifts continuously in a wave-like fashion which leads to slanted lines

in the kymograph (black dotted lines indicate the waves). This observation is consistent with our prior observations of actin waves along the leading edge of migrating *Dictyostelium* cells (Wang 2014). In contrast, as shown in Figure 6.3E, the location of actin polymerization appears stationary in cells that are following other cells in a stream. F-actin is exclusively seen at cell-cell contact regions (indicated by arrows in Figure 6.3B and black dots in Figure 6.3E), mostly at the front of cells. Thus coupled protrusion waves on streaming cells are not associated with traveling actin waves, but instead they appear associated with the ability of cells to accurately follow each other by polymerizing actin only at cell-cell contacts. This explanation is consistent with our observation that protrusions are stationary relative to the substrate (Figure 6.2E&F). Indeed, a recent study on the surface adhesion of pairs of cells reveals that the trailing cell uses the same adhesion sites as the leading cell (Bastounis et al. 2016). We also observed that cells in the leading position of multicellular streams exhibit actin waves on their sides (Figure 6.3F), much like individual cells, suggesting that protrusion waves are coupled with actin waves on leading cells. It therefore appears that the initiation of protrusion waves in cell streams is driven by actin waves in leader cells and that the propagation of protrusion waves within a stream is not associated with actin waves.

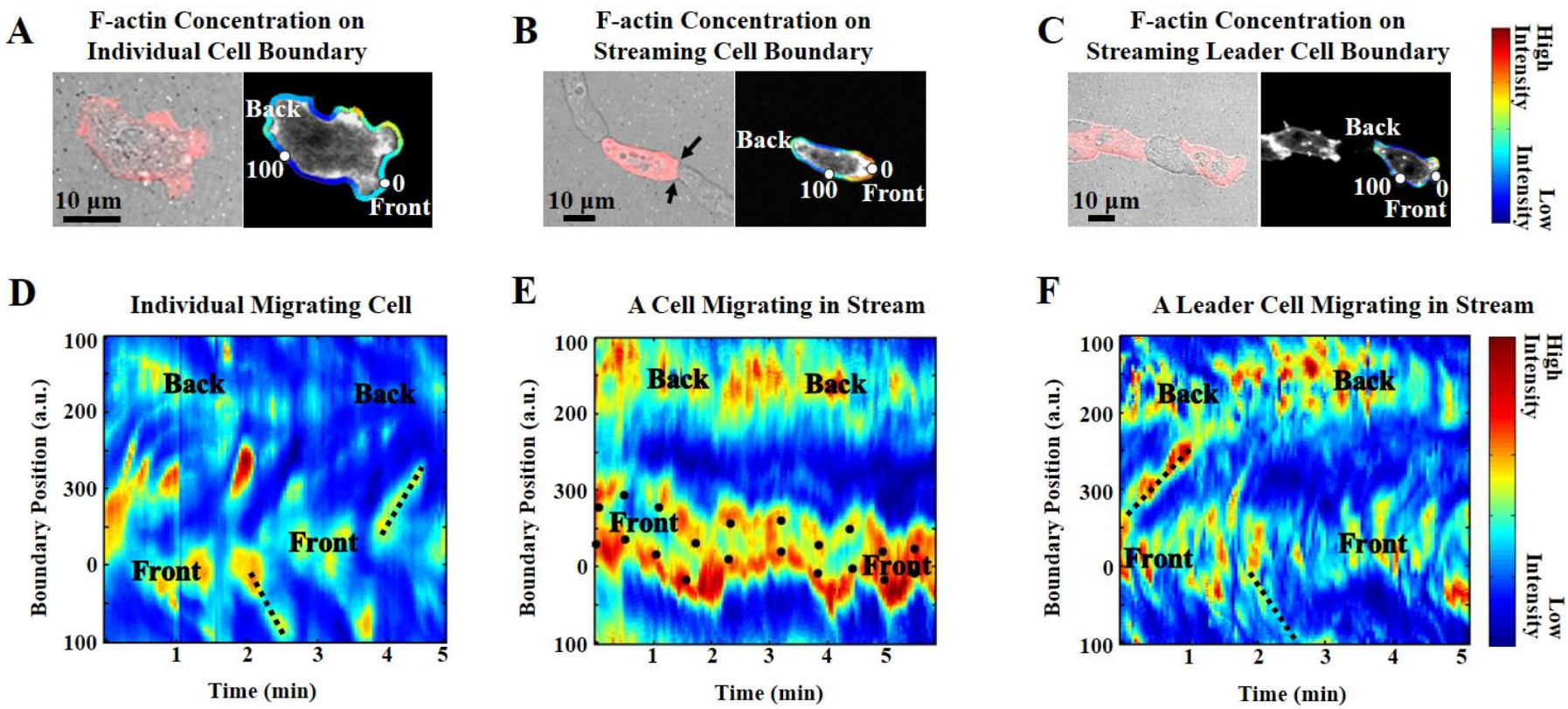
A
F-actin Concentration on
Individual Cell Boundary
Back
100
0
Front
10 μm
B
F-actin Concentration on
Streaming Cell Boundary
Back
0
100
Front
10 μm
C
F-actin Concentration on
Streaming Leader Cell Boundary
Back
100
0
Front
10 μm
High Intensity
Low Intensity
D
Individual Migrating Cell
Boundary Position (a.u.)
Time (min)
Back
Back
Front
Front
E
A Cell Migrating in Stream
Boundary Position (a.u.)
Time (min)
Back
Back
Front
Front
F
A Leader Cell Migrating in Stream
Boundary Position (a.u.)
Time (min)
Back
Back
Front
Front
High Intensity
Low Intensity

Figure 6.3, Follower cells in streams exhibit distinct actin polymerization than individual cells and leading cells. (A) Image of an individual AX3-lifeact-RFP cell with its boundary outline. Color of the outline represents F-actin concentration near the boundary point. Red: high concentration; blue: low concentration. (B) Image of a streaming AX3-lifeact-RFP cell with its intensity outline. (C) Image of an AX3-lifeact-RFP cell at the leading position of a cell stream with its intensity outline. (D) A kymograph illustrates the spatial-temporal evolution of F-actin distribution in an individual cell which exhibiting actin waves (black dotted lines). (E) A kymograph illustrates the spatial-temporal evolution of F-actin distribution in a streaming cell on which actin waves are suppressed. Black dots: cell-cell contact points. (F) A kymograph illustrates the spatial-temporal evolution of F-actin distribution in a streaming cell at the leading position of a cell stream on which actin waves are seen (black dotted lines).

6.3.2 Complex cell shape change can be divided into simpler modes

To understand how the distinct organization of the actin cytoskeleton in streaming cells alters the motion of cells, we set out to measure the progression of cellular shape change. Cells actively deform their shape during migration, involving protrusion, rotations, and contractions (Driscoll et al. 2014). These activities result in complicated shape change as shown in Figure 6.4A. To simplify the problem, we considered the cell shape change as a combination of different types of simpler shape changes, defined as shape change modes.

Each mode represents a certain feature of shape change. Shape change modes are calculated by applying principle component analysis (PCA) (Driscoll et al. 2014; Stephens et al. 2008; Keren et al. 2008) on a cell shape data set that is extracted from sequences of images containing individual and streaming cells under different experimental conditions (Materials & method). Shape change modes can be visualized as shape changes of an ellipse, as shown in Figure 6.4B. Black dotted ellipses represent the mean cell shape, and the red and blue outlines represent how each mode deforms the cell shape. Note that the red and blue outlines indicate the two signs of a single mode. For example, a positive mode 1 results in forward motion, whereas a negative mode 1 results in backward motion. Only the three most dominant shape change modes are plotted here. While one can identify as many modes as there are boundary points, each of which contributes independently to the actual shape change of cells, the actually observed shape changes are dominated by these three modes. Shape change modes are sequenced by the contribution of each mode to the overall shape changes of cells. The plot of cumulative contribution vs. the number of involved modes (Figure 6.5) confirms that only a few modes are required to describe cell shape changes: about 70% of cell shape change is contributed by the first three modes. In other words, a few important modes decide the main features of cell shape change, whereas others sculpture the detail features.

Because we are essentially parameterizing cell shape change, the contribution of each mode to the overall shape change of a particular cell is represented as C_1, C_2,…, C_N in the following equation:

Boundary Motion on Cell Shape $M = C_1*Mode1+C_2*Mode2+\ldots\ \ldots + C_N*ModeN$

The cell shape change is then reconstructed by adding up modes. Figure 6.4C shows the cell shape change at the leading edge of a cell. As shown in Figure 6.4D, the original shape (black outline) is changed by forward motion (mode 1, the grey dotted outline). Similarly, a contribution from mode 2 (C_2) and a contribution from mode 3 (C_3) are added, which brings the cell shape. By adding in more types of modes, the cumulative shape (grey dashed line) is approaching the real shape (grey dashed line in Figure 6.4C). Therefore, with values of three modes, the instantaneous changes in shape and thus motion of a cell can be well described. Since the shape change of every cell is represented by the same set of shape change modes, we can quantitatively compare shape change between frames and among cells and experimental conditions. Thus, we gathered 1000 shape change data from each experimental condition and perform statistical analysis.

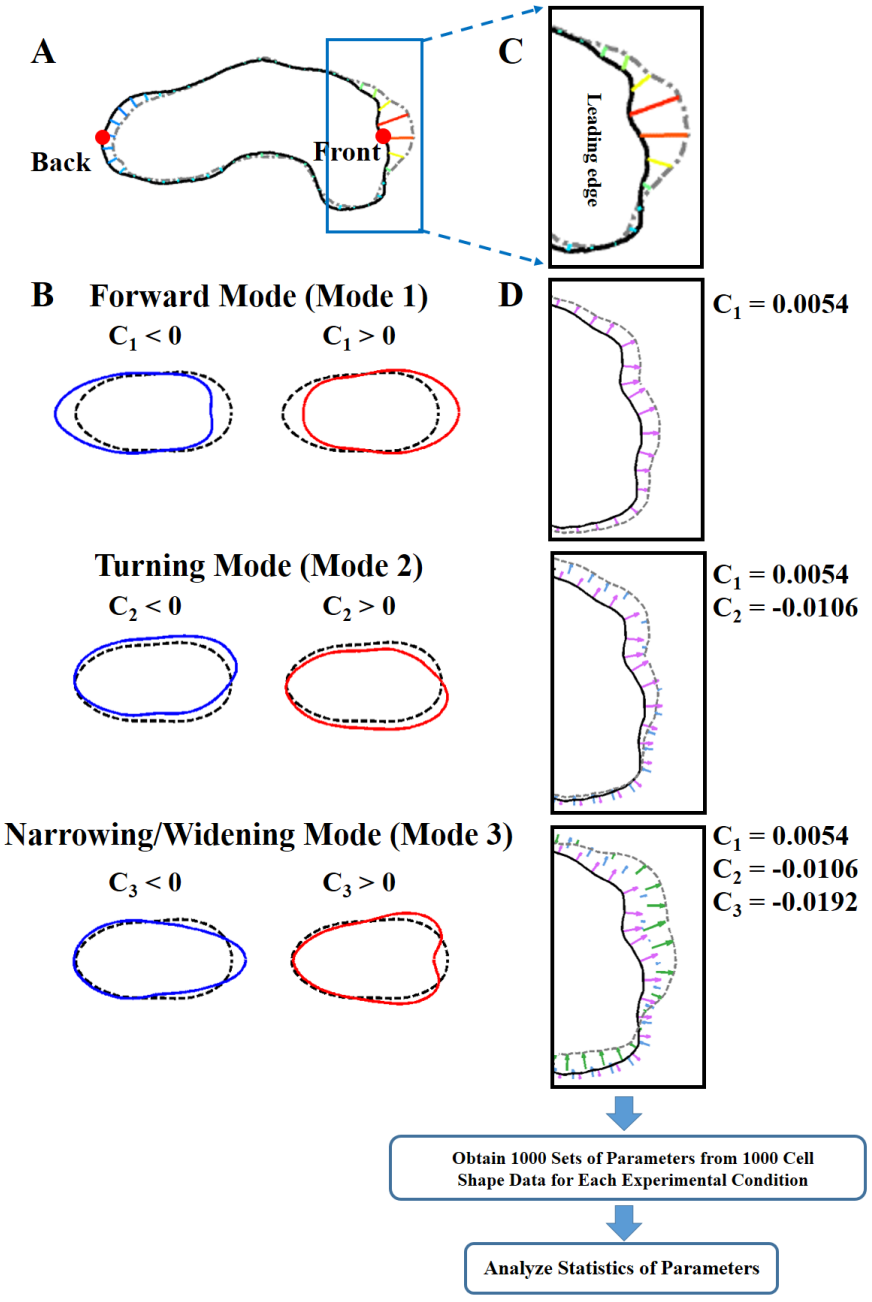

Figure 6.4 –Approximating Shape Changes and Motion with Three Shape Change Modes. (A) Overlaid shapes extracted from two successive images of one cell. Black solid outline represents initial shape; gray dashed outline represents the shape taken 5 seconds later. Lines connecting two shapes indicate cell shape change, colored by line

length. (B) The 3 primary shape change modes. Black dashed line: mean cell shape. Blue/Red lines: illustrations of how each shape change mode affects the cell shape. (C) Adding modes at the leading edge of a cell. (D) Cumulative motion is constructed by adding the 3 shape change modes. The magnitude of shape change mode N is C_N.

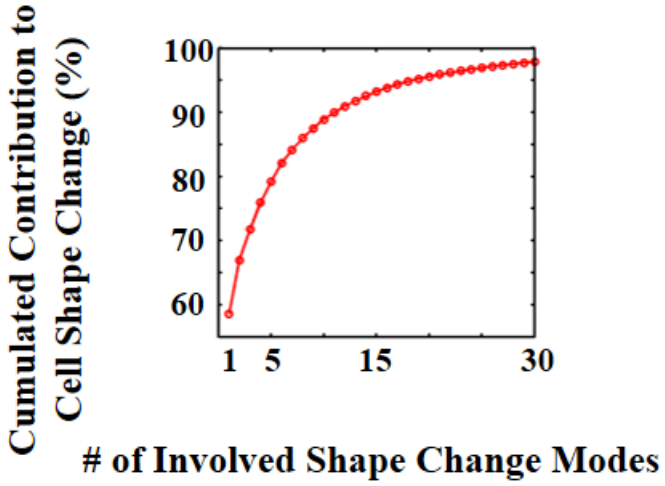

Figure 6.5 –Cumulated Contribution to The Shape Change Vs. Number of Shape Change Modes. Modes are sequenced by their contribution to the overall cell shape change.

6.3.3 Streaming cells exhibit narrowing of front protrusions

We first compared the shape change of individual and streaming cells. Typical schematic examples of shape change at the cell front are presented in Figure 6.6A for both positive and negative signs of each mode. The mean values are shown in Figure 6.6B, and the distribution of values for each mode is presented in Figure 6.7. To interpret these results, we now provide a qualitative description of these automatically (via PCA) extracted modes. The first shape change mode can be interpreted as the

global motion of cells, where cells uniformly move forward or backward. Since cell shapes were realigned by their front point before performing PCA, most cells exhibit forward motion, i.e. most values of mode 1 (C_1) are positive (Figure 6.7A). Hence, mode 1 is termed forward mode. Streaming cells exhibit higher forward motion than individual cells as the mean of C_1 is higher (Figure 6.6B). This is consistent with independent cell tracking analysis performed on the same set of data (Figure 6.8). Note that when we included all streams in a prior analysis, including very thick streams multiple cells wide, we measured similar cell speeds inside and outside of streams (McCann et al. 2010). Streams multiple cells wide were excluded from the current analysis because we are currently focusing on front-back guidance.

The second shape change mode can be interpreted as a turning mode. As shown in Figure 6.6C and Figure 6.7B, both individual and streaming cells show similar behaviors in this mode. Combined with our earlier observation that leader cells of streams exhibit left-and-right actin polymerization similarly to individual cells, we envision that turning decisions are made by leader cells within streams and transmitted to the rest of the cells in a stream, resulting in the similar turning behavior found on individual and streaming cells. The third shape change mode describes a more localized shape change at the leading edge of cells. Positive values lead to a narrower leading edge of the cell, while negative values result in a widening of the leading edge. We define these two shape change behaviors as front narrowing and front widening. The mean and the distribution of C_3 indicate that streaming cells exhibit front narrowing, while in individual cells front widening dominates (Figure 6.6D, right and Figure 6.7C).

Taken together, our findings show that the protrusive motion of streaming cells is localized at the cell front. Further analysis indicates that the front narrowing coincides with the region of contact with the leading cell, suggesting that leading cells effectively control the protrusive engine of their followers and that follower cells are able to accurately follow their leader. We envision that the coupling of protrusions waves between cells is enabled by the accurate following of protrusions from the leader cells, i.e., at cell-cell contact, the follower cell generates a protrusion at the same location as its leading cell.

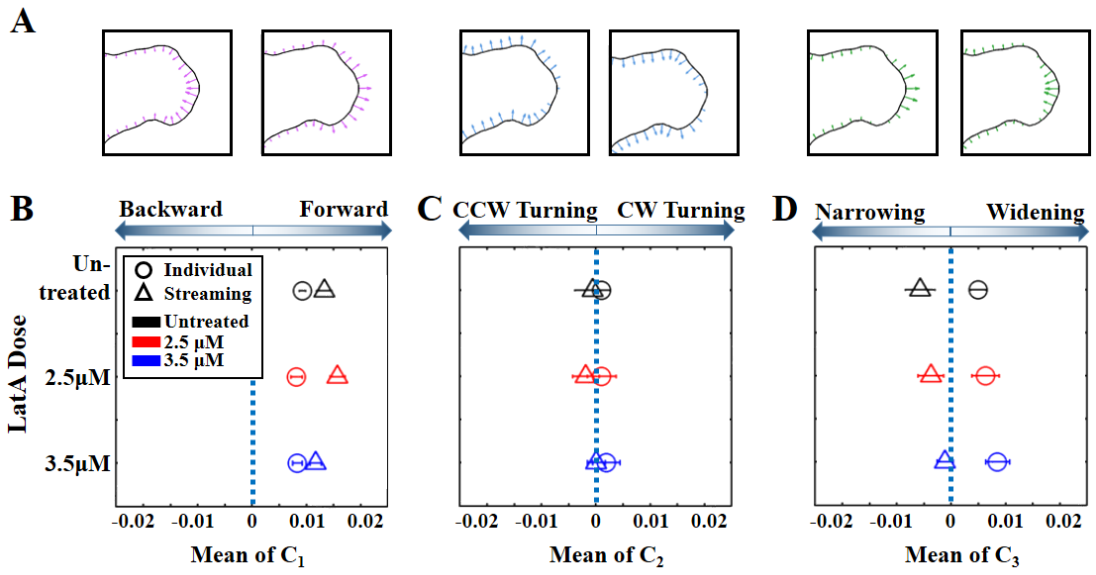

Figure 6.6 –Streaming cells exhibit front narrowing that can be reduced by Latrunculin A. (A) Schematic examples of shape change at the cell front for both signs of each mode. (B-D) Mean of value of individual and streaming cells changes when cells are treated with Latrunculin A.

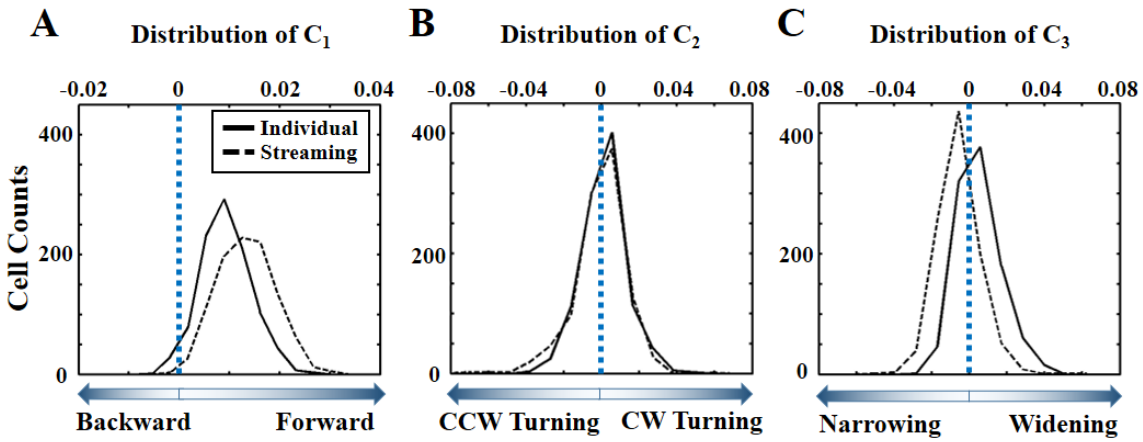

Figure 6.7 –Distribution of Values for Shape Change Modes in Individual And Streaming Cells.

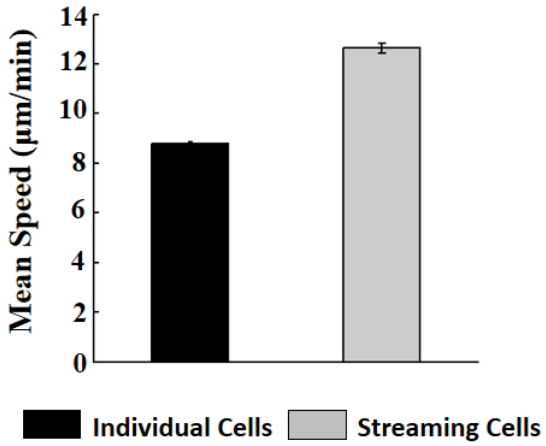

Figure 6.8 –Mean Migration Speed of Individual and Streaming Cells.

6.3.4 Reducing actin polymerization results in front widening

Streaming cells exhibit strong localization of protrusions and actin polymerization at their front. To investigate whether the front narrowing that is also observed in the shape change modes is actin-dependent, we used Latrunculin A (LatA)

at concentrations where actin polymerization is partially inhibited and cell motility is retained (McCann et al. 2014). We focused on cells treated with 2.5μM and 3.5μM LatA and compared them with untreated cells under both individual migration and streaming conditions. Note that the LatA concentrations are estimated initial concentrations. Cells were exposed to increasing LatA concentration as they migrate toward the drug source (Materials & Method). The mean and distribution of values of the three most important shape change modes are plotted in Figures. 6.6B-D, 6.9. We found that the mean of the mode indicative of forward motion, C_1, is reduced at higher LatA concentration (3.5μM), consistent with the known inhibition of motion at high LatA concentrations. In contrast, a widening of the front (C_3) was the main change in the shape change modes observed as the turning motion (C_2) was unaffected by LatA treatment.

While the interpretation of the change in C_3 is similar for both individual cells and cells in streams – i.e. the front widens – the magnitude of the mode increases for individual cells while it decreases for streaming cells. If the magnitude of shape change is distributed among more modes, the motion is more complex. This leads to an intriguing question: Do the changes in the magnitude of mode C_3 indicate that the complexity decreases with LatA treatment for streaming cells while it increases for individual cells? We cannot answer this question with the modes we analyzed so far, as they are based on all six experimental conditions to allow for comparison of mode magnitudes. To assess the complexity of shape changes, we performed PCA independently for all six conditions (control plus 2 LatA concentrations for individual cells and streaming cells) and calculated the contribution of each mode to the overall

shape change within each group. We found that shape change of individual cells becomes more complex with LatA treatment as shown in the cumulative contributions of shape change modes in Figure 6.10A. In untreated cells, the first 4 modes explain ~80% of cell shape change. For cells treated with 2.5μM or 3.5μM LatA, 6 and 8 modes are needed respectively to explain ~80% of cell shape change. The total contribution of the first 3 shape change modes decreases for individual cells upon LatA treatment (Figure 6.10B). In contrast, as shown in Figure 6.10A&B, the boundary motion dynamics can be explained with fewer modes for streaming cells treated with LatA. These findings reveal that individual and streaming cells respond differently to actin polymerization inhibition: individual cells migrate more irregularly with higher localized cell shape change, whereas streaming cells migrate with less complex motion. Taken together, these findings show that front narrowing of streaming cells is actin dependent as the reduction of actin polymerization decreases such localized shape change on these cells.

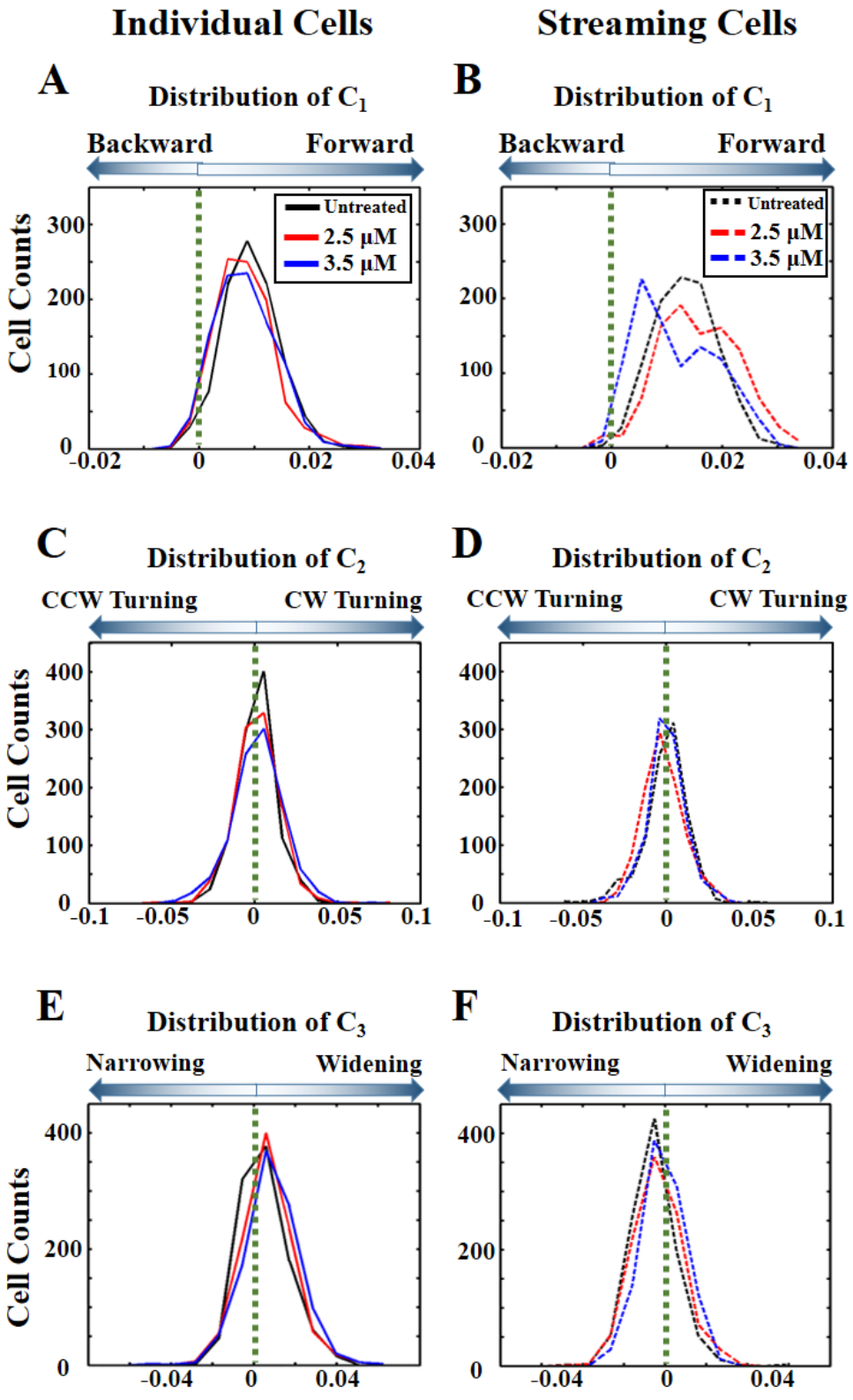
Individual Cells
Streaming Cells
A
Distribution of C_1
Backward
Forward
Cell Counts
Untreated
2.5 μM
3.5 μM
B
Distribution of C_1
C
Distribution of C_2
CCW Turning
CW Turning
D
Distribution of C_2
E
Distribution of C_3
Narrowing
Widening
F
Distribution of C_3

Figure 6.9 –Distribution of Values for Shape Change Modes in Individual and Streaming Cells with LatA Treatment. (A-B) Distribution of values of shape change mode 1 for individual cells and streaming cells under LatA treatment. (C-D) Distribution of values of shape change mode 2 for individual cells and streaming cells under LatA treatment. (E-F) Distribution of values of shape change mode 3 for individual cells and streaming cells under LatA treatment.

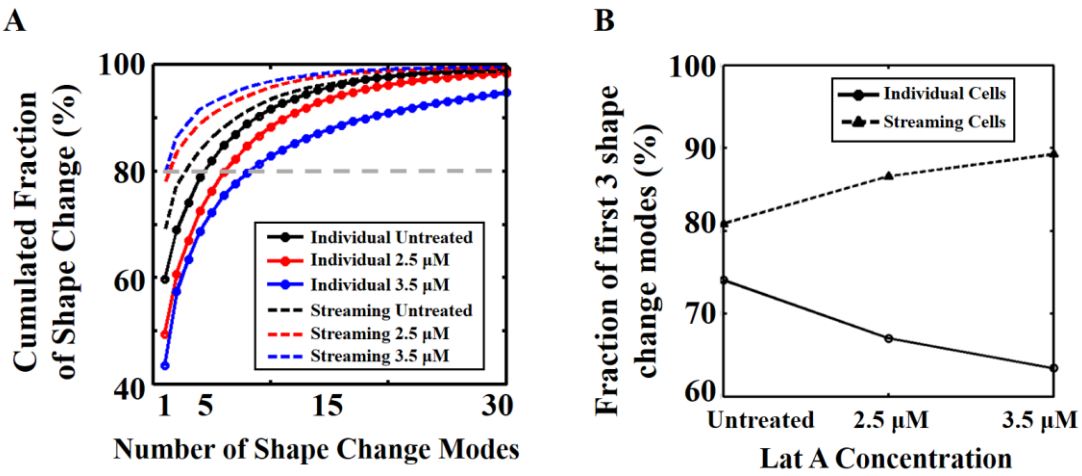

Figure 6.10 –Individual and Streaming Cells Adopt Different Strategies to Migrate under F-actin Inhibition. (A) Cumulative fraction of shape change vs. Number of modes for individual and streaming cells under control and 2 LatA doses. (B) The total contribution of first 3 shape change modes on individual and streaming cells.

6.3.5 Latruculin A treatment induces F-actin assembly on the side of streaming cells

We next studied changes in the distribution of F-actin upon LatA treatment. The spatial distribution of F-actin was obtained by measuring normalized fluorescence intensity at the cellular boundaries of WT cells expressing Lifeact-RFP. Figure 6.11A illustrates an intensity distribution outline obtained by using the custom

shape analysis Matlab program (Driscoll et al. 2012). As we did for our shape change analysis, the F-actin distribution along the cell boundary can be analyzed as a sum of orthogonal modes of the intensity distribution. PCA was used to identify the intensity distribution modes of WT-Lifeact-RFP cells migrating under different experimental conditions. The F-actin distribution along each cell boundary can be parameterized using the same math as before, though the modes and mode values now represent distribution of F-actin concentration hence we use the subscript F:

$$\text{F-actin distribution on cell cortex} = C_{F1}*Mode_F1+C_{F2}*Mode_F2+\ldots\ \ldots + C_{FN}*Mode_FN$$

Values C_{F1}, C_{F2}, etc. indicate the contribution of each intensity mode to the overall intensity distribution along the cell boundaries. As illustrated in the left panel of Figure 6.11B, the boundary of a typical cell is initially colored according to the intensity distribution of mode F1. As expected this only partially recovers the actual intensity distribution of this cell (Figure 6.11A). The cumulative intensity distribution of the first 2 modes and the first 3 modes, respectively, approach the actual intensity distribution. As we did for cell shape changes, we can again compare the values of modes (C_{F1}, C_{F2}, C_{F3}, etc) between cells from different experimental groups. Indeed, 1000 sets of values were obtained from PCA for each group and statistically analyzed.

We found that F-actin distribution is well represented by the first 3 intensity distribution modes, as 80% of intensity information is contained in these modes (Figure 6.12). The distributions of values of individual and streaming cells are shown in Figure 6.11C. Typical examples of intensity distribution on cells are shown under each corresponding distribution plot. Average cell shapes are shown (roughly

elliptical) and colors indicate the magnitude of intensity. Similar to shape change modes, there are two colored outlines for each mode, representing two opposite ways by which a mode can contribute to the intensity distribution, which are determined by the signs of the intensity values. As expected, the distribution of C_{F1} shows that, for both individual and streaming cells, the anterior of cells exhibit more F-actin than the rest of the cell boundaries. Yet, we found that about half of individual cells have F-actin on the sides of cell boundaries, whereas only a few streaming cells are in that mode (pointed by the purple arrow in the distribution plot of C_{F2}). This result further validates our observation in Figure 6.3, which showed that streaming cells suppress actin polymerization waves that travel along their sides.

We further investigated how the F-actin distribution responds to actin polymerization inhibition. As shown in Figures 6.11D & 6.13, while the distribution of values (C_{F1}, C_{F2}, C_{F3}) of individual cells does not significantly change upon LatA treatment, the distribution of F-actin is significantly enhanced on the sides of streaming cells, as more streaming cells are found in the region of $C_2 < 0$ (Figure 6.11E, red and blue dash line). Therefore, upon LatA treatment, the suppression of actin polymerization on the sides of streaming cells gradually disappears, suggesting that streaming cells re-organize their actin cytoskeleton to adapt to actin inhibition.

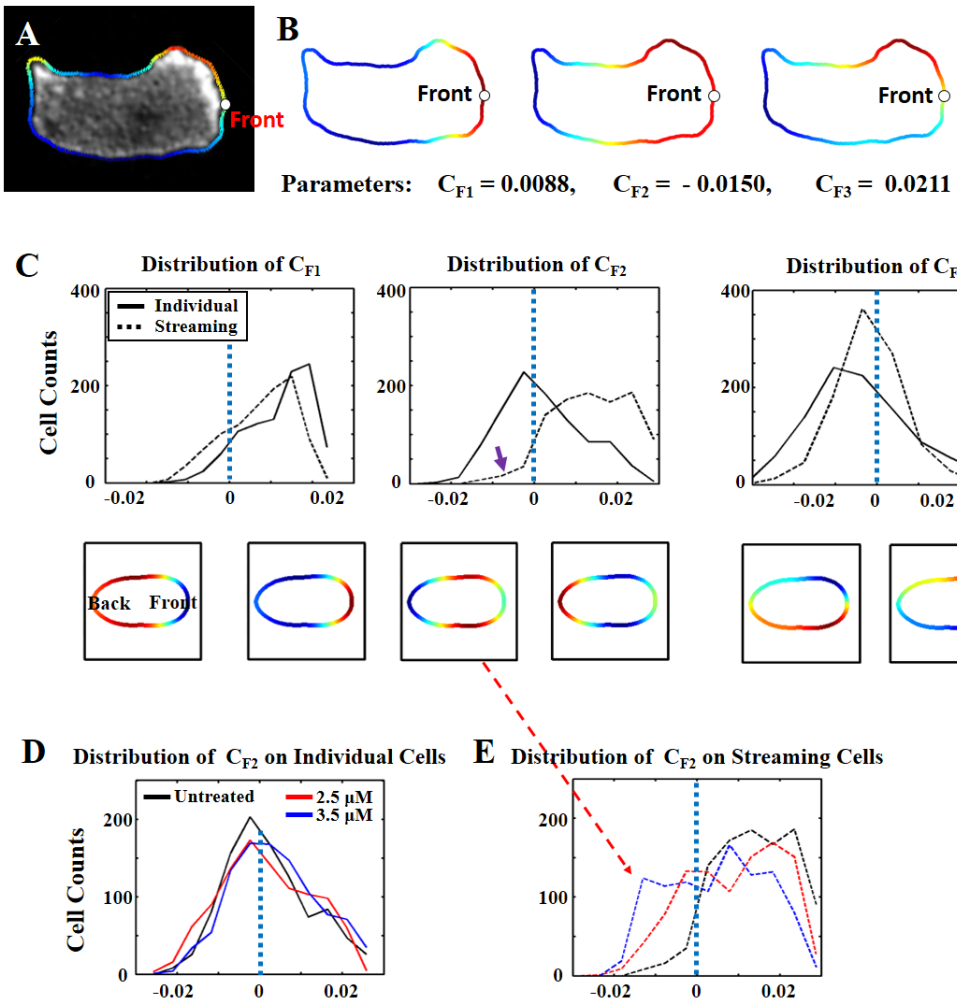

Figure 6.11 –The Restricted Distribution of Actin Polymerization nn Streaming Cells Disappears under LatA Treatment. (A) Image of an AX3-lifeact-RFP cell with extracted cell boundary. Color indicates F-actin concentration near each boundary point. Red: high concentration; blue: low concentration. (B) With contributions from 3 intensity distribution modes, the cumulative intensity distribution looks similar to the actual intensity distribution in (A). (C) Upper plots: Distribution of values of individual cells and streaming cells for the first 3 intensity distribution modes. Lower: schematic examples of intensity distribution on cell boundaries for corresponding intensity modes.

(D) Distribution of C2 for individual cells under LatA treatment. (E) Distribution of C2 for streaming cells under LatA treatment.

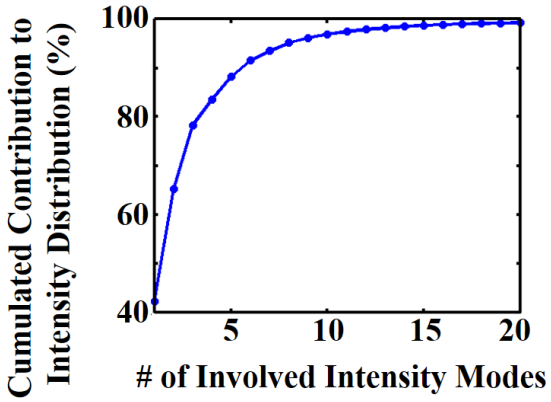

Figure 6.12 –Cumulated Contribution to the Lifeact-RFP Intensity Vs. Number of Intensity Modes. Intensity modes are sequenced by their contribution to the overall distribution of intensity.

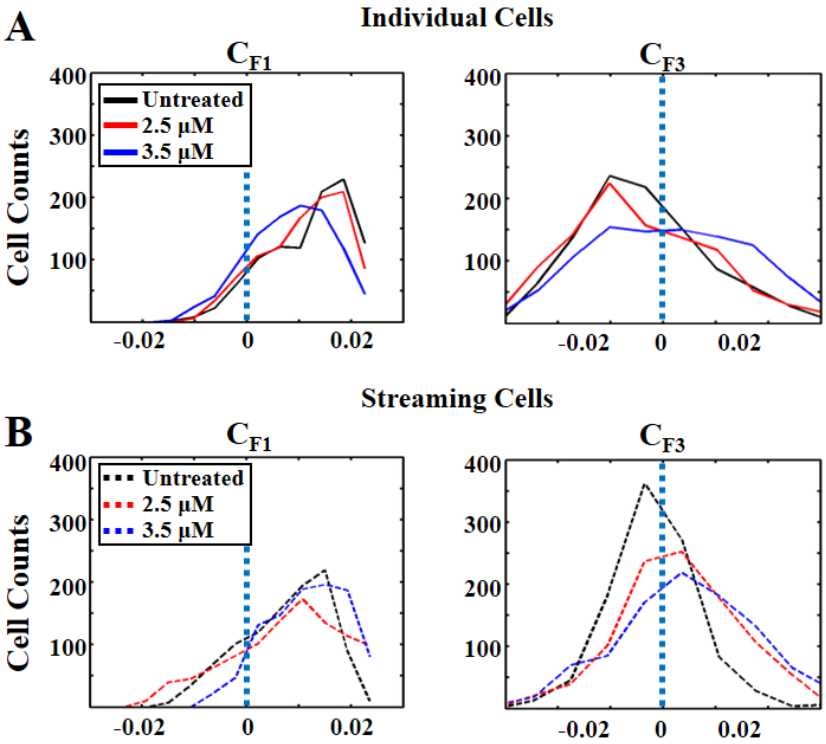

Figure 6.13 –Distribution of Values for Intensity Modes in Individual and Streaming Cells with LatA Treatment. (A) Distribution of values of 3 intensity modes for individual cells under LatA treatment. (B) Distribution of values of 3 intensity modes for streaming cells under LatA treatment.

6.3.6 Latrunculin A treatment alters wave coupling between cells

How do cell-cell coupling and streaming change under the influence of LatA? Images of typical cellular streams under 2.5μM and 3.5μM LatA treatment are shown in Figure 6.14A&B. Despite the noticeable morphological change, LatA treated streams retained a certain level of motility and actin activity. The spatio-temporal evolution of boundary curvature of pairs of cells in streams are shown in Figure 6.14C&D, where the curvature of each boundary point from successive images is plotted vertically and aligned along the time axis. The front of the leading cell exhibits high curvature, as do other regions on the cell boundaries. At low LatA concentration, some protrusions (yellow) originate at the leading cell and travel to the following cell across the cell-cell contact (Figure 6.14C). However, only few protrusions travel across cell-cell contacts with higher LatA treatment (Figure 6.14D).

We next investigated how cell migration is globally influenced by LatA treatment by performing under-agarose assays with different LatA concentrations and taking time-lapse images. For these experiments, a 90%/10% mixture of WT and WT/Lifeact-RFP cells were allowed to migrate in a gradient of cAMP and LatA. This allowed the cells to migrate out of the well and be slowly exposed to higher concentration of LatA. Cell migration tracks were obtained from the RFP channel by using a previously developed cell tracking Matlab program (McCann et al. 2010). As

shown in Figure 6.15A, the average cell speed remained at a comparable level when actin polymerization is partially inhibited (LatA < 5μM). However, while the instantaneous speed of untreated cells levels off, the instantaneous speed of LatA-treated cells is decreased as the cells migrated up the LatA gradient (Figure 6.15B). Interestingly, while moderately-inhibited cells (LatA < 5μM) retained significant motility throughout the experiment, the collective migration pattern significantly changed (Figure 6.14E). Indeed, the overall shape of the cell groups changed from the stream-like shapes shown in Figure 6.3 to cohesive cluster-like shapes. Concomitantly, head-to-tail cell-cell alignments were less obvious in LatA-treated conditions. These findings suggest that cells require localized shape change at cell-cell contact regions to mechanically coordinate with neighboring cells and maintain multicellular head-to-tail streams.

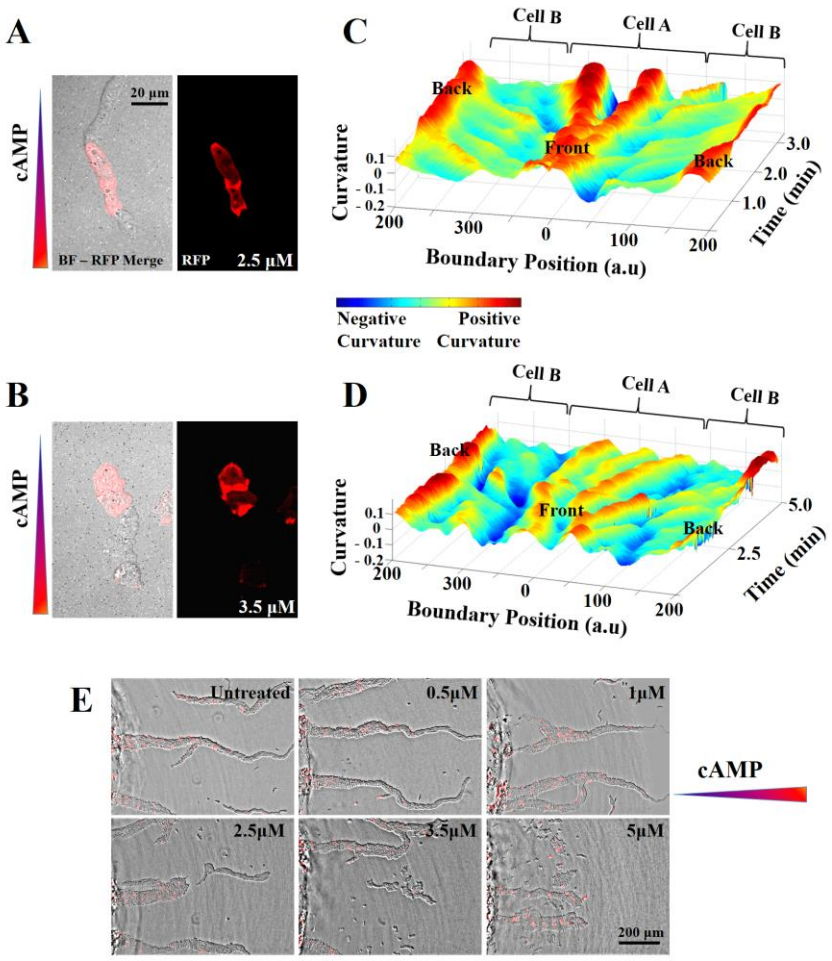

Figure 6.14 –Lata Treatment Alters Cell-Cell Interactions. (A-B) images of multicellular streams formed by mixed AX3-lifeact-RFP cells and unlabeled AX3 cells under 2.5µM and 3.5µM LatA treatment, respectively. (C-D) 3D kymographs illustrate the spatial-temporal evolution of curvature of two contacting cells under LatA treatment, indicating coupled protrusion waves reduce during LatA treatment. (E) The pattern of collective migration of *Dictyostelium* alters under the influence of LatA.

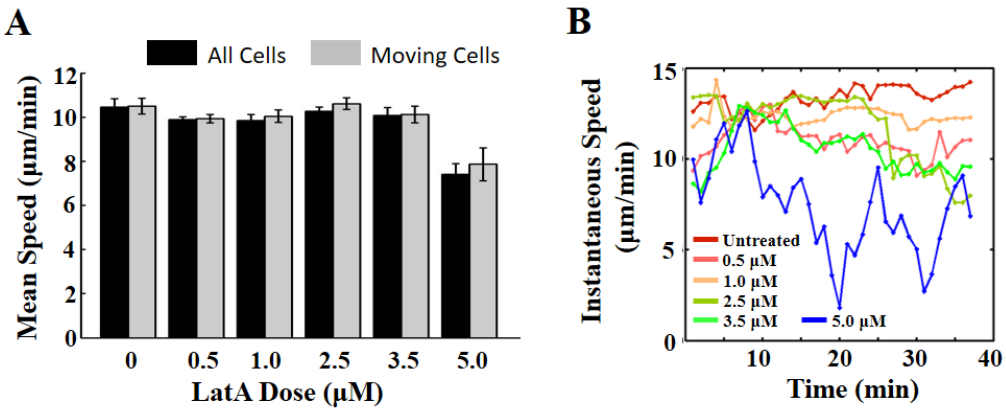

Figure 6.15 –The Mean and Instantaneous Speeds of Cells under LatA Treatment. (A) The average speed of cells under different does of LatA treatment. Black bars: average speed of all cells in the microscopic field of view; gray bars: average speed of cells that moving faster than a certain threshold. (B) Instantaneous speed of cells under LatA treatment. Selected cells were tracked from the beginning of the migration movies for the following 45 mins.

6.3.7 The relay of chemical signal is similar inside and outside of streams

It is well established that the relay of cAMP signals between cells is essential for streaming. The binding of cAMP to its specific receptor on the cell surface activates a series of intracellular signaling pathways that eventually lead to the synthesis and secretion of additional cAMP by the adenylyl cyclase (ACA), which is enriched at the back of cells (Dormann et al. 2002; Kriebel et al. 2003). The produced cAMP is secreted and relayed to neighboring cells. It has been shown that the distribution of ACA at the back of cells is essential for streaming (Kriebel et al. 2008; Kriebel et al. 2003). Using WT cells expressing ACA-YFP, we assessed ACA intensities in individual and streaming cells. Similar to the analysis of F-actin

distribution on cell boundaries, the distribution of ACA on cell boundaries is considered as a cumulative distribution based on a set of ACA intensity distribution modes. These modes were obtained by PCA from 1900 ACA distribution outlines for both individual and streaming cells. We found the distribution of ACA to be remarkably robust and simple as 74% of ACA distribution information was contributed by the first mode (Figure 6.16). For both individual and streaming cells, ACA was dominantly distributed at the back of cells (Figure 6.17). We found no significant distribution differences between individual and streaming cells, indicating that cells do not significantly change cAMP signaling upon the formation of cell-cell contacts in multicellular streams.

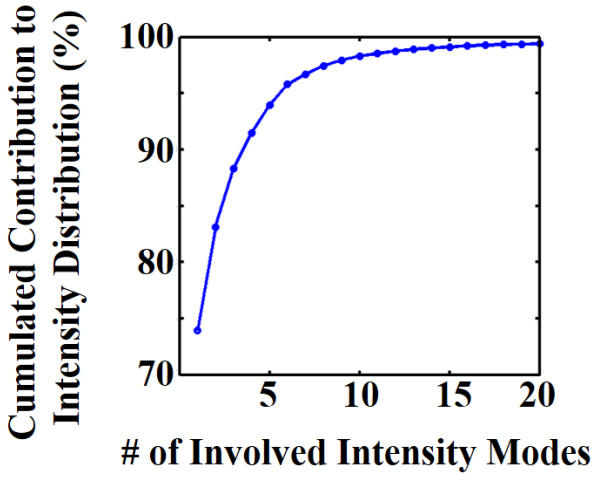

Figure 6.16 –Cumulated Contribution to The ACA-YFP Intensity Vs. Number of Intensity Modes. Intensity modes are sequenced by their contribution to the overall distribution of intensity.

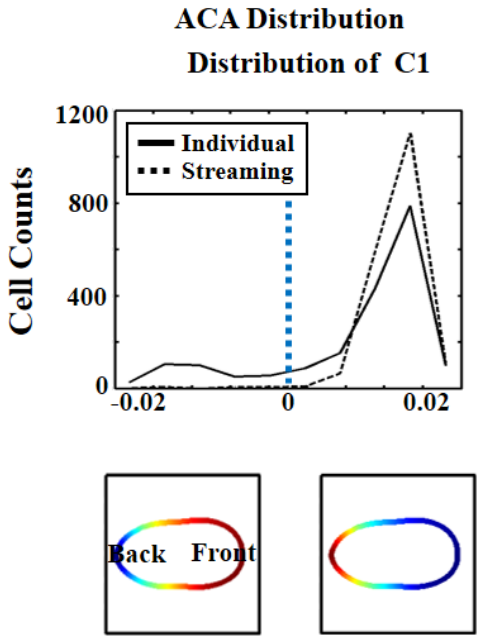

Figure 6.17 –Distribution of ACA is Similar in Individual and Streaming Cells. Upper: Distribution of values of individual cells and streaming cells for the first ACA distribution modes. Lower: Examples of ACA distribution on cell boundaries.

6.4 Conclusion and Future Work

Our main finding is the suppression of actin polymerization waves in collective cell migration. Actin polymerization waves, seen at the leading edge of individually migrating cells, disappear once cells follow other cells in a stream, and actin exclusively polymerizes at cell fronts where the cell-cell contact is formed.

Further analysis of cell motion and migration indicate that the switch of actin behavior to the stable state enables the close coordination of cell motion in groups. PCA on cell shape change shows that individual cells migrate more irregularly as they require more shape change modes to describe boundary motion. Collectively

migrating cells exhibit less variety in their cell shape change, especially when the actin polymerization is globally reduced. Uniform forward motion is dominant in these cells. In addition, actin polymerization at cell-cell contacts enables the front narrowing in the same region, which may promote cells to accurately follow their leading cells and enable the coupling of their protrusions. Moreover, breaking up the stable state of the actin cortex by reducing F-actin with LatA decreases the coupling of protrusion waves between cells and leads to the disruption of collective migration.

Finally, it is important to note that the leading cells of streams still exhibit wave-like actin assembly similar to individual cells and thus generate alternating protrusions on both sides of the cell. Since following cells in a stream polymerize actin at cell-cell contact, they are able to follow faithfully the footprint laid out by the leading cell down to the level of localized protrusions that persist from cell to cell shown in Figure 6.2C. One consequence of this faithful following of the leader cell is that the characteristics of motion of all cells in a stream are expected to be similar to the motion of the leader cell. In turn, that is similar to individual cells. Thus, our findings explain why cells in a stream exhibit the same directionality and cell speed as individual cells (McCann et al. 2010).

6.5 Materials and Method

6.5.1 Tissue culture and differentiation

Wild-type *Dictyostelium discoideum* (AX3) cells, AX3-Lifeact-RFP cells, ACA-YFP AX3 cells, and PH-crac-GFP AX3 cells were cultured at 21 ℃ in HL-5 medium containing 50 μg/mL Hygromycin (for AX3-Lifeact-RFP cells) or 20μg/mL

G418 (for ACA-YFP AX3 cells and PH-crac-GFP AX3) at density no higher than $5*10^6$ cells/mL.(Sussman 1987) Cells were harvested 6 hours before imaging and developed for 5 hours in development buffer (5 mM KH_2PO_4; 5 mM $Na_2HPO_4*7H_2O$; 2 mM $MgSO_4$; 0.2 mM $CaCl_2$), following the differentiation procedure previously described in other papers.(Devreotes et al. 1987; McCann et al. 2010; Wang et al. 2014) Then, developed cells were spin down at 9000 rpm and re-suspended in phosphate buffer (5 mM KH_2PO_4; 5 mM $Na_2HPO_4*7H_2O$). Suspended cells were incubated with 2mg/mL caffeine for 30 minutes before added into wells of under-agarose migration assay.

6.5.2 Under-agarose migration assay

The procedure of under-agarose assay experiments is adapted from a previously published protocol.(Kriebel & Parent 2009) For most experiment 2-well Lab-tek chamber slides (Lab-Tek, Nunc) were used. For experiments shown in Figure 6.14E, 6-Well Glass Bottom Plates (Cellvis) were used. Chambers were pre-washed by 1 M HCL for 15 minutes and then triple rinsed with water. Then, each chamber was incubated with 2 ml 1% w/v of BSA (Sigma) for 2 hours. When it is done, BSA solution was aspirate and 1.2 ml 0.5% agarose (liquid) was added into each chamber (3 ml agarose for 6 well plates). Slides were left on the bench for curing at room temperate for 30 minutes before moving to the 4℃ refrigerator to continue curing for another 30 minutes. 14.5 gauge hypodermic tubing was used to drill two wells (2 mm in diameter, 4mm center-center apart) through the cured agarose in each chamber. One well is filled with 1uM of cAMP, which diffuses in agarose gel and forms a

cAMP concentration gradient. The other well is filled 15 minutes later with caffeine-treated cells which then migrated toward the first well guided by the cAMP gradient.

For experiments with Latrunculin A treatment, a mixture of cAMP and LatA (0 (only DMSO for untreated), 5μM, 10μM, 25μM, 35μM, 50μM) was added into one well in the agarose, and cells were added into the other well 15 minutes later. A gradient of cAMP and LatA then build up in the agarose gel, which guide cells to migrate towards the higher gradient forming multicellular streams. During the migration, cells are treated by LatA with gradually higher concentration. Base on mathematical models, the concentration of LatA at the edge of the well of cell, where cells start to migrate, is about 10% of the concentration that added into the well of cAMP and LatA mixture, i.e., the actual initial doses of LatA treatment are: 0, 0.5μM, 1μM, 2.5μM, 3.5μM, 5μM. Moreover, instead of being treated with a constant LatA dose, cells are exposed to a gradient of LatA with increasing concentration in the under-agarose migration assay.

6.5.3 Microscopy

Cell migration movies used in PCA analysis and shape analysis were taken under Zeiss 510 confocal microscope with a 60X objective for every 2.5 seconds. Cells were added into the under-agarose assay chamber 15 minutes prior to imaging to allow cells to migrate out of wells. Other cell migration movies, like ones shown in Figure 6.14E, were taken under Zeiss Observer.Z1 microscope (Zeiss, Goettingen, Germany) equipped with an automated moveable stage using a 10X objective. Movies for all experimental conditions were simultaneously taken with 1.5 minutes interval.

6.5.4 Imaging processing and shape analysis

Since cells migrate above coverglass and under the agarose gel in the under-agarose migration assay, they are in an environment that has limited space in the Z direction. Thus, cortex waves on cell boundary are well confined in the X-Y plane. We extracted 2D shapes of cells by a custom shape analysis Matlab program (The Mathworks, Natick, MA) as described in previous publications. (Driscoll et al. 2012; Wang et al. 2014) 400 points on each cell boundary are evenly chosen, and boundary points are 1:1 mapped between two successive shapes according to their front point. The front is defined in this way: each cell shape is fitted to an ellipse; there are two points at where the major axis of the ellipse meets the cell shape. The boundary motions around these two points are compared, and the point with larger outward motion is set to be point 0.

Curvature around each boundary point is obtained by fitting the point and two nearby points into a circle and calculating the reciprocal of the radius of the circle. Boundary intensity is obtained by drawing a circle around each boundary point and calculating the average fluorescent intensity within that circle. Then, the value of the intensity of each point was normalized by making the maximum and minimum intensity value to be equal for every cell boundary.

Besides individual and streaming cells, some cells migrate in bulk groups, where they form cell-cell contact on the side of cell boundaries. They are removed from our analysis because we mainly focus on the front-back guidance in the study. In other words, streaming cells only form front-back contact with other cells.

6.5.5 Principal component analysis

Cell shape change modes and F-actin intensity modes are calculated by principle component analysis (PCA) based on the imaging data collected from AX3-Lifeact-RFP cells. We collected sequences of images containing individually and streaming AX3-Lifeact-RFP cells under different experimental conditions, from which thousands of cell shapes are extracted and shape change and intensity are calculated. The shape change of cells can be gained by overlaying cell shapes extracted from two successive images and calculating the moving distance of each boundary point, as illustrated in Figure 6.4A. For the 1:1 mapping between the two shapes, they are aligned by front point (point 0), which is decided by cell orientation.

Cell shape change data and intensity data are randomly selected (1000 shapes from each condition), and PCA was performed on these two data sets respectively using Matlab build-in function to find out modes. Intensity modes for ACA were calculated similarly based on imaging data collected from ACA-YFP AX3 cells. 1900 from each condition are randomly selected for analysis respectively.

Chapter 7: Summary and Future Directions

7.1 Summary

This thesis has discussed how cells adapt their motion to neighboring cells and extracellular substrates by actively regulating the cytoskeleton and shape dynamics. Cells adhere to extracellular substrates and neighboring cells during collective migration and perceive various signals from their surrounding environment. These signals are further processed intracellularly via a complex signaling network, which has been extensively studied in the past decade (Devreotes & Horwitz 2015; Garcia & Parent 2008; Penela et al. 2014). This thesis focuses on understanding the output of this signaling network: the actin polymerization and the subsequent cell shape changes, both of which exhibit dynamic wave-like behaviors. In this thesis, I perturbed these waves by altering cell-substrate and cell-cell interactions and by active micromanipulation, which led to different actin polymerization, cell shape changes, and cell motion. These studies provide insights in how mechanical and intracellular waves govern collective cell migration.

Much of my work aimed to understand how cells coordinate their motion during collective migration. As previously shown, the motion of individual cells is governed by wave-like cell shape dynamics. (Driscoll et al. 2012; Driscoll et al. 2011). Hence, I analyzed the shape dynamics of pairs of *Dictyostelium* cells migrating head-to-tail (Chapter 5). I found that protrusion waves travel across cell-cell contact on pairs of cells. Then, I expanded my studies to streams of cells and further

quantified protrusion waves (Chapter 6). I found that protrusion waves are highly coupled between streaming cells. I further studied how cell-cell coupling affects cells motion by applying principal component analysis (PCA) on cell shape data. PCA yields a set of shape change modes, each of which represents a particular feature of cell shape change, such as protrusion, rotation, etc. I found that compared to individual cells, streaming cells exhibit more localized anterior protrusive motion, which I termed front narrowing. Here, I propose that front narrowing, which occurs at the cell-cell contact region, is important for the coupling of protrusions between cells because it allows leading cells to efficiently guide the protrusive motion of the follower cell and the follower cell to accurately follow their leader cells. Such precise following is also reflected at the individual protrusion level, where a follower cell's protrusion is generated at the same location as its leader cell's protrusion.

As indicated in previous studies, individually migrating cells exhibit actin polymerization waves that are associated with membrane protrusions (Gerisch et al. 2004; Gerisch et al. 2009; Driscoll et al. 2015) . However, as described in Chapter 6, I found that actin polymerization waves are significantly suppressed in streaming cells, indicating that the coupling of protrusion waves in streaming cells is not governed by traveling actin polymerization waves. Note that the leading cells of streams exhibited actin polymerization waves, and associated alternating protrusions, suggesting actin polymerization is still associated with the initiation of protrusions seen on the sides of streams. My studies further showed that streaming cells exclusively produce F-actin at cell-cell contact regions, especially at cell fronts,

which enables front narrowing. With LatA treatment, which sequesters actin monomers and thus suppresses active actin polymerization, polymerized actin was found on the side of cells, which reduces front narrowing and in turn reduces coupling of protrusion waves. These results further support the conclusion that wave-like propagation of protrusions on the side of cell streams are not actin-driven.

I observed the switch of actin polymerization from a wave-like state to a stable state upon the formation of cell-cell adhesion (chapter 6), which suggests that the actin cytoskeleton is a dynamic system. Indeed, previous studies indicate that the actin cytoskeleton exhibits distinct behaviors under different circumstances. The Losert lab has previously found that actin waves are guided by nanoscale ridges, which are very different with actin waves in migrating cells on flat surfaces (Wang et al. 2014; Driscoll et al. 2014). Stable actin polymerization is seen wrapping around nano-scale obstacles (ongoing research in Losert's lab). Moreover, actin filament assembly significantly varies when cells are exposed to distinct microenvironments, and cells readily switch from one behavior to another as they enter a different extracellular matrix (Doyle et al. 2013). Together, these findings suggest that the actin cortex is a dynamic system that can quickly switch between states in response to external triggers.

My studies also suggest that cell-surface adhesions are essential for the coupling between cells migrating collectively. As described in Chapter 4, the chemical composition of surfaces affects cell-cell adhesion, resulting in distinct collective migration patterns. Moreover, cells with a surface adhesion defect (*Talin*

A null cells) exhibit significantly different cell-cell interactions: they aggregate by clumping instead of by head-to-tail streaming. I examined another case, where cells were suspended on a surface coated with PEG, which prevents cell-surface adhesion (Chapter 5). The loss of cell-surface adhesion led to a different aggregation behavior compared to adherent cells. Suspended cells still exhibited wave-like protrusions, but the protrusions were not coupled between neighboring cells, suggesting that the coupling of protrusion waves is surface-adhesion-dependent. Indeed, the location of protrusions was stationary with respect to the surface when the whole cell streams migrated forward (Chapter 6). Thus, I hypothesize that protrusions on the sides of streaming cells are associated with cell-surface adhesions. This hypothesis is supported by a recent study showing that successive cells use the same surface adhesion sites (Bastounis et al. 2016). Thus, these results indicate that collective migration requires a balance between cell-cell and cell-surface adhesions.

Such a balance is reached via the regulation of the cytoskeleton. My studies revealed how collectively migrating cells assemble their cytoskeleton in response to varying cell-surface adhesions. Chapter 4 showed that cells actively regulate their cytoskeleton to retain optimal cell-surface adhesions in response to different types of surfaces. Cells lacking the link between actin and surfaces (*talin A null* cells) could not retain optimal surface adhesions. Without cell-surface adhesions, shown in Chapter 5, cells assembled actin on the periphery of groups instead of in cell-cell contact regions. This distinct actin assembly pattern facilitated the aggregation of suspended cells by merging small cell clumps into larger clumps.

7.2 Future Directions

This thesis reveals that cells migrate in a coordinated manner during the head-to-tail streaming process. The coupling between cells is enabled by front narrowing, i.e. protrusions that are confined to the cell-cell contact region, which is associated with exclusive actin filament assembly in the same region. The restricted F-actin assembly and coupling of protrusions is cell-surface adhesion-dependent. These findings raise many new questions:

How does the restricted actin polymerization at cell-cell contacts drive local forces and motions to facilitate cell-cell coupling?

This thesis shows that the coupling of protrusion waves is associated with specific actin polymerization at cell-cell contacts. However, how does actin polymerization generate forces, and in turn, drive the localized motion at cell fronts to facilitate the coupling of protrusions remains unclear. I found that the restricted actin polymerization exhibits an oscillating on-and-off manner at cell-cell contacts. I speculate that such oscillating behaviors are related to the periodic generation of protrusions at cell fronts. In the case that a protrusion travels to the back of a cell, the protrusion presents an obstacle to its follower cell. The obstacle may bring two possible consequences: (i) higher forces is required to push on the obstacle so that the actin polymerization is enhanced at the front of the follower cell. Recent studies provide evidence from molecular level showing the constraint or force applied on cells increases the density of actin filaments increases (Fletcher 2010; Bieling et al.

2016; Diz-Muñoz et al. 2013).(ii) the growth of actin filaments is constrained by the obstacle so that F-actin grows slightly sideway. Indeed, the packing of filaments changes when force is applied on cell membrane. Normally, new actin branches grow at 70 degrees with respect to the existing filaments, which determines the angle of filaments attacking cell membrane. This angle decreases when the external forces increases, reflecting some geometry change of actin network, such as the bending of actin filaments or branch-points made by Arp2/3 (Bieling et al. 2016).

The change of actin network assembly leads to the generation of a new protrusion at the corresponding side of the follower cell's front. This protrusion remains when the cell migrates forward. In this way, the protrusion of the follower cell accurately follows the protrusion of its leading cell. According to this hypothesis, cells cannot precisely follow their leading cells without constantly recruiting actin to their front, which explains the suppression of actin polymerization waves on streaming cells.

To verify this hypothesis, direct measurements of forces and corresponding motions at the front of cells are required. Cell local motion can be assessed by measuring the change of cell shapes as previously described (Driscoll et al. 2011). The measurement of forces requires new experimental techniques. Traction force microscopy (TFM) has been applied to study force generation during cell migration with much success. Previous studies suggest that adherent migrating cells exert forces in the tens of nanonewtons per square micrometer range (Ricart et al. 2011; Bastounis et al. 2016), which is about the force resolution of TFM (Plotnikov et al. 2014;

Bergert et al. 2015). I could use TFM to measure forces generated by migrating cell streams and study how the forces are related to the overall cell shape change. However, TFM does not have enough force resolution for measuring localized actin forces, such as forces generated at cell-cell contacts, which are expected to be in the low piconewtons to hundreds of piconewtons per square micrometer range (Bergert et al. 2015; Ehrlicher 2007). Atomic force microscopy (AFM), which has the force resolution of ~10 piconewtons (Neuman & Nagy 2008), could be used to measure local actin forces at the front of cells. I could study the spatial-temporal evolution of the force generated at cell front and compare it to the actin polymerization and protrusion generation in the same region. I expect to see a strong correlation between force and actin polymerization, as well as between force and protrusions. I could also compare the force generated in a cell to the protrusion generated on its leading cell to determine whether the protrusion at the back of the leading cell induces actin polymerization, and in turn, force generation at the front of the follower cell. These studies would provide significant insights into the mechanism that regulate coupling of protrusion waves in collective cell migration.

What is the molecular mechanism of cell-cell coupling?

I proposed the above hypothesis from a mechanical perspective without considering molecules mediating cell-cell adhesions. Recent studies indicate that cadherins and their adapter proteins mediate cell-cell coupling through regulation of the cytoskeleton in mammalian cells (Case & Waterman 2011; Schwarz & Gardel

2012). Although the coupling of protrusion waves discussed in this thesis is not cadherin-dependent, as *Dictyostelium* does not express cadherins, there are some other types of cell-cell adhesion molecules identified in *Dictyostelium*, such as csA, DdCAD-1, TgrB1 and TgrC1 (Coates & Harwood 2001; Siu et al. 2011). Both csA and Tgr proteins are linked to the actin cytoskeleton (Sriskanthadevan et al. 2011; Siu et al. 2011; Bastounis et al. 2016) and are thereby expected to mediate the coordination of motion between cells. However, they exhibit distinct migratory phenotypes: cells lacking csA form head-to-tail streams, whereas cells lacking Tgr proteins cannot form stable streams (Harloff et al. 1989; Chen et al. 2013). These results suggest that cell-cell adhesion molecules play different roles in the coordination of cell motion through the cytoskeleton. I hypothesize that cells lacking Tgr proteins do not exclusively polymerize actin at cell-cell contacts, and these cells do not exhibit front narrowing and thereby coupling of protrusion waves between cells. On the other hand, I speculate that cells lacking csA are still able to exclusively recruit actin to their front at cell-cell contact regions and they exhibit coupled protrusion waves. I could verify this by applying the experimental and analytical tools developed in Chapter 6 to cells lacking cell-cell adhesion molecules and then comparing their shape dynamics and cytoskeletal behavior to wild type streaming cells. I expect to see that the unstable steaming behavior shown in cells lacking Tgr is related to the loss of restricted actin polymerization at the front of cells. Such studies would help to determine the way these adhesion molecules regulate the actin cytoskeleton and their distinct roles in collective migration.

Appendices

This chapter provides supplemental methods for the work described in Chapter 3, 5, 6. A.3 is adapted from Wang, Parent, and Losert (in preparation). Meghan Driscoll originally developed the shape analysis program and integrated it with a boundary finding program (snake algorithm).

A.1 Shape Dynamics Analysis

To better extract cell boundaries, I pre-processed images with ImageJ (NIH) to enhance the contrast of original fluorescent images and reduce background noise. After this step, the cell areas appear to be very bright in images. Then, I used a custom cell shape dynamics Matlab program that was previously developed in the Losert lab to extract cell boundaries and obtain the measurements (Driscoll, McCann, et al. 2012). The program implemented a snake algorithm to extract cell boundaries.

The process can be broken into 3 steps: Step I, extracting cell boundaries from a sequence of images of fluorescently-labeled migrating cells via a snake algorithm. For each frame, the extracted cell boundary was interpolated to output 400 points that are equally distributed. This step is implemented by 4 functions in the shape

dynamics analysis code: **readDirectory, findBoundaries, trackBlobs, findSnakes**.

Below are the values of parameters I chose in my analysis:

findBoundaries(N, minRegionSize, noiseLevelAdd, adjustGammaPre, adjustGammaPost, erodeImage, dilateImage, dilateLargeCH, inDirectory, savePath);
minRegionSize = 50; %original 100 % the minimum size of a blob (in square pixels)
noiseLevelAdd = 0.001; % the maximum value of the uniform noise that is added to the image
adjustGammaPre = 0.6; % the adjusted gamma of the image prior to brightness-contrast adjustment
adjustGammaPost = 0.4; % the adjusted gamma of the image after brightness-contrast adjustment (deals with varying blob brightness)
erodeImage = 2; % number of pixels the binary image is eroded prior to labeling
dilateImage = 2; % number of pixels the binary image is next dilated prior to labeling (smooths the outline)
dilateLargeCH = 3; % number of pixels the binary image is dilated prior to finding the large convex hull

trackBlobs(N, centerTravelThresh, areaChangeThresh, minRegionSize, maxRegionSize, minSolidity, minDuration, savePath);
centerTravelThresh = 50; % the maximum number of pixels that a centroid is allowed to travel between two frames
areaChangeThresh = 50; % the maximum percentage area change that a blob is allowed between two frames
maxRegionSize = 10000; % the maximum mean size of a blob (in square pixels) (2*sqrt(maxRegionSize/pi)/pixelsmm is the maximum diameter in microns)
minSolidity = 0.5; % the minimum mean solidity of a blob
minDuration = 35; % the minimum duration of a blob (in frames)

findSnakes(N, paramsSnake, inDirectory, savePath);
paramsSnake.mu = 0.1;
paramsSnake.alpha = 0.002; % alpha and beta are the snake tension and rigidity
paramsSnake.beta = 0.005; %
paramsSnake.gamma = 1; % you probably don't want to change gamma and kappa

```
paramsSnake.kappa = 0.6;
paramsSnake.dmin = 0.5;                % the minimum number of pixels seperating boundary
points after interpolation
paramsSnake.dmax = 1.5;                % the maximum number of pixels seperating boundary
points after interpolation
paramsSnake.NoGVFIterations = 80;      % the number of iterations used to calculate the
gradient vector field of the image
paramsSnake.EquidistantNum = 400;      % the number of boundary points per blob
outputted by the 'posNum' variable (usually 400) (must be a multiple of 4 for measureMotion)
paramsSnake.widthImageB = 6;           % the width, in pixels, of the border added to each
frame (must be larger than widthCellB)
paramsSnake.widthCellB = 5;            % the effective width, in pixels, of the border added to
each blob's image

paramsSnake.binLowerThresh = 0.7;      % the lower threshold when nearly binarizing the
image (multiplied by the automatically calculated binarization threshold)
paramsSnake.binUpperThresh = 1.1;      % the upper threshold when nearly binarizing the
image (multiplied by the automatically calculated binarization threshold)
paramsSnake.blobGamma = 0.4;           % the adjusted gamma of the nearly binarized image
paramsSnake.numIterFirst = 40;         % the number of initial snake iterations
paramsSnake.numIterEvery = 25;         % the number of subsequent snake iterations
performed in every loop before checking convergence
paramsSnake.convergeThresh = 3;        % the maximum area change, in pixels, per loop that
is considered converged
paramsSnake.runLimit = 250;            % the maximum number of iteration loops run
```

Step II, mapping boundary points from frame to frame. The 1:1 mapping of 400 pairs of points between every two successive frames is determined by a function **initShape** of the shape dynamics program (initMode = 'leastSquares'). The program goes through all 1:1 mapping possibilities, calculates the sum of the squared distance

between pairs of points, and chooses the mapping with the minimum squared distance.

Step III, obtaining measurements on cell boundaries. Different types of measurements can be obtained from the shape dynamics program. I mainly used the measurements of curvature, intensity, and boundary motion. These measurements are calculated in the following ways: Curvature: the program fits each boundary point and two nearby boundary points to a circle and calculates the reciprocal of the radius of that circle as the curvature of that boundary point; Intensity: the program draws a circle around each boundary point and calculates average intensity in that circle. Note that the cell boundaries are extracted based on contrast-enhanced images, while the fluorescent intensity is measured based on original images. Boundary motion: the direction of boundary motion for each boundary point is perpendicular to the tangent line passing through that point. For each boundary point, the program finds the

corresponding point on the next shape and calculates the distance between these two points.

This step is implemented by 3 functions in the shape dynamics analysis code: **measureShape, measureMotion, measureIntensity**. Below are the values of parameters I chose in my analysis:

```
% measure shape parameters
boundaryPoint = 25;         % number of boundary points curvature is found over
curvatureThresh = 0.35;     % the maximum allowed value of the curvature measure

% measure motion parameters
frameDelta = 9;             % the number of frames over which motion is measured
motionThresh = 22;          % the maximum allowed value of the local motion measure
smoothMotion = 29;          % the number of boundary points over which motion is first
smoothed %12
smoothMotionAgain = 21;     % the number of boundary points over which motion is next
smoothed
smoothCentroid = 5;         % the number of frames the centroid position is smoothed over
prior to calculating the velocity
frameVelocity = 3;      %original 2    % the number of frames the centroid velocity is
calculated over when finding velocity

% measure intensity parameters
intensityKernelRadius = 5; %10 (lifact - pcaIntensity is 6; phcrac=5)
innerIntensityM = paramsSnake.EquidistantNum/8;
```

All the calculated measurements are saved in **shape.m** file that is generated by the shape analysis program. Below is the list of outputs that I used in my study:

```
shape
.area              - the area of the shape in every frame (uses snakeDist and polyarea)
.perimeter         - the perimeter of the shape in every frame (uses snakeDist)
```

.centroid - the centroid of the shape in every frame (uses snakeDist)
.curvature - the boundary curvature at each boundary point (uses snakeNum) Curvatures above or below a cutoff are given the magnitude of the cutoff
.uncutCurvature - the uncut boundary curvature at each boundary point (uses snakeNum)
.aliCurvature - the curvature for realignment (added by Chenlu)
.uncutaliCurvature - the uncut curvature for realignment (added by Chenlu)
.orientation - the orientation of the best fit ellipse (uses regionprops)
.frontBack - the boundary points closest to the front and the back of the shape, as measured by orientation (the back and front are not distinguished here)
.motion - the uncut local motion measure
.alimotion - the realigned motion measurment (added by Chenlu)
.cutMotion - the cut local motion measure
.front - the boundary point closest to the front of the shape (the front was determined by the orientation and average motion)
.back - the boundary point closest to the back of the shape
.motionFront - the local motion measure aligned so that the front is at (M-1)/2
.motionBack - the local motion measure aligned so that the back is at (M-1)/2
.intensity - the intensity at each boundary point

I used two ways to present these results as shown in Figure A.1, taking **curvature** measurement as an example. Curvature measurement on the boundary of a single cell can be plotted in a kymograph with function **imagesc (shape.curvature')** in Matlab (Figure A.1A), where the horizontal axis indicates time, the vertical axis indicates the position on cell boundary, and the color indicates the magnitude of curvature. Measurements also can be plotted in 3D with the function **surf**

(shape.curvature') in Matlab (Figure A.1B). Both the third dimension and the color indicate magnitude of curvature, which makes the presentation more intuitive.

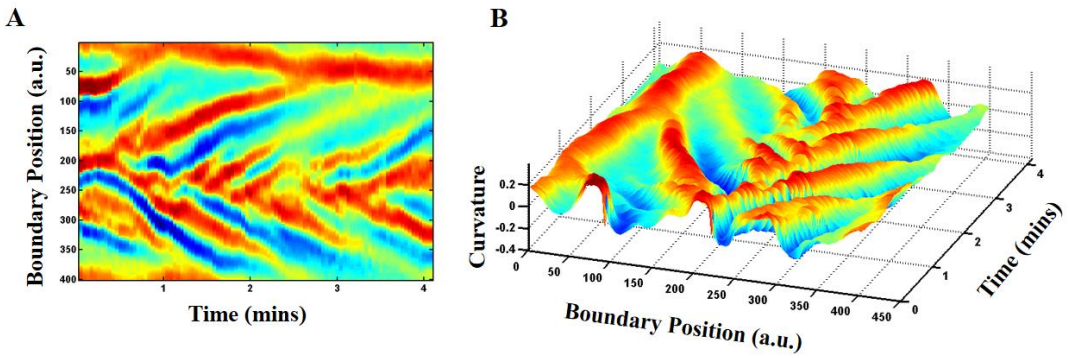

Figure A.1- Presentations of Curvature Dynamics in 2D and 3D.

A.2 Shape Dynamics Analysis on Pairs of Cells

To analyze the shape dynamics of pairs of cells, I mixed wild type cells with AX3-Lifact-RFP cells and imaged the streaming process as discussed in Chapter 6. During the imaging acquisition, I intended to find the situation that two RFP-labeled cells migrate together and un-fluorescent labeled cells migrate before and after them in the stream. I applied shape dynamics analysis program to extract the overall boundaries of pairs of cells, found 400 evenly-spaced points on the overall boundaries, and obtained the measurements in a way similar to individual cells.

A.3 Correlation Analysis and Calculation of Wave Frequency and Speed

Correlation between boundary points

To quantitatively compare the dynamics of different cells or different points on the same cell, I calculated the cross-correlation of measurements between cells or

points. Figure A2 shows how to find out the correlation of curvature between two points on a cell boundary. Black curve in A.2A indicates how the curvature of a boundary point change with time; red curve indicates how the curvature of another boundary point change with time. These two points are 20 boundary points apart. The cross-correlation of two measurements can be calculated with the following equation:

$$Corr(\tau) = \int_{-\infty}^{+\infty} f^*(t)g(t+\tau)\mathrm{d}t$$

Note, f, g are time evolution of curvature measurements of the two points. The equation calculates the correlation between f and g that is shifted with a lag "τ". A Matlab built-in function **xcorr** was used to calculate it.

As shown in Figure A.2B, the maximum correlation is found when the lag is equal to -5. It indicates the red curve shown in Figure A.2A overlaps the most with the black curve when shifting the red curve to the left by 12.5 seconds (5frame*2.5second/frame). In other words, the curvature of these two points exhibits a 12.5 seconds time delay, which can be used to calculate the speed of curvature waves traveling between these two points. In addition, the peaks in Figure A.2B appear in a periodic pattern, suggesting curvature waves occur periodically.

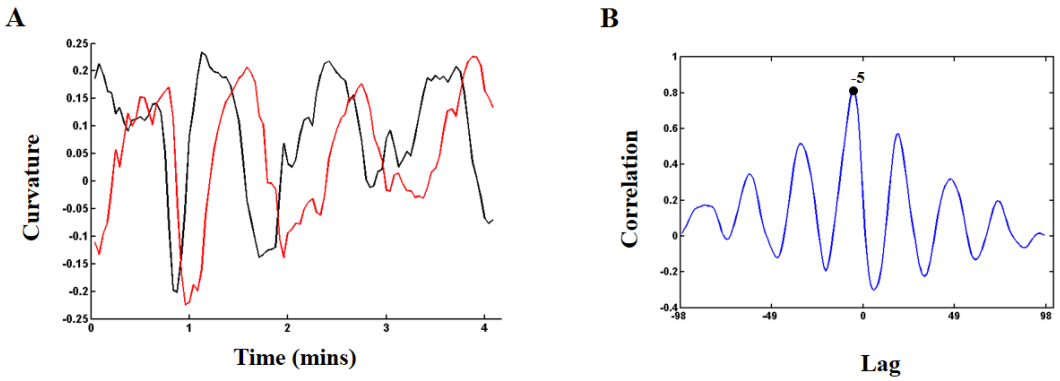

Figure A.2- Calculation of Cross-correlation of Curvature Dynamics between Two Boundary Points.

With this method, I compared the curvature dynamics of boundary points on one cell with those on the following cell, and found the curvature dynamics on two successive cells are highly correlated as discussed in Chapter 6. Below is an example of comparing the curvature dynamics between cells. First, choose a reference point on the leading cell. The reference point should be in the back region of the leading cell, and I usually use point 70. Next, compare all other points on the same side of cell boundary to the reference point. The example code is below:

```
cref = shape.curvature(ref,:);
for i = 1:200
   ci = shape.curvature(i,:);
   correlation(i,:) = xcorr(cref,ci);
end
imagesc(correlation);
```

Calculation of wave frequency

The correlation was used to calculate the speed and period of curvature waves. The period of waves was calculated by auto-correlation, meaning the measurement was compared to itself, *i.e.,* the f and g in the correlation equation were the same. The calculation can be broken into four steps:

(i) Define the time evolution of the curvature of point x to be f(t) (Figure A.3A).
(ii) For each point on the side of cells (point 50~150, 250~350), calculate the auto-correlation of f(t). The maximum correlation is always found when lag is equal to 0 frame because f(t) always overlaps with itself without any shifting. Other peaks are found when the lag is divisible by the wave period. (Figure A.3B)
(iii) Represent the correlation of each point on one side of the cell in a kymograph. The magnitude of the correlation is indicated by color. Overall, all points on the same side of cell boundary exhibit similar period as the bright stripes are nearly vertical (Figure A.3C).
(iv) Calculate the mean correlation over all points at different lags. The first maximum is always 0, and the position of next peak indicates the period. In this example, the lag is 17, so the period is 17*2.5sec = 42.5 seconds, suggesting, for every 42.5 seconds, there is a new curvature wave generated on this side of the cell boundary. Thus, the period of wave generation is about 20 seconds when considering both sides of the cell boundary.

Below is an example code:

```
for i = 1:200
   ci = shape.curvature(i,:);
   correlation(i,:) = xcorr(ci,ci);
```

```
end
imagesc(correlation);
collapse = mean(correlation);
```

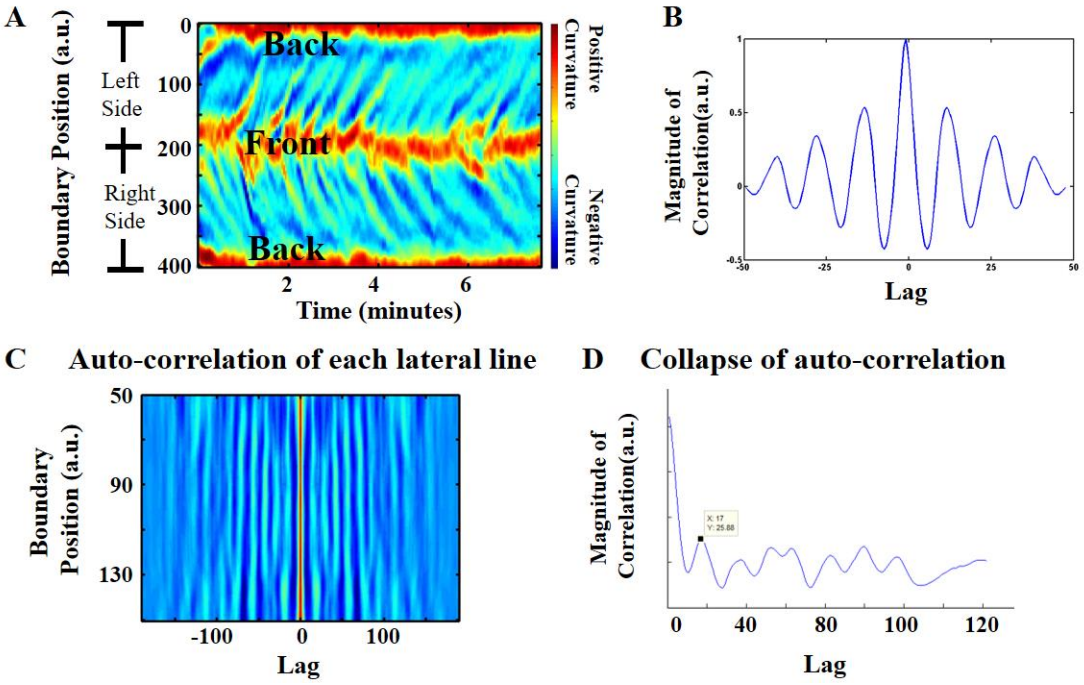

Figure A.3- Calculation of Period of Curvature Waves using Auto-correlation.

Calculation of wave speed

The speed of waves is obtained by calculating the cross-correlation between two points on the cell boundary. A typical example is shown in Figure A.4. Point 100 and point 110 are two points on the cell boundary. I calculated the cross-correlation of the curvature dynamics between these two points. The position (lag) of the maximum correlation indicates the time delay when curvature waves traveling through these two points. Similar cross-correlation calculation was implemented for each pairs of points on the side of cell boundary (two points are 10 points apart), and results are plotted in 2D (Figure A.4B). Each horizontal line indicates how the

correlation of between a certain pair of points change with lag, and the vertical axis indicates the position of the anterior point in this pair. Next, the position of maximum correlation averaged over all points is obtained. Thus, the speed of waves passing through this region can be calculated by the following equation:

$$\text{Speed} = \frac{(\#\text{ of point2} - \#\text{ of point1})*\text{Perimeter}/400}{\text{Lag}_{max}* \text{ Time Interval between Frames}}$$

Below is an example code:

```
delta_p  % # of point2 - # of point 1, I used 10
for i = 1:180
   ci = shape.curvature(i,:);
   cj = shape.curvature(i+delta_p,:);
   correlation(i,:) = xcorr(ci,cj);
end
imagesc(correlation);
collapse = mean(correlation);
```

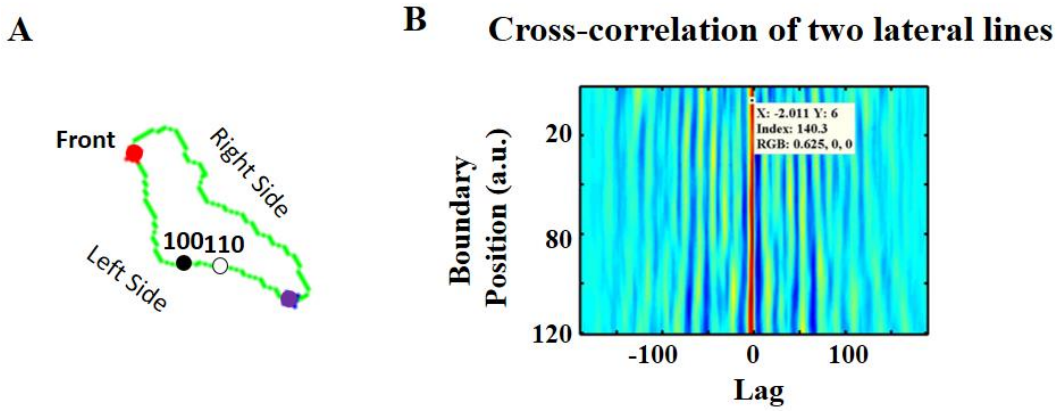

Figure A.4- Calculation of Speed of Curvature Waves using Cross-correlation.

A.3 Principal Component Analysis

Cell shape change modes and F-actin intensity modes are calculated by principal component analysis (PCA) based on the imaging data collected from AX3-Lifeact-RFP cells. We collected sequences of images containing individual and streaming AX3-Lifeact-RFP cells under different experimental conditions, from which thousands of cell shapes are extracted and measurements of shape change and intensity are calculated. The shape change of cells can be measured by overlaying cell shapes extracted from two successive images and calculating the moving distance of each boundary point. For the 1:1 mapping between the two shapes, they are aligned by front point (point 0), which is decided by cell orientation.

Since the data size varies, same amount of cell shape change data and intensity data are randomly selected (1000 shapes from each experimental condition) to build a data set that contributed equally from each experimental condition, and PCA was performed on these two data sets respectively using Matlab function **princomp** to find out principle components and their variance. Intensity modes for ACA were calculated similarly based on imaging data collected from ACA-YFP AX3 cells. 1900 shapes from each condition are randomly selected for analysis respectively.

The principle component analysis can be broken into four steps:
(i), obtain measurements (boundary motion, intensity) from shape dynamics analysis program. 400 measurements along cell boundary are obtained for every two successive shapes for each cell.

(ii), realign these measurements making the point 0 is always the front of cells. All cell shapes were fitted into ellipses, and the long axis of ellipses intersects with each cell shape at two points. The point where cell exhibit more protrusive motion is the cell front.

(iii), run **princomp**. Each row represents measurement on a cell at a certain time (frame); each column represents each boundary points on cells. Mathematically, principal component analysis is a linear transformation of original data into new orthogonal coordinates. Each dimension is a principal component, which is named mode. The function **princomp** provides the variance of each data point under each mode, *i.e.*, the value of the analyzing measurement on a cell at a certain time under each mode. Variances are normalized under each mode, making the sum of the square of variances to be 1.

(iv), measurements on all cells are represented by the same set of modes. Statistical analysis of the values under each mode provides insights in the difference between experimental groups.

Steps i-iii are implemented by the function **measurePCA** in the shape dynamics analysis code. The inputs and outputs of the function is showing below. Note that only the output data ".toPCA" was actually used in further analysis.

Inputs:

N	- the number of images
M	- the number of boundary points in each snake
frameDelta	- the number of frames over which motion is measured
savePath	- the directory that data is saved in

Output:

pca

.pcaShape

.toPCA	- the realigned shape measurement for each boundary point
.pc	- the varience of each principal component for each cell shape
.zscores	- the total varience of each principal component
.latent	- eigenvalues of the covariance matrix of "toPCA"

.pcaCurvature

.toPCA	- the realigned curvature measurement for each boundary point
.pc	- the varience of each principal component for each cell shape
.zscores	- the total varience of each principal component
.latent	- eigenvalues of the covariance matrix of "toPCA"

.pcaMotion

.toPCA	- the realigned motion measurement for each boundary point
.pc	- the varience of each principal component for each cell shape
.zscores	- the total varience of each principal component
.latent	- eigenvalues of the covariance matrix of "toPCA"

.pcaIntensity

.toPCA	- the realigned intensity measurement for each boundary point
.pc	- the varience of each principal component for each cell shape
.zscores	- the total varience of each principal component
.latent	- eigenvalues of the covariance matrix of "toPCA"

Step iv is calculated separately based on the output of **measurePCA**, which is saved in the matlab data file: **pca.m**. Take the analysis of motion modes for example: First, select equal number of motion measurements from each experimental condition, and create a combined data set. In my analysis, motion measurement calculated by overlaying cell shapes with their successive shapes, and 1000 such measurements

were randomly selected from each experimental condition from the previously saved Matlab data file: pcaMotion.toPCA. Thus, all selected data was combined and is created to a combined data set. The PCA was performed on this combined data set:

[pc,zscores,latent] = princomp(pcaMotion.toPCA);

Inputs:

number - number of cell shapes of each experimental condition

shapenum - number of shapes selected into the combine data set

Outputs:

pcaMotion

.pc	- the varience of each principal component for each cell shape
.toPCA	- the realigned motion measurement for each boundary point
.zscores	- the total varience of each principal component
.latent	- eigenvalues of the covariance matrix of "toPCA"
.source	- cell label in the un-selected shape data
.numofcells	- cell sample size of each condition
.numofexpts	- times that experiments repeated for each condition

Values of each cell under each condition were saved in pcaMotion.pc. Then, they were performed with statistical analysis on it. An example is showing below:

Values of pc were divided into 6 groups, representing 6 experimental condition.

Values of each condition under mode N can be extracted as following:

Single_control = pcaMotion.pc(1:1000,N);

Single_low = pcaMotion.pc(1001:2000,N);

Single_high = pcaMotion.pc(2001:3000,N);

Stream_control = pcaMotion.pc(3001:4000,N);

Stream_low = pcaMotion.pc(4001:5000,N);

Stream_high = pcaMotion.pc(5001:6000,N);

To compare untreated stream cells to single cells, I calculated mean and standard deviation of Single_control and Stream_control by using functions **mean** and **std** in Matlab, and plotted it accordingly.

Bibliography

Aabo, T. et al., 2010. Effect of long- and short-term exposure to laser light at 1070 nm on growth of Saccharomyces cerevisiae. J. Biomed. Opt., (15).

Afonso, P. V. et al., 2012. LTB4 Is a Signal-Relay Molecule during Neutrophil Chemotaxis. Developmental Cell, 22(5), pp.1079–1091.

Alexander, S. et al., 2008. Dynamic imaging of cancer growth and invasion: a modified skin-fold chamber model. Histochemistry and Cell Biology, 130(6), pp.1147–1154.

Allard, J. & Mogilner, A., 2013. Traveling waves in actin dynamics and cell motility. Current Opinion in Cell Biology, 25(1), pp.107–115.

Alt, W. et al., 1995. Patterns of spontaneous motility in videomicrographs of human epidermal keratinocytes (HEK). Biochemistry and Cell Biology, 73(7-8), pp.441–459.

Anna Bagorda, Carole A. Parent, V.A.M., 2006. Chemotaxis: moving forward and holding on to the past. Thromb.Haemost., 95.

Arneborg, N. et al., 2005. Interactive optical trapping shows that confinement is a determinant of growth in a mixed yeast culture. FEMS Microbiology Letters, 245(1), pp.155–159.

Ashkin, A. et al., 1986. Observation of a single-beam gradient force optical trap for dielectric particles. Opt. Lett., 11, pp.288–290.

Ashkin, A. & Dziedzic, J.M., 1987. Optical trapping and manipulation of viruses and bacteria. Science, 235(4795), pp.1517–1520.

Ashkin, A., Dziedzic, J.M. & Yamane, T., 1987. Optical trapping and manipulation of single cells using infrared laser beams. Nature, 330(6150), pp.769–771.

Ashkin, A., 1992. Forces of a single-beam gradient laser trap on a dielectric sphere in the ray optics regime. Biophysical Journal, 61(2), pp.569–582.

Ayano, S. et al., 2006. Quantitative measurement of damage caused by 1064-nm wavelength optical trapping of Escherichia coli cells using on-chip single cell cultivation system. Biochemical and Biophysical Research Communications, 350(3), pp.678–684.

Bae, A.J. & Bodenschatz, E., 2010. On the swimming of Dictyostelium amoebae. Proceedings of the National Academy of Sciences, 107(44), pp.E165–E166.

Banerjee, A.G. et al., 2011. Survey on indirect optical manipulation of cells, nucleic acids, and motor proteins. J. Biomed. Opt., 16(5), p.51302.

Banerjee, A.G. et al., 2012. Realtime path planning for coordinated transport of multiple particles using optical tweezers. IEEE Transactions on Automation Science and Engineering, 9(4), pp.669–678.

Barr, V.A. & Bunnell, S.C., 2009. Interference reflection microscopy. Curr Protoc Cell Biol, Chapter 4, p.Unit 4 23.

Barry, N.P. & Bretscher, M.S., 2010. Dictyostelium amoebae and neutrophils can swim. Proceedings of the National Academy of Sciences, 107(25), pp.11376–11380.

Bastounis, E. et al., 2016. Cooperative Cell Motility during Tandem Locomotion of Amoeboid Cells. Molecular Biology of the Cell.

Bergert, M. et al., 2015. Force transmission during adhesion-independent migration. Nature cell biology, 17(4), pp.524–9.

Berns, M.W., 1976. A possible two-photon effect in vitro using a focused laser beam. Biophysical journal, 16(8), pp.973–977.

Burute, M. & Thery, M., 2012. Spatial segregation between cell–cell and cell–matrix adhesions. Current Opinion in Cell Biology, 24(5), pp.628–636.

Cai, D. et al., 2014. Mechanical feedback through E-cadherin promotes direction sensing during collective cell migration. Cell, 157(5), pp.1146–1159.

Case, L.B. & Waterman, C.M., 2011. Adhesive F-actin Waves: A Novel Integrin-Mediated Adhesion Complex Coupled to Ventral Actin Polymerization. PLoS ONE, 6(11), p.e26631.

Chen, G. et al., 2013. TgrC1 mediates cell–cell adhesion by interacting with TgrB1 via mutual IPT/TIG domains during development of Dictyostelium discoideum. Biochemical Journal, 452(2), pp.259–269.

Chenyang, X. & Prince, J.L., 1998. Snakes, shapes, and gradient vector flow. Image Processing, IEEE Transactions on, 7(3), pp.359–369.

Chowdhury, S. et al., 2012. Automated indirect transport of biological cells using planar gripper formations. 8th IEEE International Conference on Automation Science and Engineering, pp.267–272.

Chowdhury, S. et al., 2013. Automated Cell Transport in Optical Tweezers-Assisted Microfluidic Chambers. IEEE Transactions on Automation Science and Engineering, 10(4), pp.980–989.

Chowdhury, S. et al., 2013. Automated manipulation of biological cells using gripper formations controlled by optical tweezers. IEEE Transactions on Automation Science and Engineering, PP(99), pp.1–10.

Chowdhury, S. et al., 2013. Automated indirect manipulation of irregular shaped cells with Optical Tweezers for studying collective cell migration. 2013 IEEE International Conference on Robotics and Automation (ICRA), pp.2789–2794.

Coates, J.C. & Harwood, A.J., 2001. Cell-cell adhesion and signal transduction during Dictyostelium development. Journal of Cell Science, 114(24), pp.4349–4358.

Collins, C. & Nelson, W.J., 2015. Running with neighbors: coordinating cell migration and cell-cell adhesion. Current opinion in cell biology, 36, pp.62–70.

Cornillon, S. et al., 2000. Phg1p Is a Nine-transmembrane Protein Superfamily Member Involved in Dictyostelium Adhesion and Phagocytosis. Journal of Biological Chemistry, 275(44), pp.34287–34292.

Cornillon, S. et al., 2006. An adhesion molecule in free-living Dictyostelium amoebae with integrin beta features. EMBO reports, 7(6), pp.617–621.

Cornillon, S., Froquet, R. & Cosson, P., 2008. Involvement of Sib Proteins in the Regulation of Cellular Adhesion in Dictyostelium discoideum. Eukaryotic Cell, 7(9), pp.1600–1605.

Critchley, D.R., 2000. Focal adhesions – the cytoskeletal connection. Current Opinion in Cell Biology, 12(1), pp.133–139.

Cuvelier, D. et al., 2007. The universal dynamics of cell spreading. Curr Biol, 17(8), pp.694–699.

Dao, M., Lim, C.T. & Suresh, S., 2003. Mechanics of the human red blood cell deformed by optical tweezers. Journal of the Mechanics and Physics of Solids, 51(11–12), pp.2259–2280.

Décavé, E. et al., 2002. Shear Flow-Induced Detachment Kinetics of Dictyostelium discoideum Cells from Solid Substrate. Biophysical Journal, 82(5), pp.2383–2395.

Devreotes, P. et al., 1987. Chapter 17 Transmembrane Signaling in Dictyostelium. In A. S. James, ed. Methods in Cell Biology. Academic Press, pp. 299–331.

Devreotes, P. & Horwitz, A.R., 2015. Signaling networks that regulate cell migration. Cold Spring Harb Perspect Biol, 7(8), p.a005959.

Dholakia, K., Spalding, G. & MacDonald, M., Optical tweezers: The next generation. Physics world15-10 (Oct 2002).

Dogterom, M. & Surrey, T., 2012. Microtubule organization in vitro. Current Opinion in Cell Biology, 25(1), pp.1–7.

Dormann, D. et al., 2002. Visualizing PI3 Kinase-Mediated Cell-Cell Signaling during Dictyostelium Development. Current Biology, 12(14), pp.1178–1188.

Dormann, D. & Weijer, C.J., 2006. Imaging of cell migration. EMBO J, 25(15), pp.3480–3493.

Dovas, A. et al., 2012. Imaging interactions between macrophages and tumour cells that are involved in metastasis in vivo and in vitro. Journal of Microscopy, p.no–no.

Doyle, A.D. et al., 2013. Dimensions in cell migration. Current Opinion in Cell Biology, 25(5), pp.642–649.

Driscoll, M.K., Fourkas, J.T. & Losert, W., 2011. Local and global measures of shape dynamics. Phys. Biol., 8(5).

Driscoll, M.K., Albanese, J.L., et al., 2012. Automated image analysis of nuclear shape: What can we learn from a prematurely aged cell? Aging (Albany NY), 4(2), pp.119–132.

Driscoll, M.K. et al., 2012. Cell Shape Dynamics: From Waves to Migration. PLoS Comput Biol, 8(3), p.e1002392.

Driscoll, M.K. et al., 2014. Cellular Contact Guidance through Dynamic Sensing of Nanotopography. ACS nano, 8(4), pp.3546–55.

Driscoll, M.K. et al., 2015. Spatiotemporal relationships between the cell shape and the actomyosin cortex of periodically protruding cells. Cytoskeleton, 72(6), pp.268–281.

Dubin-Thaler, B.J. et al., 2004. Nanometer Analysis of Cell Spreading on Matrix-Coated Surfaces Reveals Two Distinct Cell States and STEPs. Biophysical Journal, 86(3), pp.1794–1806.

DuFort, C.C., Paszek, M.J. & Weaver, V.M., 2011. Balancing forces: architectural control of mechanotransduction. Nature reviews. Molecular cell biology, 12(5), pp.308–19.

Ehrlicher, R.A. and A., 2007. The Forces Behind Cell Movement. Int J Biol Sci., 3(5), pp.303–317.

Eichinger, L. et al., 2005. The genome of the social amoeba Dictyostelium discoideum. Nature, 435(7038), pp.43–57.

Enculescu, M. et al., 2010. Modeling of Protrusion Phenotypes Driven by the Actin-Membrane Interaction. Biophysical Journal, 98(8), pp.1571–1581.

Ericsson, M. et al., 2000. Sorting Out Bacterial Viability with Optical Tweezers. J. Bacteriol., 182(19), pp.5551–5555.

Etienne-Manneville, S. & Hall, A., 2002. Rho GTPases in cell biology. Nature, 420(6916), pp.629–635.

Farooqui, R. & Fenteany, G., 2005. Multiple rows of cells behind an epithelial wound edge extend cryptic lamellipodia to collectively drive cell-sheet movement. Journal of cell science, 118(Pt 1), pp.51–63.

Fey, P. et al., 2002. SadA, a novel adhesion receptor in Dictyostelium. The Journal of Cell Biology, 159(6), pp.1109–1119.

Fletcher, D.A.M.R.D., 2010. Cell mechanics and the cytoskeleton. Nature, 463(7280), pp.485–492.

Friedl, P., Borgmann, S. & Bröcker, E.-B., 2001. Amoeboid leukocyte crawling through extracellular matrix: lessons from the Dictyostelium paradigm of cell movement. Journal of Leukocyte Biology, 70(4), pp.491–509.

Friedl, P. & Wolf, K., 2003. Tumour-cell invasion and migration: diversity and escape mechanisms. Nature reviews. Cancer, 3(5), pp.362–74.

Friedl, P. & Gilmour, D., 2009. Collective cell migration in morphogenesis, regeneration and cancer. Nat Rev Mol Cell Biol, 10(7), pp.445–457.

Friedl, P. & Wolf, K., 2010. Plasticity of cell migration: a multiscale tuning model. The Journal of Cell Biology, 188(1), pp.11–19.

Fujita, S., Ohshima, M. & Iwata, H., 2009. Time-lapse observation of cell alignment on nanogrooves. Journal of the Royal Society, Interface / the Royal Society, 6 Suppl 3, pp.S269–77.

Garcia, G.L. & Parent, C.A., 2008. Signal relay during chemotaxis. Journal of Microscopy, 231(3), pp.529–534.

Gerisch, G. et al., 1995. Chemoattractant-controlled accumulation of coronin at the leading edge of Dictyostelium cells monitored using a green fluorescent protein–coronin fusion protein. Current Biology, 5(11), pp.1280–1285.

Gerisch, G. et al., 2004. Mobile Actin Clusters and Traveling Waves in Cells Recovering from Actin Depolymerization. Biophysical Journal, 87(5), pp.3493–3503.

Gerisch, G. et al., 2009. Self-organizing actin waves as planar phagocytic cup structures. Cell Adhesion and Migration, 3(4).

Gerisch, G. et al., 2012. PIP3 waves and PTEN dynamics in the emergence of cell polarity. Biophysical Journal, 103(6), pp.1170–1178.

Grier, D.G., 2003. A revolution in optical manipulation. Nat Photon, 424(6950), pp.810–816.

Grigaravičius, P., Greulich, K.O. & Monajembashi, S., 2009. Laser Microbeams and Optical Tweezers in Ageing Research. ChemPhysChem, 10(1), pp.79–85.

Guilluy, C. et al., 2014. Isolated nuclei adapt to force and reveal a mechanotransduction pathway in the nucleus. Nature cell biology, 16(4), pp.376–81.

Haeger, A. et al., 2015. Collective cell migration: guidance principles and hierarchies. Trends in Cell Biology, 25(9), pp.556–566.

Hanahan, D. & Weinberg, R.A., 2011. Hallmarks of cancer: the next generation. Cell, 144(5), pp.646–674.

Harloff, C., Gerisch, G. & Noegel, A.A., 1989. Selective elimination of the contact site A protein of Dictyostelium discoideum by gene disruption. Genes & Development , 3 (12a), pp.2011–2019.

Heasman, S.J. & Ridley, A.J., 2008. Mammalian Rho GTPases: new insights into their functions from in vivo studies. Nat Rev Mol Cell Biol, 9(9), pp.690–701.

Hsu, S. et al., 2005. Effects of shear stress on endothelial cell haptotaxis on micropatterned surfaces. Biochemical and Biophysical Research Communications, 337(1), pp.401–409.

Iijima, M. & Devreotes, P., 2002. Tumor Suppressor PTEN Mediates Sensing of Chemoattractant Gradients. Cell, 109(5), pp.599–610.

Janson, L.W. & Taylor, D.L., 1993. In vitro models of tail contraction and cytoplasmic streaming in amoeboid cells. The Journal of Cell Biology, 123(2), pp.345–356.

Jay, P.Y. et al., 1995. A mechanical function of myosin II in cell motility. J Cell Sci, 108 Pt 1, pp.387–393.

Keren, K. et al., 2008. Mechanism of shape determination in motile cells. Nature, 453(7194), pp.475–480.

Killich, T. et al., 1993. The locomotion, shape and pseudopodial dynamics of unstimulated Dictyostelium cells are not random. Journal of Cell Science, 106(4), pp.1005–1013.

Kim, J.-H., Dooling, L.J. & Asthagiri, A.R., 2010. Intercellular mechanotransduction during multicellular morphodynamics. Journal of the Royal Society, Interface / the Royal Society, 7 Suppl 3, pp.S341–50.

Kimmel, A.R. & Parent, C. a, 2003. The signal to move: D. discoideum go orienteering. Science (New York, N.Y.), 300(5625), pp.1525–7.

King, J.S. & Insall, R.H., 2008. Chemotaxis: TorC before You Akt; Current Biology, 18(18), pp.R864–R866.

König, K. et al., 1996. Cell damage in near-infrared multimode optical traps as a result of multiphoton absorption. Opt. Lett., 21(14), pp.1090–1092.

Koss, B. et al., 2011. Indirect optical gripping with triplet traps. J. Opt. Soc. Am. B, 28(5).

Kreitmeier, M. et al., 1995. A talin homologue of Dictyostelium rapidly assembles at the leading edge of cells in response to chemoattractant. The Journal of Cell Biology, 129(1), pp.179–188.

Kriebel, P.W., Barr, V.A. & Parent, C.A., 2003. Adenylyl Cyclase Localization Regulates Streaming during Chemotaxis. Cell, 112(4), pp.549–560.

Kriebel, P.W. et al., 2008. Collective cell migration requires vesicular trafficking for chemoattractant delivery at the trailing edge. The Journal of Cell Biology, 183(5), pp.949–961.

Kriebel, P.W. & Parent, C.A., 2009. Chemotaxis T. Jin & D. Hereld, eds. , 571, pp.111–124.

Kulin, S. et al., 2002. Real-Time Measurement of Spontaneous Antigen-Antibody Dissociation. Biophysical Journal, 83(4), pp.1965–1973.

Lämmermann, T. & Sixt, M., 2009. Mechanical modes of “amoeboid” cell migration. Current Opinion in Cell Biology, 21(5), pp.636–644.

Lämmermann, T. et al., 2013. Neutrophil swarms require LTB4 and integrins at sites of cell death in vivo. Nature, 498(7454), pp.371–375.

Lauffenburger, D.A. & Horwitz, A.F., 1996. Cell migration: A physically integrated molecular process. Cell, 84(3), pp.359–369.

Lecuit, T., Lenne, P.-F. & Munro, E., 2011. Force Generation, Transmission, and Integration during Cell and Tissue Morphogenesis. Annual Review of Cell and Developmental Biology, 27(1), pp.157–184.

Liang, H. et al., 1996. Wavelength dependence of cell cloning efficiency after optical trapping. Biophysical Journal, 70(3), pp.1529–1533.

Lim, C.T. et al., 2006. Experimental techniques for single cell and single molecule biomechanics. Materials Science and Engineering: C, 26(8), pp.1278–1288.

Lin, F. et al., 2008. Lymphocyte Electrotaxis In Vitro and In Vivo. The Journal of Immunology, 181(4), pp.2465–2471.

Loomis, W.F. et al., 2012. Innate non-specific cell substratum adhesion. PloS one, 7(8), p.e42033.

Machacek, M.D.G., 2006. Morphodynamic profiling of protrusion phenotypes. Biophys. J., 90(4), p.1439.

Maruthamuthu, V. et al., 2011. Cell-ECM traction force modulates endogenous tension at cell – cell contacts. Proceedings of the National Academy of Sciences, 108(12), pp.4708–4713.

Matsuda, M. & Chitnis, A.B., 2010. Atoh1a expression must be restricted by Notch signaling for effective morphogenesis of the posterior lateral line primordium in zebrafish. Development, 137(20), pp.3477–3487.

Mayor, R. & Etienne-Manneville, S., 2016. The front and rear of collective cell migration. Nat Rev Mol Cell Biol, 17(2), pp.97–109.

McCann, C.P. et al., 2010. Cell speed, persistence and information transmission during signal relay and collective migration. Journal of Cell Science, 10(123), pp.1724–1731.

McCann, C.P., 2011. Individual and collective dynamics of chemotaxing cells. PhD Thesis. (College Park, Maryland: University of Maryland).

McCann CP, Rericha EC, Wang C, Losert W, Parent CA. 2014 Dictyostelium Cells Migrate Similarly on Surfaces of Varying Chemical Composition M. Parsons, ed. PLoS ONE, 9(2), p.e87981.

Meili, R. et al., 2010. Myosin II is essential for the spatiotemporal organization of traction forces during cell motility. Mol Biol Cell, 21(3), pp.405–417.

Menko, a. S., Bleaken, B.M. & Walker, J.L., 2014. Regional-specific alterations in cell-cell junctions, cytoskeletal networks and myosin-mediated mechanical cues coordinate collectivity of movement of epithelial cells in response to injury. Experimental Cell Research, 322(1), pp.133–148.

Mills, J.C. et al., 1998. Apoptotic Membrane Blebbing Is Regulated by Myosin Light Chain Phosphorylation. The Journal of Cell Biology, 140(3), pp.627–636.

Mirsaidov, U. et al., 2008. Optimal optical trap for bacterial viability. Physical Review E, 78(2), p.21910.

Müller-Taubenberger, A., Kortholt, A. & Eichinger, L., 2013. Simple system – substantial share: The use of Dictyostelium in cell biology and molecular medicine. European Journal of Cell Biology, 92(2), pp.45–53.

Murrell, M. et al., 2011. Spreading dynamics of biomimetic actin cortices. Biophys J, 100(6), pp.1400–1409.

Nascimento, J.M. et al., 2006. Analysis of sperm motility using optical tweezers. J. Biomed. Opt., (11).

Nelson, R.D., Quie, P.G. & Simmons, R.L., 1975. Chemotaxis under agarose: a new and simple method for measuring chemotaxis and spontaneous migration of human polymorphonuclear leukocytes and monocytes. Journal of immunology (Baltimore, Md. : 1950), 115, pp.1650–1656.

Neuman, K.C. et al., 1999. Characterization of Photodamage to Escherichia coli in Optical Traps. Biophysical Journal, 77(5), pp.2856–2863.

Neuman, K.C. & Nagy, A., 2008. Single-molecule force spectroscopy : optical tweezers , magnetic tweezers and atomic force microscopy. Nat Meth, 5(6), pp.491–505.

Niewöhner, J. et al., 1997. Talin-Null Cells of Dictyostelium Are Strongly Defective in Adhesion to Particle and Substrate Surfaces and Slightly Impaired in Cytokinesis. The Journal of Cell Biology, 138(2), pp.349–361.

Pang, K.M., Lee, E. & Knecht, D.A., 1998. Use of a fusion protein between GFP and an actin-binding domain to visualize transient filamentous-actin structures. Curr Biol, 8(7), pp.405–408.

Parent, C.A. et al., 1998. G protein signaling events are activated at the leading edge of chemotactic cells. Cell, 95(1), pp.81–91.

Parent, C.A. & Devreotes, P.N., 1999. A Cell's Sense of Direction. Science, 284(5415), pp.765–770.

Parent, C.A., 2004. Making all the right moves: chemotaxis in neutrophils and Dictyostelium. Current Opinion in Cell Biology, 16(1), pp.4–13.

Parsons, J.T., Horwitz, A.R. & Schwartz, M. a, 2010. Cell adhesion: integrating cytoskeletal dynamics and cellular tension. Nature reviews. Molecular cell biology, 11(9), pp.633–43.

Patsialou, A. et al., 2009. Invasion of Human Breast Cancer Cells In vivo Requires Both Paracrine and Autocrine Loops Involving the Colony-Stimulating Factor-1 Receptor. Cancer Research, 69(24), pp.9498–9506.

Penela, P., Nogués, L. & Mayor, F., 2014. Role of G protein-coupled receptor kinases in cell migration. Current Opinion in Cell Biology, 27, pp.10–17.

Plotnikov, S. V et al., 2014. High-Resolution Traction Force Microscopy. Methods in cell biology, 123, pp.367–394.

Prass, M. et al., 2006. Direct measurement of the lamellipodial protrusive force in a migrating cell. The Journal of Cell Biology, 174 (6), pp.767–772.

Rasmussen, M.B., Oddershede, L.B. & Siegumfeldt, H., 2008. Optical Tweezers Cause Physiological Damage to Escherichia coli and Listeria Bacteria. Applied and Environmental Microbiology, 74(8), pp.2441–2446.

Reichl, E.M. et al., 2008. Interactions between myosin and actin crosslinkers control cytokinesis contractility dynamics and mechanics. Curr Biol, 18(7), pp.471–480.

Ricart, B.G. et al., 2011. Measuring Traction Forces of Motile Dendritic Cells on Micropost Arrays. Biophysical Journal, 101(11), pp.2620–2628.

Rickert, P. et al., 2000. Leukocytes navigate by compass: roles of PI3Kγ and its lipid products. Trends in Cell Biology, 10(11), pp.466–473.

Riedl, J. et al., 2008. Lifeact: a versatile marker to visualize F-actin. Nat Meth, 5(7), pp.605–607.

Ridley, A.J. et al., 2003. Cell Migration: Integrating Signals from Front to Back. Science, 302(5651), pp.1704–1709.

Ridley, A.J., 2011. Life at the leading edge. Cell, 145(7), pp.1012–1022.

Robinson, D.N. & Spudich, J.A., 2004. Mechanics and regulation of cytokinesis. Curr Opin Cell Biol, 16(2), pp.182–188.

Roca-Cusachs, P., Sunyer, R. & Trepat, X., 2013. Mechanical guidance of cell migration: lessons from chemotaxis. Current Opinion in Cell Biology, (25), pp.1–7.

Rottner, K. & Stradal, T.E.B., 2011. Actin dynamics and turnover in cell motility. Current Opinion in Cell Biology, 23(5), pp.569–578.

Schindl, M. et al., 1995. Cell-substrate interactions and locomotion of Dictyostelium wild-type and mutants defective in three cytoskeletal proteins: a study using quantitative reflection interference contrast microscopy. Biophys J, 68(3), pp.1177–1190.

Schwarz, U.S. & Gardel, M.L., 2012. United we stand - integrating the actin cytoskeleton and cell-matrix adhesions in cellular mechanotransduction. Journal of Cell Science, 125(13), pp.3051–3060.

Siu, C.-H. et al., 2011. Regulation of spatiotemporal expression of cell–cell adhesion molecules during development of Dictyostelium discoideum. Development, Growth & Differentiation, 53(4), pp.518–527.

Sniadecki, N.J., 2010. A tiny touch: activation of cell signaling pathways with magnetic nanoparticles. Endocrinology, 151(2), pp.451–7.

Socol, M. et al., 2010. Synchronization of Dictyostelium discoideum adhesion and spreading using electrostatic forces. Bioelectrochemistry, 79(2), pp.198–210.

Spalding, G.C., Courtial, J. & Di Leonardo, R., 2008. Chapter 6 Holographic optical tweezers. In Structured Light and Its Applications: An Introduction to Phase-Structured Beams and Nanoscale Optical Forces. Academic Press, pp. 139–168.

Sriskanthadevan, S. et al., 2011. The cell adhesion molecule DdCAD-1 regulates morphogenesis through differential spatiotemporal expression in Dictyostelium discoideum. Development, 138(12), pp.2487–2497.

Stephens, G. j et al., 2008. Dimensionality and dynamics in the behavior of C. elegans. PLoS Comput. Biol., 4(4), p.e1000028.

Sun, X. et al., 2015. Asymmetric nanotopography biases cytoskeletal dynamics and promotes unidirectional cell guidance. Proceedings of the National Academy of Sciences, 112(41), p.201502970.

Sussman, M., 1987. Chapter 2 Cultivation and Synchronous Morphogenesis of Dictyostelium under Controlled Experimental Conditions. In A. S. James, ed. Methods in Cell Biology. Academic Press, pp. 9–29.

Svoboda, K. & Block, S.M., 1994. Biological Applications of Optical Forces. Annu Rev Bioph Biom, 23(1), pp.247–285.

Szatmary, A.C., Stuelten, C.H. & Nossal, R., 2014. Improving the design of the agarose spot assay for eukaryotic cell chemotaxis. RSC Adv., 4(100), pp.57343–57349.

Tan, Y. et al., 2010. Mechanical Characterization of Human Red Blood Cells Under Different Osmotic Conditions by Robotic Manipulation With Optical Tweezers. IEEE Transactions on Biomedical Engineering,, 57(7), pp.1816–1825.

Thakur, A. et al., 2012. Automated Indirect Optical Micromanipulation Of Biological Cells Using Indirect Pushing To Minimize Photo-Damage. ASME 2012 International Design Engineering Technical Conferences (IDETC) & Computers and Information in Engineering Conference (CIE).

Thakur A, Chowdhury S, Wang C, Losert W, Gupta SK. 2014 Indirect pushing based automated micromanipulation of biological cells using optical tweezers. The International Journal of Robotics Research, 33, 1098–1111.

Thiery, J.P., 2002. Epithelial-mesenchymal transitions in tumour progression. Nat Rev Cancer, 2(6), pp.442–454.

Van Haastert, P.J.M. & Bosgraaf, L., 2009. The local cell curvature guides pseudopodia towards chemoattractants. HFSP Journal, 3(4), pp.282–286.

Vasioukhin, V. & Fuchs, E., 2001. Actin dynamics and cell–cell adhesion in epithelia. Current Opinion in Cell Biology, 13(1), pp.76–84.

Veltman, D.M., Keizer-Gunnik, I. & Van Haastert, P.J.M., 2008. Four key signaling pathways mediating chemotaxis in Dictyostelium discoideum. The Journal of Cell Biology , 180 (4), pp.747–753.

Ventre, M., Causa, F. & Netti, P. a, 2012. Determinants of cell-material crosstalk at the interface: towards engineering of cell instructive materials. Journal of the Royal Society, Interface / the Royal Society, 9(74), pp.2017–32.

Vitorino, P. et al., 2011. A steering model of endothelial sheet migration recapitulates monolayer integrity and directed collective migration. Molecular and cellular biology, 31(2), pp.342–50.

Wang C, Chowdhury S, Gupta SK, Losert W. 2013 Optical micromanipulation of active cells with minimal perturbations: direct and indirect pushing. J. Biomed. Opt. 18, 045001.

Wang C, Chowdhury S, Parent C, Gupta SK, Losert W. 2014 The interplay of cell – cell and cell – substrate adhesion in collective cell migration. Journal of The Royal Society Interface 11 (100), 20140684.

Wang, J. et al., 2000. The Membrane Glycoprotein gp150 Is Encoded by the lagC Gene and Mediates Cell–Cell Adhesion by Heterophilic Binding during Dictyostelium Development. Developmental Biology, 227(2), pp.734–745.

Wang, X. et al., 2011. Enhanced cell sorting and manipulation with combined optical tweezer and microfluidic chip technologies. Lab on a Chip, 11(21), pp.3656–3662.

Wang, Y. et al., 2005. Visualizing the mechanical activation of Src. Nature, 434(7036), pp.1040–1045.

Weber, G.F., Bjerke, M.A. & DeSimone, D.W., 2012. A Mechanoresponsive Cadherin-Keratin Complex Directs Polarized Protrusive Behavior and Collective Cell Migration. Developmental cell, 22(1), pp.104–115.

Weijer, C.J., 2009. Collective cell migration in development. Journal of Cell Science, 122(18), pp.3215–3223.

Weiner, O.D. et al., 2007. An Actin-Based Wave Generator Organizes Cell Motility. PLoS Biol, 5(9), p.e221.

Wischerhoff, E. et al., 2008. Controlled Cell Adhesion on PEG-Based Switchable Surfaces. Angewandte Chemie International Edition, 47(30), pp.5666–5668.

Wolf, K. et al., 2013. Physical limits of cell migration: Control by ECM space and nuclear deformation and tuning by proteolysis and traction force. The Journal of Cell Biology, 201(7), pp.1069–1084.

Wolfenson, H., Lavelin, I. & Geiger, B., 2013. Dynamic Regulation of the Structure and Functions of Integrin Adhesions. Developmental Cell, 24(5), pp.447–458.

Wu, S.K. et al., 2014. Cortical F-actin stabilization generates apical-lateral patterns of junctional contractility that integrate cells into epithelia. Nature cell biology, 16(2), pp.1–15.

Yoshida, K. & Soldati, T., 2006. Dissection of amoeboid movement into two mechanically distinct modes. Journal of Cell Science, 119(18), pp.3833–3844.

Zaritsky, A. et al., 2014. Propagating Waves of Directionality and Coordination Orchestrate Collective Cell Migration. PLoS computational biology, 10(7), p.e1003747.

Zhang, H. & Liu, K.-K., 2008. Optical tweezers for single cells. Journal of The Royal Society Interface, 5(24), pp.671–690.

Zhao, M. et al., 2002. Genetic analysis of the role of G protein-coupled receptor signaling in electrotaxis. The Journal of cell biology, 157(6), pp.921–927.

Zouani, O.F., Gocheva, V. & Durrieu, M.C., 2014. Membrane nanowaves in single and collective cell migration. PLoS ONE, 9(5).